



Delft University of Technology

---

# Investigation of Bio-Sourced Resveratrol Epoxy Resin as a Matrix Material for Structural Aerospace Composites

---

*A dissertation submitted to the Delft University of Technology for the degree of MSc Aerospace Engineering in the Faculty of Aerospace Engineering.*

*By Elmar-Daniel Alasoo*

*Thesis committee:*

*Chair: Dr. Otto Bergsma*

*Supervisors: Dr. Baris Kumru & William E. Dyer*

*External Examiner: Dr. Daniël Peeters*

*Project Duration: 01.03.2024 – 20.01.2025*

*Student Number: 5835895*

*An electronic version is available at: <https://repository.tudelft.nl/>*



## Preface

The following chapter marks the conclusion of my Master's thesis and, indeed, the academic journey that began over five years ago when I enrolled at the University of Manchester to study Mechanical Engineering. From my earliest introduction to materials science and manufacturing technologies, particularly their application in aerospace engineering, I became convinced that there was no better institution to further develop my knowledge than TU Delft. Therefore, I have been incredibly fortunate to consider the Department of Aerospace Structures and Materials my second home over the past two years.

These years have been both challenging and transformative, offering invaluable opportunities for personal and academic growth. The journey, however, was not without its moments of doubt, setbacks, and mental struggles. Yet, in hindsight, these hardships have served as the foundation for my development, both personally and professionally, making every difficulty worthwhile.

While this thesis bears my name, it represents the collective efforts, guidance, and support of many individuals. I am profoundly grateful to my supervisor, Dr Baris Kumru, for his mentorship and for introducing me to the fascinating field of bio-based epoxies. His guidance has been indispensable. I also extend my heartfelt thanks to William Dyer for his insights into both the theoretical and experimental dimensions of my work, and for his patience in addressing my many questions. I am equally grateful to Niklas Lorenz, whose lucid explanations of cure kinetics and assistance in experimental work were pivotal to my progress.

I would like to express my special appreciation to the laboratory technicians - Victor, Dave, Chantal, Alexander, Caitlin, and Roy - for their invaluable support in conducting experiments and sharing their practical expertise. A practical project of this scale would have been impossible without their assistance.

Above all, the unwavering support of my dear family has made this journey immeasurably easier and more joyful. I am eternally thankful for their belief in me, especially during the most challenging moments. I am truly blessed to have them by my side, and from the depths of my heart, I thank them for their love and encouragement - even when I struggled to believe in myself.

To everyone who has been a part of this journey: thank you for your integral role in its success!

# Table of Contents

Preface.....	iii
Table of Contents .....	iv
List of Figures.....	vii
List of Tables.....	ix
Nomenclature.....	x
Abstract.....	xi
1. Introduction.....	1
1.1. Research Background & Motivation .....	1
1.1.1. Sustainable Aviation.....	1
1.1.2. Polymer Matrix Composites in Aerospace .....	2
1.1.3. Negative Impact of Epoxy Resin Production.....	2
1.1.4. Alternatives to BPA .....	3
1.2. Thesis Outline .....	3
2. Composite Materials .....	4
2.1. Introduction to Composites.....	4
2.2. Fibre–Matrix Interface in PMCs.....	5
2.3. Dispersed Phase Overview .....	7
2.4. Matrix Phase Overview.....	8
2.4.1. Thermoplastic Polymers .....	9
2.4.2. Thermosetting Polymers .....	10
2.5. Environmental Burden of PMCs.....	11
2.5.1. Carbon Fibres.....	11
2.5.2. Epoxy Resins .....	12
2.6. The Importance of Sustainable Thermoset Research.....	13
2.6.1. Matrix versus Fibres .....	13
2.6.2. Thermosets versus Thermoplastics .....	14
3. Epoxy Resins .....	14
3.1. Epoxy Monomers.....	14
3.1.1. DGEBA Monomer .....	15
3.1.2. Tactix 742 Monomer.....	15

---

3.2.	Curing Agents .....	16
3.2.1.	Anhydrides .....	16
3.2.2.	Amines .....	16
3.3.	Advantages of Epoxy Resins .....	18
3.4.	Limitations of Epoxy Resins.....	18
3.5.	Bio-Based Epoxies.....	19
3.5.1.	State of Research of Bio-Based Epoxy Monomers.....	21
3.5.2.	Limitations of Existing Bio-Based Resins .....	23
3.5.3.	Resveratrol .....	24
4.	Methodology .....	26
5.	Resin Characterisation .....	27
5.1.	Thermal Property Analysis .....	27
5.1.1.	Thermogravimetric Analysis.....	27
5.1.2.	Differential Scanning Calorimetry.....	30
5.1.3.	Dynamic Mechanical Analysis .....	41
5.1.4.	Dynamic Rheometry .....	46
5.1.5.	Processing & Curing Cycle Finalisation.....	50
5.2.	Physical Property Analysis .....	51
5.2.1.	Bio-based Content.....	51
5.2.2.	Density .....	52
5.2.3.	Water Contact Angle .....	53
5.2.4.	Water absorption .....	55
5.2.5.	Gel Content .....	56
5.3.	Mechanical Property Analysis .....	57
5.3.1.	Tensile Specimen Preparation.....	58
5.3.2.	Tensile Testing & Results .....	61
5.3.3.	3-Point Bend Specimen Preparation .....	63
5.3.4.	3-Point Bend Testing & Results.....	65
5.3.5.	Fracture Toughness Specimen Preparation.....	67
5.3.6.	Fracture Toughness Testing & Results.....	70
6.	Composite Manufacturing & Testing.....	73
6.1.	Specimen Design & Manufacturing.....	73

---

---

6.1.1.	Wet Lay-Up & Autoclave Curing .....	73
6.1.2.	Quality Control .....	76
6.2.	ILSS Testing.....	78
6.3.	IPSS Testing.....	80
6.4.	CLC Testing .....	82
7.	Outcomes .....	84
7.1.	Resin Thermal & Physical Properties .....	84
7.2.	Resin Mechanical Properties.....	87
7.3.	Composite Mechanical Properties .....	92
7.4.	Final Conclusions.....	94
8.	Recommendations for Future Work .....	96
	References.....	97
	Appendix A .....	106
A.1.	Stoichiometry Ratio Determination .....	106
	Theory and Practice .....	106
	Ratio Estimation Procedure .....	106

## List of Figures

Figure 1. Composite classification based on the reinforcement type (Callister, William D. & Rethwisch, 2018a).....	5
Figure 2. Fibre-matrix interaction under applied load (Callister, William D. & Rethwisch, 2018a).....	6
Figure 3. Influence of the fibre length on the effectiveness of load transfer (Callister, William D. & Rethwisch, 2018a) .....	7
Figure 4. Representation of a) thermoplastic molecule and b) thermosetting polymer molecules (Wikipedia, 2024e).....	11
Figure 5. Epoxide functional group (Wikipedia, 2024d) .....	15
Figure 6. The reaction of a hydroxyl group and epichlorohydrin, followed by dehydrohalogenation (Wikipedia, 2024d).....	15
Figure 7. Formation of DGEBA from BPA and epichlorohydrin (Capretti et al., 2023).....	15
Figure 8. Structure of Tactix 742 epoxy resin (Hughes & Than Tun, 2019) .....	15
Figure 9. Reaction of glycidyl group with amine curing agent (Fink, 2013) .....	17
Figure 10. Examples of aromatic amines used in curing of epoxy resins.....	18
Figure 11. Overview of bio-based molecules used as starting material for epoxy formulation (Wikipedia, 2024f).....	20
Figure 12. Chemical structure of (a) trans-resveratrol and (b) resveratrol triglycidyl ether (RTE) (Tian et al., 2020).....	25
Figure 13. TGA results of RTE and T742 resins in air .....	29
Figure 14. Rate of mass loss with respect to temperature.....	29
Figure 15. Heat flow vs temperature non-isothermal DSC plot .....	31
Figure 16. Estimation of T <sub>g</sub> of the uncured resin at different heating rates .....	32
Figure 17. Kissinger model linear fitting plots for RTE and T742 resins.....	33
Figure 18. Non-isothermal DSC exotherms for a) RTE and b) T742 resins.....	34
Figure 19. Non-isothermal DSC runs at 10°C/min and 25°C/min .....	36
Figure 20. Example of TTT diagram .....	37
Figure 21. Isothermal DSC heat flow vs time.....	38
Figure 22. Isothermal DSC conversion vs time .....	38
Figure 23. Rate of cure vs conversion and the overlaid Kamal-Sourour model.....	39
Figure 24. Non-isothermal DSC run on a sample cured at 180°C for 2 hours .....	40
Figure 25. Damping vs temperature for various heating rates (no post-curing).....	42
Figure 26. Storage and loss moduli for various heating rates (no post-curing).....	43
Figure 27. Damping vs temperature at various heating rates for RTE-DDS (with post-curing) ..	44
Figure 28. Storage and loss moduli at various heating rates for RTE-DDS (with post-curing) ...	44
Figure 29. Damping vs temperature at various heating rates for T742-DDS (with post-curing) .	45
Figure 30. Storage and loss moduli at various heating rates for T742-DDS (with post-curing) ..	45
Figure 31. Change in viscosity of RTE-DDS and T742-DDS with temperature.....	47
Figure 32. Change in storage and loss moduli with time at 100°C .....	48
Figure 33. Change in storage and loss moduli with time at 180°C .....	49
Figure 34. Calibration of the Attension Theta Optical Tensiometer .....	54

Figure 35. Images of water droplets placed on RTE 1, 2 and 3 .....	54
Figure 36. Illustration of a dogbone geometry used for tensile testing .....	58
Figure 37. Tensile mould not filled in due to trapped air.....	60
Figure 38. Cracking of tensile samples due to thermal contraction.....	60
Figure 39. RTE-DDS tensile samples .....	62
Figure 40. Tensile test load-displacement curve for RTE-DDS and T742-DDS .....	63
Figure 41. Rectangular RTE-DDS panel .....	64
Figure 42. RTE sample loaded in 3-point bending .....	65
Figure 43. RTE specimens for 3PB.....	65
Figure 44. Flexural test load-displacement curve for RTE and T742 samples .....	67
Figure 45. Test setup and sample dimensions considered in the SENB fracture toughness test ..	68
Figure 46. Crack dimensions of RTE 5 specimen.....	69
Figure 47. RTE-DDS SENB specimens.....	70
Figure 48. SENB sample installed in the fixture .....	70
Figure 49. Load-deflection curve with AB and AB' lines for RTE 3.....	72
Figure 50. Prepared mould.....	74
Figure 51. Schematic of a mould layup .....	74
Figure 52. Autoclave curing cycle diagram .....	75
Figure 53. Vacuum bag after curing.....	75
Figure 54. De-moulded composite panel.....	75
Figure 55. Quality control samples.....	77
Figure 56. Short beam test configuration.....	78
Figure 57. Invalid failure mode example.....	78
Figure 58. Mid-plane inter-laminar shear failure.....	79
Figure 59. ILSS load-displacement curve.....	79
Figure 60. IPSS specimen orientation.....	80
Figure 61. IPSS test setup .....	80
Figure 62. IPSS test stress-strain curve.....	81
Figure 63. Prepared specimens for CLC testing.....	82
Figure 64. CLC test setup .....	82
Figure 65. Compression test load-displacement curves.....	83
Figure 66. Tg values of several resveratrol-based and commercial epoxy resins (HexFlow, 2024; Shang et al., 2018b; Tian et al., 2020; Westlake, 2024a) .....	86
Figure 67. Tensile and flexural strengths of various epoxy resins (Gupta, 2024; Huntsman, 2010, 2012; Kaushik, 2024).....	89
Figure 68. Tensile and flexural moduli of various epoxy resins(Gupta, 2024; Huntsman, 2010, 2012; Kaushik, 2024).....	89
Figure 69. Fracture toughness values of various epoxy resins (Gupta, 2024; HexFlow, 2024; Kaushik, 2024; Westlake, 2024a) .....	90
Figure 70. ILSS, IPSS and compressive strength values for different matrices .....	93
Figure 71. Shear and Compressive moduli for different matrices .....	93

## List of Tables

Table 1. Properties of common PMC fibre materials and aerospace-grade aluminium alloys (Callister, William D. & Rethwisch, 2018a).....	8
Table 2. Properties of common polymers used in PMCs (Mallick, 2017a).....	9
Table 3. Weight loss data of RTE and T742 resins .....	29
Table 4. Peak temperature values for RTE and T742 resins .....	33
Table 5. Kamal-Sourour model parameters .....	40
Table 6. Viscosity values at specific temperatures of RTE- and T742-based resins.....	47
Table 7. Summary of processing and manufacturing steps for RTE-DDS resin.....	50
Table 8. Density measurement data for RTE and T742 resins.....	53
Table 9. Water contact angle measurements for RTE (left) and T742 (right) resins.....	54
Table 10. Water absorption data for RTE and T742 resins .....	55
Table 11. Gel content data for RTE-DDS and T742-DDS.....	56
Table 12. Average dimensions of RTE tensile specimens.....	61
Table 13. Average dimensions of T742 tensile specimens.....	61
Table 14. UTS, strain at break and elastic modulus values for RTE and T742 samples .....	62
Table 15. Average dimensions of RTE 3-point bend specimens.....	64
Table 16. Average dimensions of T742 3-point bend specimens.....	64
Table 17. Flexural stress at break, strain at break and flexural elastic modulus values for RTE..	66
Table 18. Average dimensions of RTE fracture toughness specimens and the corresponding notch data.....	69
Table 19. T742 SENB specimen and notch dimensions .....	69
Table 20. Crack length requirements for RTE and T742 specimens .....	70
Table 21. Fracture toughness of RTE and T742 and parameters used for test validity .....	72
Table 22. Quality control data from Test Method II .....	76
Table 23. Quality control data from Test Method I.....	77
Table 24. ILSS specimen data and test results .....	79
Table 25. IPSS specimen data and test results .....	81
Table 26. CLC specimen data and test results .....	83
Table 27. Resin thermal characterisation summary .....	84
Table 28. Resin physical characterisation summary .....	86
Table 29. Resin mechanical characterisation summary .....	87
Table 30. Composite mechanical characterisation summary .....	92

## Nomenclature

### List of Abbreviations

IEA	International Energy Agency	PAN	Polyacrylonitrile
ICAO	International Civil Aviation Organisation	CFRP	Carbon fibre-reinforced polymer
IATA	International Air Transport Association	DMF	Dimethylformamide
PMC	Polymer matrix composite	NIH	National Institute of Health
BADGE/D	Bisphenol A diglycidyl ether	CDC	Centers for Disease Control and Prevention
GEBA		WHO	World Health Organisation
BPA	Bisphenol A	ECHA	European Chemicals Agency
DDS	4,4'-diaminodiphenylsulfone	EFSA	The European Food Safety Authority
DDM	4,4'-diaminodiphenylmethane	UTS	Ultimate tensile strength
DDE	4,4'-diaminodiphenyl ether	THPM	tris(4-hydroxyphenyl)methane
ASTM	American Society for Testing and Materials	GF	Glass fibre
DSC	Differential scanning calorimetry	RTE	Resveratrol triglycidyl ether
DMA	Dynamic mechanical analysis	T742	Tactix 742
EEW	Epoxy equivalent weight	TTT	Time-temperature-transformation
THPMTGE	Tri-glycidyl ether of tris(4-hydroxyphenyl)methane	MSE	Mean squared error
IPSS	In-plane shear strength	RMSE	Root mean squared error
ILSS	Inter-laminar shear strength	PP	Polypropylene
TGA	Thermogravimetric analysis	CLC	Combined loading compression
THPM	Tris(4-hydroxyphenyl)methane		

### List of Symbols

$\tan(\delta)$	Damping ratio	$E'$	Storage Modulus
$F^{cu}$	laminar compressive strength	$E''$	Loss Modulus
$T_g$	Glass Transition Temperature	$\eta$	Viscosity
$\beta$	Heating rate	$\tau_{12}^m$	In-plane shear strength
$G^{chord}$	shear modulus of elasticity	$K_{Ic}$	Critical Stress Intensity Factor
$E_c$	Compressive modulus	$F^{ILS}$	Inter-laminar shear strength

## Abstract

### **Investigation of Bio-Sourced Resveratrol Epoxy Resin as a Matrix Material for Structural Aerospace Composites.**

**Research Goal:** *Investigating the potential of sustainable epoxy based on resveratrol triglycidyl ether (RTE) as a high-performance alternative to petroleum-based matrix materials in aerospace composite applications.*

The aviation sector increasingly prioritises sustainability, necessitating the development of environmentally friendly materials. Polymer matrix composites (PMCs), widely utilised in aerospace for their excellent strength, stiffness and low weight, predominantly rely on petroleum-derived epoxy resins. These resins pose significant environmental concerns, including dependency on non-renewable resources, health risks, and limited recyclability. This thesis explores the feasibility of bio-based resveratrol epoxy resin as a sustainable replacement for commercial epoxy monomers. A comparison with commercial Tactix 742 monomer is motivated by its application in areas requiring high thermomechanical performance, a niche that RTE has the potential to fill. Furthermore, RTE is also compared with BADGE as the most common commercial monomer, as well as other bio-based monomers. Derived from renewable sources such as knotweed, resveratrol offers a trifunctional aromatic structure with the potential to achieve high thermal and mechanical properties while reducing the environmental burden of epoxy.

The study entailed the synthesis and detailed characterisation of resveratrol epoxy resin, assessing thermal, physical, and mechanical properties. Results demonstrated a bio-based content of 74% compared to 25% of the T742-based analogue, indicating the resin's strong potential as a renewable material. Thermal analysis revealed a high glass transition temperature ( $T_g$ ) of over 300°C and thermal resistance of up to 350°C, outperforming aerospace-grade commercial epoxies. Mechanical testing highlighted the resin's excellent performance, including fracture toughness 47% higher than analogue T742 resin. Furthermore, additional mechanical testing of composite panels showed RTE's usability in composite structures.

The findings confirm that resveratrol-based epoxy resin offers a sustainable, high-performance alternative to traditional petroleum-based matrices. It also tackles some common bio-based epoxy issues, such as hydrophilicity and low thermal stability. Recommendations for further optimisation, including viscosity reduction, further cure kinetic characterisation and thermal performance investigation, are provided to facilitate the broader adoption of bio-based thermosetting systems in aerospace and other high-performance sectors.

**Key words:** *bio-based epoxy, composite manufacturing, resveratrol, glass transition temperature, sustainability, resveratrol triglycidyl ether (RTE), aerospace-grade composite matrix, polymer matrix composite*

# 1. Introduction

## 1.1. Research Background & Motivation

### 1.1.1. Sustainable Aviation

Over the previous decades, the aviation industry has firmly established itself at the forefront of efficient technology. Initially, the drive to develop more efficient aircraft technology was governed purely by economic reasoning. However, as humanity fully recognised the problem of global warming and climate change, aircraft producers embraced the concept of eco-efficiency, which prioritises sustainable development considering both the economic benefits and environmental impacts of commercial activity (Muthu, 2020). Despite the reduced growth of the aviation sector during and in the aftermath of the COVID-19 pandemic, recent estimates suggest an increased yearly demand of 4.3% over the next 20 years. As a result, it is expected that by the middle of the 2030s, more than 200,000 flights will take place daily, constituting a two-fold increase with respect to 2023 (ICAO, 2024). According to the International Energy Agency (IEA), in the year 2022, the aviation industry accounted for 2% of global energy CO<sub>2</sub> emissions – 80% of the pre-pandemic level (IEA, 2022).

To mitigate emissions growth, the International Air Transport Association (IATA) passed a resolution requiring its member airlines to achieve net-zero carbon emissions by 2050. The Fly Net Zero Commitment aims to align the aviation industry with the Paris Climate Agreement, striving to limit the increase in average global temperatures to below 2°C above pre-industrial levels (IATA, 2021c). The detailed plan to achieve the 2050 net-zero goals can be found in the form of IATA Roadmaps which are aimed at all participants in the aviation industry including airlines, government agencies, aircraft manufacturers, suppliers, etc. The Roadmaps address the necessary transition steps according to 5 categories: energy infrastructure, finance, operations, policy, and aircraft technology (IATA, 2021d). As defined by IATA, there are three main constraints to net zero transition in the aviation industry, namely, ‘*Aircraft have a long useful life*’, ‘*Aircraft have lengthy development times*’ and ‘*Aircraft use a large amount of energy*’ (IATA, 2021b). The latter variable is specifically targeted by the aircraft technology roadmap.

With the average commercial aircraft lifetime being 25 years and the age of European and North American fleets averaging 11 and 14 years in 2025 (Statista, 2020), it is estimated that more than 12000 aircraft will be decommissioned in the coming 20 years. On top of that, a large number of aircraft components are expected to be replaced as part of the routine maintenance (Scheelhaase et al., 2022). Thus, a sense of urgency is related to the timely introduction of sustainable technology.

Emphasis on the introduction of new propulsion, airframe and structure systems is governed by the potentially high-efficiency yield. Historically, the introduction of new-generation aircraft has resulted in a commendable 20% reduction in energy consumption compared to the aircraft they replaced. Consequently, a 15-20% improvement in energy efficiency compared to the current best technology is expected for the evolutionary aircraft. This would be accomplished through the

implementation of more efficient engines, employment of lighter materials, and enhancement of aerodynamic performance. By the year 2050, advancements in aircraft technology are anticipated to yield a nearly 7% reduction in in-flight energy consumption (IATA, 2021a).

One of the action points included in the Aircraft Technology Roadmap emphasises the utilisation of ‘Composite material wings and fuselage sections in service’, thus, establishing the use of composite materials as an essential tool for improving aircraft sustainability.

### 1.1.2. Polymer Matrix Composites in Aerospace

A composite is a multiphase material combining useful properties of its constituent phases, typically the matrix and the dispersed phase. The properties of a composite depend on the characteristics, amounts, and geometry of these phases. Composites can be classified by the geometry and orientation of the dispersed phase (e.g., particles, fibres, structures) or by the matrix material (e.g., metal, ceramic, polymer) (Callister, William D. & Rethwisch, 2018a). Polymer Matrix Composites (PMCs) with high-modulus and high-strength fibres are increasingly used in aerospace due to their low density, high strength and stiffness, and processing flexibility. This allows significant weight savings without compromising structural integrity (Mallick, 2017a). For example, the Boeing 787 Dreamliner uses about 50% PMCs, compared to 3% in the Boeing 767, reducing aluminium alloy use from 77% to 20%. Similarly, the Airbus A350 XWB uses 53% composites, cutting operational costs by 8% compared to the Dreamliner (Zhang et al., 2023). Carbon fibres, renowned for their exceptional modulus and strength, are the primary reinforcement in aerospace composites, leading to the dominance of carbon fibre-reinforced polymer (CFRP) composites in aircraft like the Boeing 787 and Airbus A350. The matrix in these composites transfers loads to the fibres and protects them from environmental damage, with properties like melting point and viscosity crucial for processing (Mallick, 2017a). CFRP composites use either thermosetting or thermoplastic polymers. Thermosets, with strong covalent cross-links, are generally stronger and harder, making them preferred for high-performance aerospace applications. Despite thermoplastics comprising 40% of the composite market, they account for less than 5% of aerospace applications (Hamerton & Mooring, 2012). Thermosetting resins, especially epoxy resins, dominate due to their high strength-to-weight ratios, good thermomechanical performance, favourable adhesion, chemical resistance, and low shrinkage (Liu et al., 2021). Epoxy resins are used in about 90% of CFRP composite matrices in aerospace (Hamerton & Mooring, 2012).

### 1.1.3. Negative Impact of Epoxy Resin Production

Epoxy resins are cured through polyaddition, involving the reaction of an epoxy monomer, such as bisphenol A diglycidyl ether (BADGE), with a hardener like diaminodiphenylsulfone (DDS). The aromatic structures of these compounds enhance the thermomechanical properties of the cured resin (Dyer & Kumru, 2023). DGEBA is synthesised from bisphenol A (BPA) and epichlorohydrin in an alkaline environment (Auvergne et al., 2014). Epichlorohydrin can be obtained from bio-based sources (AGC Chemicals, 2024), but BPA is derived from petroleum products (LibreTexts, 2024). Although BPA is beneficial for producing strong, high-quality epoxy monomers, its petroleum origin and associated health risks present significant challenges. BPA is linked to

adverse health effects, including fertility issues and cancer, and is classified as an endocrine disruptor. Consequently, BPA is banned in various consumer products in the EU (EEA, 2023a). The aerospace industry's goal of net-zero operations necessitates eliminating crude oil-sourced materials like BPA. Given that 90% of commercial epoxy resins are BPA-based, finding alternatives is crucial for environmental and health reasons (Auvergne et al., 2014).

#### 1.1.4. Alternatives to BPA

The limitations of petro-sourced polymers, combined with shifting societal priorities, have driven growing interest in replacing traditional epoxies with sustainable bio-based alternatives. These resins can be synthesised from renewable sources such as plant oils, vanillin, eugenol, cardanol, furan, and rosin. Ideally, sustainable thermosets should be both renewable and biodegradable; however, high performance remains critical for aerospace composites, rendering many bio-feedstocks unsuitable. Resveratrol, a trifunctional phenol derived from renewable sources such as grapes and knotweed, shows promise as a BPA substitute for epoxy resins. Its stilbene aromatic structure provides excellent thermal stability and mechanical properties, while its three hydroxyl groups enable effective chemical modifications during curing. Moreover, resveratrol offers health benefits, including anticancer properties and cardiovascular protection. Despite its potential, few studies focus on resveratrol-based epoxy resins, particularly from an engineering and manufacturing perspective. Current research mainly characterises resveratrol chemically, with limited attention to its use with aerospace-grade hardeners or its mechanical properties in composites.

### 1.2. Thesis Outline

This thesis is organised into several chapters, providing a comprehensive overview of the research problem, methodology, and conclusions. Sections 2 and 3 form the core literature review. Section 2 introduces composite materials and their significance in the aviation industry, discussing their constituents and environmental drawbacks, with an emphasis on sustainable epoxies as a promising research area. Section 3 delves into epoxy resins, explaining their chemistry and limitations. It also explores bio-based epoxies as a potential solution to the environmental challenges posed by industrial epoxy resins. Finally, this section highlights resveratrol as a bio-sourced epoxy monomer with significant potential for use in sustainable, high-performance composites. Following the literature review, Section 4 summarises the main research goal of the thesis and outlines the objectives that must be completed. Furthermore, it introduces the main research questions that will be answered at the end of the study. Section 5 investigates various properties of resveratrol-based resin and draws a comparison with petroleum-based commercial analogues. Section 6 explores the application of resveratrol-based epoxy as a matrix material in PMCs. Once again, several important matrix properties are analysed. Finally, Section 7 presents a more detailed discussion of the results followed by the conclusions of the study, while Section 8 gives recommendations on future work.

## 2. Composite Materials

### 2.1. Introduction to Composites

Composite materials, as a distinct class of engineering materials, are generally accepted to have emerged in the mid-twentieth century. Following the discovery of a commercially viable method for manufacturing fibreglass on an industrial scale, the fibres were initially used as a reinforcement phase embedded in resins. Early applications were predominantly military, particularly in World War II fighter planes (Tencom Ltd., 2024). The combination of two discrete material phases during manufacturing led to the recognition of composites as a new class of materials distinct from polymers, alloys, and ceramics. Unlike naturally occurring composites, a composite is defined as an artificially created material consisting of at least two dissimilar phases separated by a distinct interface (Callister, William D. & Rethwisch, 2018a). Another definition of a composite, as proposed by Reinhart (Reinhart, 1998a), supplements the previous definition with a requirement for macroscopic combinations of distinct phases. Thus, in the present context, composites are artificially-made heterogeneous materials composed of two or more distinct macroscopic phases, separated by a discrete interface.

Generally, composites consist of two main phases: matrix and dispersed phase. As mentioned in the introduction, the combined action of two phases allows to achieve a favourable combination of properties, not obtainable by the individual constituents (Reinhart, 1998a). The dispersed phase can also be referred to as the reinforcement or the discontinuous phase. It is the discontinuous phase, from which the main engineering properties (e.g., strength, stiffness, etc.) of a composite material are primarily derived. The type of and the extent to which a material property is improved depends on the geometry, orientation and volume fraction of the reinforcement phase (Callister, William D. & Rethwisch, 2018a). At the same time, the matrix serves as a base material holding the discontinuous phase in place, enabling internal load transfer in the composite (such as between particles and fibre bundles), protecting it from the mechanical and chemical influence of the environment, and providing impact resistance. In the case of fibre-reinforced composites, it also impacts the compressive properties of a composite by preventing the buckling of the fibres (Reinhart, 1998a). Moreover, the shear strength of the matrix directly influences the quality of the bonding interface between the matrix and reinforcement. Therefore, although increasing the volume fraction of the reinforcement leads to increased mechanical properties of the composite, it is limited by the ability of the matrix to sufficiently support the discontinuous phase and transfer the loads. A reduction in the matrix phase can lead to significantly lower composite properties (ASTM, 2022d).

Accordingly, it is common to classify different types of composites based on their constituents. A simple classification system is based on the matrix material, in which composites are divided into ceramic, metallic and organic matrix composites. The latter is further subdivided into carbon and polymer matrix composites. An alternative and more common classification system is based on the reinforcement and separates the composites depending on the geometry and orientation of the dispersed phase. The summary of the classification scheme can be found in Figure 1. The system

involves the division of composites into three main categories: particle-reinforced, fibre-reinforced and structural.

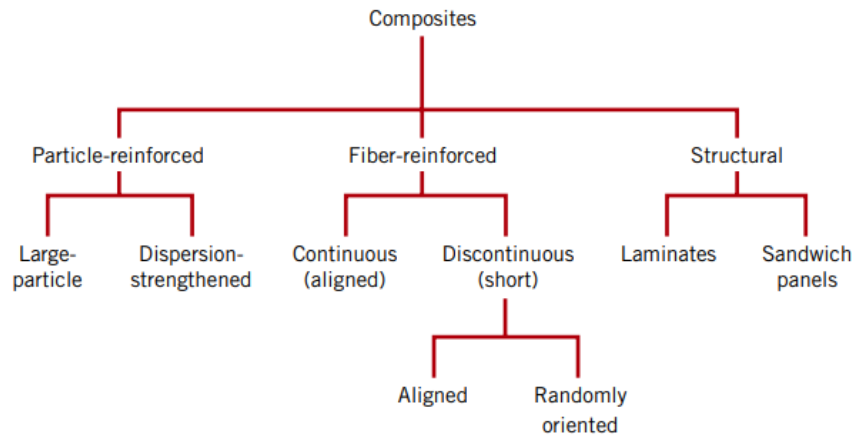


Figure 1. Composite classification based on the reinforcement type (Callister, William D. & Rethwisch, 2018a)

The discussion in the following chapters is limited to fibre-reinforced composites, which are the most commonly used type of composites in aerospace structural applications. Moreover, fibre-reinforced polymer matrix composites (PMCs) have become increasingly used in automotive, consumer, aerospace, and other applications. The more widespread adoption of PMCs in various industries, when compared to metal and ceramic matrix composites, is owed to superior specific strength and modulus characteristics (Mallick, 2017a). Therefore, the following discussion is also limited to composites containing polymer matrices.

## 2.2. Fibre–Matrix Interface in PMCs

As compared to particle-reinforced composites, fibre-reinforced PMCs are engineered for high-performance applications that demand superior strength and stiffness while minimising structural mass. They are further classified into continuous and discontinuous (short) fibre composites. Generally, discontinuous-fibre PMCs exhibit inferior mechanical properties compared to their continuous counterparts. However, they can be fabricated using production methods for pure polymers (e.g., injection moulding) and thus can be made very cheaply (Chou, 1992). The difference between the two categories is related to the parameter known as the critical length ( $l_c$ ), which is to be discussed further below. Normally short fibres are referred to as those having a length of less than  $15l_c$ , while those that are longer are known as continuous (Callister, William D. & Rethwisch, 2018a). For a fibre to distribute load efficiently across its surface and thereby enhance the composite's stiffness and strength, it must exceed the critical length. If a load case similar to the one illustrated in Figure 2 is assumed, it can be concluded that the load transfer from the matrix to the fibre occurs as a result of shear stress developing over the surface of the fibre. This shear stress is balanced by the resulting tensile stress in the fibre. Thus, the quality of the interfacial bond between the matrix and the fibre becomes of significant importance. Since there is no shear stress at the extremity of the fibre, the tensile stress at the fibre end also remains zero

(Matikas, 2007). This leads to matrix deformation as illustrated in Figure 2. Following the load balance in shear-lag analysis, the tensile stress in the fibre increases from zero at the ends to a maximum value at the centre (Withers, 2000).

The influence of fibre critical length on the effectiveness of load transfer to the fibre can be seen from Figure 3. Assuming that the fibre length is equal to ( $l_c$ ) and the applied load is equal to the ultimate tensile strength (UTS) of the fibre ( $\sigma_f^*$ ), the load distribution over the length of the fibre is equivalent to Figure 3 (a). In case the fibre length is above the critical length, the load distribution presented in Figure 3 (b) results. It can be concluded that in the case of (a), the maximum load-carrying capacity of the fibre is utilised only at the axial centre. However, in the case of (b), the maximum fibre load region is extended. As a result, more load is transferred to the fibres away from the relatively weak matrix. It should also be mentioned that in case the fibre length is below the critical length value, the load at the axial centre never reaches the UTS of the fibre. Therefore, the load-carrying capacity of the fibre is not fully utilised (Callister, William D. & Rethwisch, 2018a).

The value of the critical length for a fibre-matrix combination can be calculated using the Kelly-Tyson equation:

$$l_c = \frac{\sigma_f^* d}{2\tau_c} \quad (1)$$

where  $l_c$  – critical fibre length;  $\sigma_f^*$  - fibre UTS;  $d$  – fibre diameter;  $\tau_c$  – bond strength between fibre and matrix.

In this equation, an assumption can be made that the bond strength  $\tau_c$  is equivalent to the shear strength of the polymer matrix. As the shear strength increases, the critical length decreases, allowing for more efficient load transfer at shorter fibre lengths (Matikas, 2007). As can be concluded from the discussion above, the mechanical properties of the composite are influenced not only by the fibre properties but also by the properties of the matrix. Various tests can be performed on a composite sample to quantify the quality of the fibre-matrix interface, such as an inter-laminar shear strength (ILSS) and in-plane shear strength (IPSS).

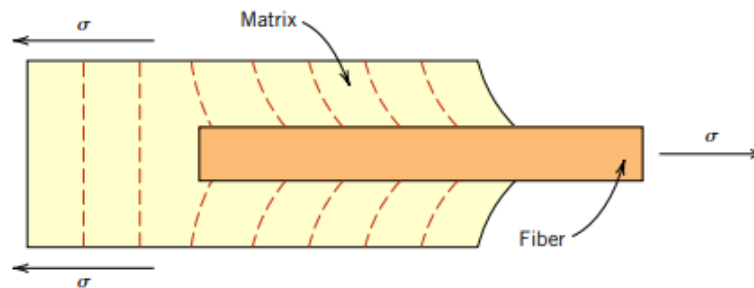


Figure 2. Fibre-matrix interaction under applied load (Callister, William D. & Rethwisch, 2018a)

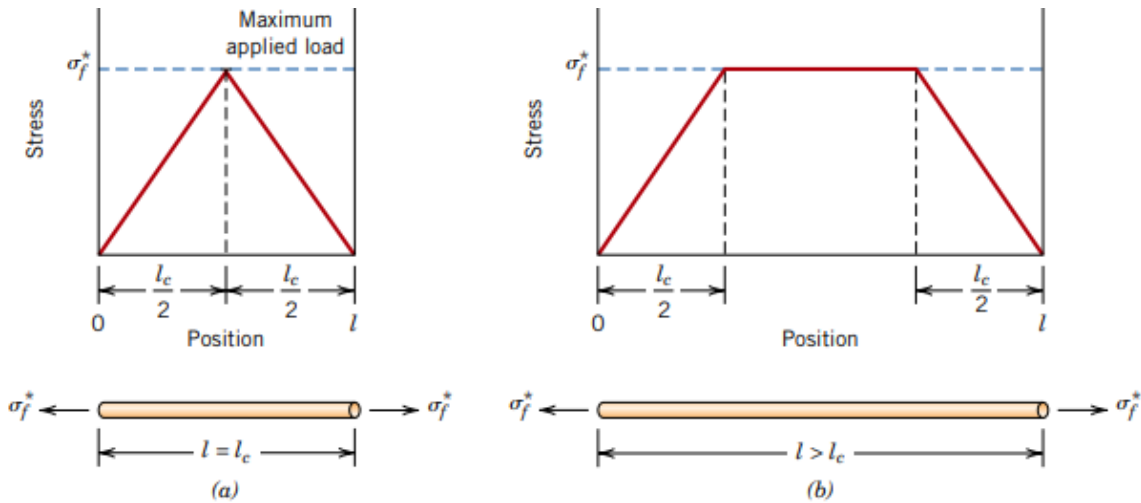


Figure 3. Influence of the fibre length on the effectiveness of load transfer (Callister, William D. & Rethwisch, 2018a)

### 2.3. Dispersed Phase Overview

As discussed in the previous paragraph, the continuous-fibre PMCs have the advantage of more efficient load distribution over the fibre length. Thus, they are generally more preferred in high-performance aerospace applications. For this reason, further discussion is limited to this specific type of fibre composites. Furthermore, it is possible to further distinguish the fibres based on their origin. The fibres used in PMCs can be classified into two main groups: synthetic and natural. In turn, synthetic fibres can be organic, such as aramid, or inorganic, such as carbon and glass. The latter two types form the majority of applications in the aerospace industry. The properties of some commonly used organic and synthetic fibre types are given in Table 1.

The growing adoption of PMCs in modern aircraft production is driven by the superior specific properties of fibre materials. Consequently, their usage has risen significantly over the past two decades. With the introduction of the Boeing 787 Dreamliner, the utilisation of PMC materials reached about 50 wt% in the airframe, tail wing, flap, and wing structures, as compared to only 3 wt% in the flaps of Boeing 767. At the same time, the use of aluminium alloy in the primary structures was reduced from 77 wt% to 20 wt%. Similarly, the launch of the Airbus A350 XWB in 2005 saw a record amount of composite materials being used in the production of commercial airliners, equaling 53 wt%. As a consequence, the total operational costs of the plane were reduced by 8% relative to the Boeing 787 Dreamliner (Zhang et al., 2023).

Carbon fibres can be produced using either PAN (polyacrylonitrile) or pitch precursors. As can be seen from Table 1, the PAN-based carbon fibres possess the best tensile strengths, while some of the pitch-based fibres obtain very high modulus values. Where the use of carbon fibres is redundant based on cost and performance considerations, it is possible to use glass fibres. They provide superior economy and still have an advantage over some traditional aluminium alloys in terms of specific properties. However, it is the organic fibres, specifically aramid (also known under the trademarked name “Kevlar”), that provide the best specific strength values. In combination with

the superior impact properties of Kevlar than both carbon and glass fibres, the organic fibres have found application in some aircraft components with a higher probability of impact damage (e.g., leading edges, landing gear, engine nacelles, etc.). However, their use is also limited by their low compressive properties and high sensitivity to environmental conditions, especially moisture content and sunlight exposure (Khusiafan, 2018).

Type of fibre	Tensile Strength (Mpa)	Tensile Modulus (Gpa)	Strain at Failure (%)	Density (g/cm <sup>3</sup> )
<b>Glass</b>				
E-Glass	3450	76	4.7	2.58
S2 Glass	4500	87	5.6	2.48
Quartz	3400	69	5.0	2.15
<b>Organic</b>				
Kevlar 29	3620	83	4.0	1.44
Kevlar 49	3800	131	2.8	1.44
Spectra 1000	3100	172	0.7	0.97
<b>PAN-based CF</b>				
Standard Modulus	4140	231	1.85	1.80
Intermediate Modulus	5170	286	1.65	1.80
High Modulus	4830	396	0.85	1.90
<b>Pitch-based CF</b>				
Low Modulus	2240	207	0.9	1.90
Ultra-high Modulus	2400	827	0.3	2.20

Table 1. Properties of common PMC fibre materials and aerospace-grade aluminium alloys (Callister, William D. & Rethwisch, 2018a)

## 2.4. Matrix Phase Overview

As addressed in Section 2.2, the matrix phase plays a significant role in defining the properties of the polymer matrix composite. Specifically, it has a direct impact on the fibre alignment, load transfer between the fibres, and protection from environmental effects. The matrix properties significantly influence the composite's compressive and shear characteristics. Variations in the matrix properties due to temperature changes or moisture absorption directly affect these properties (Reinhart, 1998b). Additionally, such composite characteristics as flammability and environmental resistance (e.g., to sunlight exposure, to the humid atmosphere, etc.) are extensively affected by the matrix material.

When considering the processing stage of a PMC, it is also important to consider the influencing parameters of the matrix. Thus, it is essential to quantify properties, such as the viscosity of the resin and its temperature dependence. This enables a proper selection of the processing temperature and ensures good fibre wetting. For thermoset resins, the processing temperature must be selected to avoid premature curing of the resin. Therefore, the cure kinetics of the resin must be quantified to define the activation energy and curing onset. Resin degradation is another factor that should be

considered both during processing and operation. For high-performance applications, the resin must be able to sustain the operational temperatures.

Table 2 gives common polymers used as matrix material along with their main characteristics. As can be seen from the table, the polymers can be subdivided into two main categories: thermosets and thermoplastics. Both of the types consist of long-chain molecules with many repeating units. The main molecular difference is that thermosetting polymers have chemically connected or cross-linked molecules, whereas thermoplastic polymers lack these chemical connections (See Figure 4).

Polymer	Density (g/cm <sup>3</sup> )	Tensile Modulus (GPa)	Tensile Strength (MPa)	Strain at Failure (%)	Glass Transition Temperature, $T_g$ (°C)	Maximum Service Temperature (°C)
<b>Thermosetting Polymers<sup>a</sup></b>						
Epoxies	1.2–1.3	2.75–4.1	55–130	1.5–8	150–260	125
Polyesters	1.1–1.4	2.1–3.5	35–104	1–7		60–150
Vinyl esters	1.12–1.32	3–3.5	73–81	3–8		60–150
Bismaleimides	1.2–1.32	3.2–3.5	48–110	1.5–3.3	230–290	232
Polyurethanes	1.21	0.7	30–40	400	120–167	
<b>Thermoplastic Polymers</b>						
PEEK	1.30	3.7	110	25	143	260
PPS	1.35	3.45	93	15	85	218
Polyetherimide	1.28	3.45	117	60	210	171
Polyamideimide	1.42	4.5	150	8	275	
PP	0.90	1.5	36	>100%	–10	50–75
Polyamide-6	1.13	3.10	80	50	60	

<sup>a</sup> Properties of thermosetting polymers are given in ranges, since they depend on the chemical structure of the polymer and the curing condition.

Table 2. Properties of common polymers used in PMCs (Mallick, 2017a)

#### 2.4.1. Thermoplastic Polymers

Thermoplastic polymers consist of long molecule chains formed by connecting a repeated unit, also referred to as a monomer, which constitutes the polymerisation process. The monomers in each molecule form strong bonds with each other, known as the covalent bonds. However, there are no such bonds formed between different molecule chains. Instead, the chains are connected via intermolecular entanglements held together by relatively weak secondary forces (i.e., Van der Waals forces, hydrogen bonds or  $\pi$ - $\pi$  interactions) (Maiti et al., 2022). Most thermoplastic polymers are semi-crystalline, possessing both amorphous and crystalline regions. Semicrystalline polymers usually contain numerous spherulites, with each spherulite's centre being the nucleation site for crystalline phase growth.

Semicrystalline thermoplastics undergo several physical transitions under changing thermal environments. As the temperature increases, the polymer undergoes the first transformation from a hard solid material to a soft rubbery solid. This transition is known as the glass transition temperature ( $T_g$ ), which, in reality, represents a range of temperatures over which the

aforementioned transition takes place. This region is characterised by a sudden drop in the storage modulus of the polymer. To be more specific, it should be noted that only the amorphous regions undergo the glass transition. As the temperature of the material is further increased, it eventually reaches the melting point ( $T_m$ ), which corresponds to the melting of the crystalline phase of the polymer. Thus, the properties of a thermoplastic depend on the degree of crystallinity. On cooling down to the ambient conditions, both amorphous and crystalline regions revert to their original state, restoring the mechanical properties, such as modulus and hardness (Mallick, 2017a).

#### 2.4.2. Thermosetting Polymers

Having described the chemical and physical nature of thermoplastic polymers, it is possible to address the differences between them and thermosetting polymers. In contrast with thermoplastics, thermosets form a network of polymer chains inter-connected with the help of strong covalent bonds. These bonds are referred to as cross-links and cross-linked polymer can be represented as an amorphous three-dimensional network, which inhibits the movement of polymer chains and prevents closer packing and crystallisation. The formation of cross-links can proceed at room temperature but is accelerated at elevated temperatures. The usual temperature range for curing some of the common thermosets is 120-180°C. Moreover, the presence of a curing agent is required to initiate the chemical reaction (Maiti et al., 2022). The absence of crystalline regions is marked by changes in the thermal behaviour of the thermosetting polymer. Thus, unlike thermoplastics, thermosets do not have a defined melting temperature. Instead, if the temperature is high enough, the polymer will eventually start to char and ultimately disintegrate. However, thermosets still possess a  $T_g$ , upon which the polymer will soften and exhibit rubber-like behaviour, which can be hard to define for highly cross-linked networks (Mallick, 2017a).

Due to the differences in chemical structure, the processing of thermosets also differs from that of thermoplastics. Due to the formation of a rigid cross-linked network and the absence of a melting point, the polymer cannot be brought back to a liquid state upon secondary heating. Therefore, the shape of the polymer cannot be changed much post-curing, which limits the recycling potential. However, the advantages of thermosets which made them abundantly used in the aerospace industry include superior thermal stability, creep resistance, modulus, and chemical resistance when compared to thermoplastics (Maiti et al., 2022). Finally, the significantly lower viscosity of thermosets enables versatile manufacturing methods for composites and simplifies processing, as compared to thermoplastics.

Although thermoplastic matrices account for approximately 40% of the composite market, when it comes to high-performance applications (such as aerospace), the share of thermoplastics is less than 5%. Consequently, thermosetting resins are by far the most widely used matrix material in the aerospace industry. The status quo came into being as a result of historical (thermosets first adopted by the industry; long certification periods for new materials) and performance-related (high strength-to-weight and modulus-to-weight ratios) reasons. At the same time, the most widely used polymer system for CFRP composites in the aerospace industry is epoxy resin, which accounts for about 90% of the CFRP composite matrices (Hamerton & Mooring, 2012). It offers good thermomechanical performance, favourable adhesion properties, good chemical resistance and

enhanced processability. The properties and advantages of epoxy resins are discussed in more detail in Section 3.3.

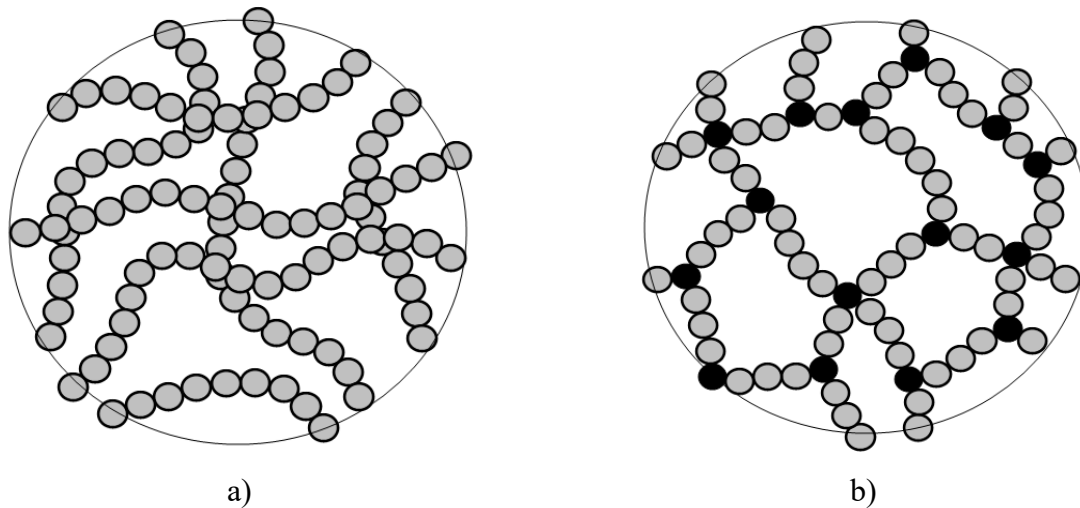


Figure 4. Representation of a) thermoplastic molecule and b) thermosetting polymer molecules (Wikipedia, 2024e)

## 2.5. Environmental Burden of PMCs

### 2.5.1. Carbon Fibres

While the current study is focused on the environmental impact of matrix materials, a brief overview of sustainability issues resulting from the use of carbon fibres in PMCs is presented in this section. Since these issues are outside of the scope of this study, they will not be discussed any further.

Despite the direct benefits of PMCs to the efficiency of modern aircraft and, as a consequence, the improved operational sustainability resulting from lower emissions, there are still major concerns regarding other stages of the PMC lifecycle. Specifically, the manufacturing and disposal of carbon fibres pose significant environmental and health risks. More than 90% of commercial carbon fibres are made from crude oil derivatives, namely PAN and Pitch. The PAN precursor is made via polymerisation of acrylonitrile, which, in turn, is made with the help of propylene, which is a by-product of petroleum refining (NIH, 1994). Similarly, pitch is obtained from the coal or petroleum distillation process. Production of carbon fibres from lignin is possible but is not as cost-effective and inferior in terms of mechanical properties. On top of that, PAN is a known carcinogen which can have a detrimental effect on various organs in the human body, including the eyes, lungs and nervous system (CDC, 2024). Similarly, the use of dimethylformamide (DMF) to dissolve PAN at the starting stage of carbon fibre production is associated with permanent liver damage when handled without care. Furthermore, the production of carbon fibres is an energy intensive process. The embodied energy of carbon fibre, which is the amount of energy used to produce a unit mass of a given material, is calculated to be between 183 and 286 MJ/kg (110-210 MJ/kg for stainless

steel and 190-257 MJ/kg for aluminium alloys) (TinyEco, 2024). Finally, carbon fibres are not biodegradable, however, they can be recycled from the used composite materials by subjecting them to pyrolysis to decompose the matrix. It should be mentioned though that this process usually leads to the degradation of the mechanical properties of the fibres and they cannot be used for high-performance purposes (CCUK, 2022).

### 2.5.2. Epoxy Resins

Since epoxy resin is the most common matrix type in PMCs, it is necessary to discuss the synthesis and chemicals that are used in the production of such resins. Epoxy resins can be cured via the step-growth polymerisation process which involves the reaction of an epoxy monomer and a curing agent (Auvergne et al., 2014). The curing agents are discussed in more detail in Section 3.2.

Diglycidyl ether of bisphenol A (DGEBA or BADGE) is the most commonly used monomer for epoxy polymerisation and is estimated to cover around 75% of industrial needs (Sukanto et al., 2021). Typically, DGEBA is derived from the reaction of Bisphenol A (BPA) and epichlorohydrin (Auvergne et al., 2014). While epichlorohydrin can be industrially acquired from bio-based sources (AGC Chemicals, 2024), BPA is usually derived from petroleum products. The chemical reaction used for the synthesis of epoxy monomer and the starting materials are discussed in more detail in Section 3.1.

The use of BPA is motivated by the strong and rigid structure imparted by the aromatic nature of the starting material, as well as by the well-established industrial processes leading to cheap and high-quality epoxy monomers. Nevertheless, the industrial utilisation of BPA was established more than seventy years ago – in the times when the aspects of environmental sustainability had not been considered and the impact of BPA on human health had not been extensively researched (Vogel, 2009). As a result, the modern world is faced with several issues concerning the use of BPA in industry. First of all, the petroleum-based nature of BPA is not compatible with the concepts of environmental protection and fossil fuel depletion. Specifically in the case of the aerospace industry, achieving net zero operations requires the elimination of crude oil-sourced materials in the production of modern aircraft. The synthesis of BPA from phenol and acetone fails to satisfy that principle (LibreTexts, 2024).

Secondly, the use of BPA has been associated with multiple health and safety hazards. In the European Union (EU) it has been classified as a highly toxic substance having adverse effects on human fertility and the health of an unborn child (ECHA, 2024). It is also recognised as an endocrine disruptor which can damage the normal functions of the hormone system. The potential outcomes of such disruptions can be breast tumour and prostate cancer, infertility, as well as multiple metabolic disorders (EEA, 2023b). For more specific information about the adverse effects of BPA on human health, the reader is referred to the literature study conducted by Rochester (Rochester, 2013). As a result, the use of BPA has been banned in various items, such as paper receipts, plastic bottles, packaging for baby food, food containers, etc (EFSA, 2023). The potential negative impact of BPA becomes more obvious when taking into consideration the fact

that about 90% of commercial epoxy resins are produced from the substance (Auvergne et al., 2014).

Finally, the disposal of composites with epoxy matrices at the end of service life presents itself as a serious issue. The highly crosslinked network of epoxies is responsible for many of their superior properties. However, as a result of the crosslinks, the epoxies cannot be re-processed/re-moulded or decomposed under mild conditions. Therefore, to allow for any degree of recyclability of the PMC, it is necessary to employ one of the available strategies. Mechanical grinding is one option for PMC recycling. Another strategy is thermal recycling which burns the epoxy resin, thus, separating the fibres which can be re-used. On top of that, it is possible to use chemical recycling to decompose the matrix using solvents. Each of the aforementioned techniques is inherently unsustainable. As such, thermal decomposition requires large amounts of energy to be supplied, while chemical recycling involves various toxic materials which are often petroleum-based. These strategies aim at removing the matrix material and saving the fibres for future re-use. However, the use of such techniques unavoidably leads to the degradation of the fibres due to the extreme conditions of each process. Thus, the recovered fibres are most probably to be used in applications that require lower performance (Sukanto et al., 2021). As a result of energy and resource intensity, high cost, and inefficiency of these recycling technologies, only a small fraction of composites are recycled each year. For instance, only 15% of PMCs are recycled at the end of life in the UK (Maiti et al., 2022).

## 2.6. The Importance of Sustainable Thermoset Research

### 2.6.1. Matrix versus Fibres

Due to the reasons described in Section 2.5.1, the production and use of carbon fibres in PMCs can have a detrimental effect on the environment. This is also true for other types of synthetic fibres (i.e., glass and aramid) that have been mentioned but not extensively discussed in this paper. As a result of environmental concerns associated with synthetic fibres, significant attention from the scientific community is devoted to the research of possible natural fibre alternatives. The purpose is to develop sustainable, lightweight and biodegradable fibres for structural composite applications. These criteria constitute multiple requirements, such as low water and energy consumption during production, bio-based starting materials and mechanical properties comparable with synthetic fibres (Maiti et al., 2022). Some of the researched alternatives include jute (Chandekar et al., 2020), flax (More, 2022), bamboo (Hasan et al., 2023), sugarcane (Kusuma et al., 2023) and others.

Although the research has resulted in some success, the use of natural fibres in PMCs is still severely limited due to a number of inherent challenges of natural feedstock. Some of the main issues identified include high moisture absorption, low durability, low to moderate mechanical properties, and inconsistency of fibre dimensions (Maiti et al., 2022). Consequently, as of the time of writing of this paper, the use of natural fibres in high-performance aerospace applications is neither conceivable nor practical.

On the other hand, the research of bio-based matrix materials in structural aerospace composites has the promise to alleviate some of the environmental issues of PMCs, as described in Section 2.5.2. At the same time, the use of bio-based matrices does not come at the cost of reduced mechanical properties of the composite. In fact, as will be demonstrated in the following chapters, in addition to improved sustainability, naturally sourced matrix materials can also improve the mechanical performance of composites.

## 2.6.2. Thermosets versus Thermoplastics

As mentioned in Section 2.4.1, thermoplastic polymers have the advantage of recyclability due to their molecular structure. Due to this characteristic, a significant part of the available literature on sustainable matrix material is devoted to thermoplastics. At the same time, significantly less attention is dedicated to sustainable thermosets.

However, the same chemical structure that makes thermoplastics easily recyclable has a negative impact on some of its mechanical properties, including creep resistance and thermal stability (Please refer back to Section 2.4 for more details).

Although thermoplastics can be easily re-cycled by melting and shaping them into a new desired form, this benefit cannot be fully utilised in aerospace composite applications due to a reduction of mechanical properties with every re-melting cycle.

# 3. Epoxy Resins

## 3.1. Epoxy Monomers

Epoxy monomers are defined as low-molecular-weight pre-polymers formed from an oligomer consisting of at least two epoxide groups of the form given in Figure 5 and a curing agent, normally an amine or anhydride. They were discovered in 1909 by N. Prileschajew and became available on the market post-WW2 with a primary application as a coating material. Since then, due to their versatile properties, epoxies have become commonly used across a wide range of fields. These include structural fibre-reinforced materials, encapsulating materials, high-performance coatings, general-purpose adhesives, and others.

The majority of commercial epoxy monomers are synthesised by the reaction of a compound containing an acidic hydroxyl group with epichlorohydrin. Initially, a coupling reaction takes place between the hydroxyl group and epichlorohydrin. It is then followed by a dehydrohalogenation process in a basic environment. The process is illustrated in Figure 6. The hydroxyl group can be derived from polyphenolic compounds, amines, aliphatic diols, and others. Epoxy resins obtained from epichlorohydrine are referred to as glycidyl-based.

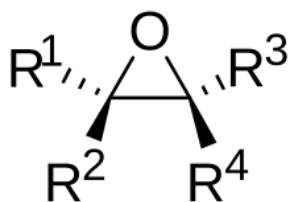


Figure 5. Epoxide functional group (Wikipedia, 2024d)

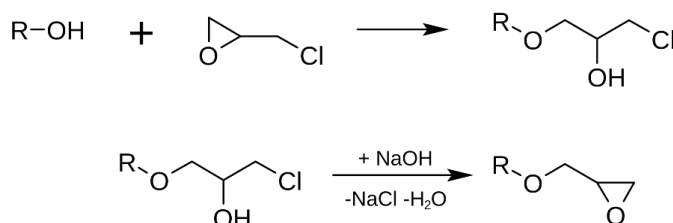


Figure 6. The reaction of a hydroxyl group and epichlorohydrin, followed by dehydrohalogenation (Wikipedia, 2024d)

### 3.1.1. DGEBA Monomer

DGEBA, the most common glycidyl-based epoxy resin monomer, is synthesised from bis(4-hydroxyphenylene)-2,2-propane (commonly known as Bisphenol A or BPA) and epichlorohydrin in the presence of sodium hydroxide. The reaction is given in Figure 7.

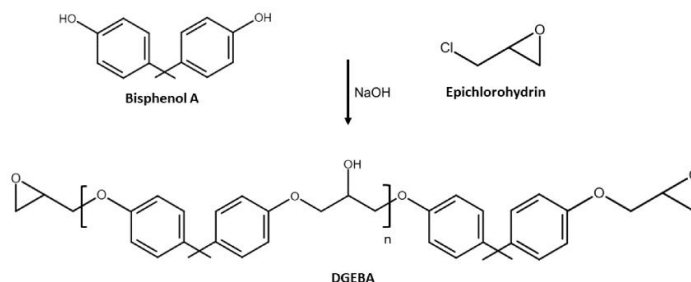


Figure 7. Formation of DGEBA from BPA and epichlorohydrin (Capretti et al., 2023)

### 3.1.2. Tactix 742 Monomer

A trifunctional epoxy resin monomer, tri-glycidyl ether of tris(4-hydroxyphenyl)methane (or THPMTGE), can be prepared by reacting 3 hydroxyl groups of a tris(4-hydroxyphenyl)methane (THPM) molecule with epichlorohydrin. As a result of this glycidylation reaction, the hydroxyl groups are converted into glycidyl ethers (Hughes & Than Tun, 2019). Overall, its synthesis process is similar to that of BADGE. It is used as a structural adhesive and in composite applications which require higher thermomechanical performance (Huntsman Corporation, 2012). The structure of the resulting epoxy resin monomer is given in Figure 8.

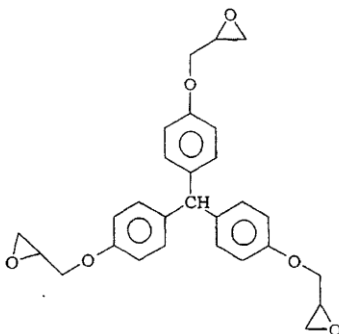


Figure 8. Structure of Tactix 742 epoxy resin (Hughes & Than Tun, 2019)

## 3.2. Curing Agents

Epoxydes can react with various substances, including amines, alcohol compounds, thiols, and anhydrides (Sukanto et al., 2021). Furthermore, according to J.K. Fink, epoxy curing agents can be divided into three groups: ionic initiators, compounds with active hydrogen, and hydroxyl coupling agents. The first group encompasses the reactions based on polyaddition, which opens the epoxide ring (Fink, 2013). This constitutes the most common reaction type used for curing composite systems, with amines and anhydrides being widely used as reaction initiators (Sukanto et al., 2021).

### 3.2.1. Anhydrides

Epoxy–anhydride systems are characterised by lower viscosity and longer pot life when compared to amines. Additionally, anhydride curing agents tend to exhibit low exothermic heat of reaction, which leads to a lower reaction rate and the need for a catalyst, such as Lewis acid or tertiary amines. To obtain an epoxy resin with satisfactory thermal resistance and mechanical properties, it is necessary to carefully calculate and mix the optimal ratio of anhydride and catalyst. This complicates the processing and requires longer mixing times and precise temperature control (Fink, 2013). Another disadvantage of anhydrides is their hygroscopic nature which further complicates handling and processing and makes them suitable for specific environments. Finally, anhydrides do not have the benzene ring present in the aromatic amines and have generally fewer reaction groups. As a result, they have lower reactivity, mechanical performance and  $T_g$  than the aromatic amine systems. The lack of aromatic groups in most anhydride systems also leads to lower chemical resistance.

As a result of the aforementioned disadvantages, anhydrides are less preferred in high-performance structural composite applications (Sukanto et al., 2021).

### 3.2.2. Amines

Amines can be further subdivided into aromatic, aliphatic and cycloaliphatic compounds based on their nucleophilic reactivity. Out of these, aliphatic amines are the most reactive, while aromatic have the lowest reactivity (Auvergne et al., 2014). Generally, aliphatic amines enable fast curing even at room temperature due to their high reactivity (Tcharkhtchi et al., 2015). However, one of the limitations of the aliphatic systems is the inability to attain glass transition temperatures in excess of 120°C (Sukanto et al., 2021). Cycloaliphatic amines serve as a less toxic alternative for aliphatic compounds. Finally, aromatic amines encompass compounds containing phenyl rings which introduce high rigidity and, consequently, high glass transition temperature to the cured epoxy network. Thus, this type of hardener is common for applications that require high thermal stability and good mechanical properties, such as aerospace-grade composites (Tcharkhtchi et al., 2015).

The curing of epoxy monomers proceeds in accordance with the reactions illustrated in Figure 9. As can be seen from the figure, the reaction happens in three stages. The first stage involves the

addition of primary amine hydrogen with the epoxide (See Figure 9 (a)). The functionality of amines is defined by the number of hydrogen atoms bound to nitrogen. In the case of primary amine, it is equal to 2. Thus, the amine is able to react with two epoxy groups. The product of the initial reaction is the secondary amine, which has only one active hydrogen atom and, thus, reacts with only one epoxy group (See Figure 9 (b)), producing tertiary amines. The product of the second reaction does not possess any remaining hydrogen atoms and, thus, does not react with epoxy groups. However, they contribute hydroxyl groups which lower the activation energy for further epoxide ring-opening (Fink, 2013). In fact, hydroxyl groups are also formed during reaction (a) due to the epoxy ring opening. Therefore, this type of curing reaction is referred to as autocatalytic (Tcharkhtchi et al., 2015).

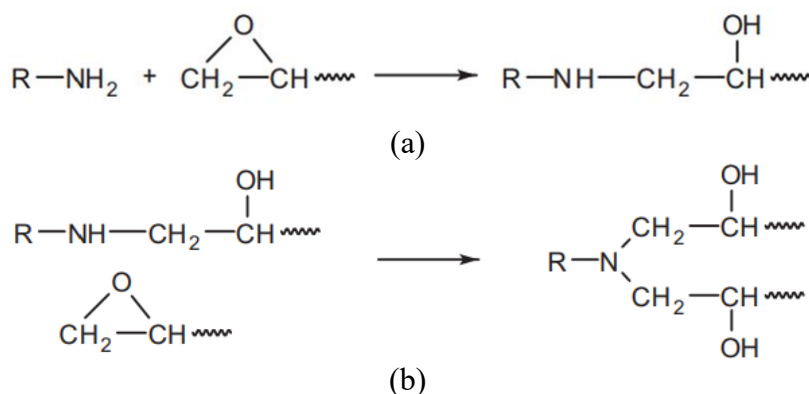


Figure 9. Reaction of glycidyl group with amine curing agent (Fink, 2013)

Figure 10 presents some of the aromatic amines that have been used in industry and research as curing agents for epoxy resins. Overall, all of the presented curing agents provide a good combination of mechanical properties, thermal stability and chemical resistance to the cured resin. DDM possesses a low melting point of around 90°C which enables more homogeneous mixing at lower processing temperatures (CAMEO Chemicals, 2010). At the same time, DDE and DDS have a significantly higher melting point of around 190°C and 176°C, respectively (Huntsman Corporation, 2010a). However, DDM and DDE both pose significant health issues due to their toxicity and may lead to potential occupational cancer, according to the European Chemicals Agency (ECHA) and the National Institute of Health (NIH) (ECHA, 2023). In contrast, DDS provides a significantly safer alternative, as it does not present a carcinogenic risk and poses minimal danger from limited skin exposure (ECHA, 2023). Finally, all the considered aromatic amines are commercially available on the market. DDS can be procured under its commercial name of Aradur 976 in the form of microsized powder which can be dissolved well in Epoxy monomer and form a homogeneous mixture (CAMEO Chemicals, 2010). The other curing agents are available in the form of small crystals which require further milling to obtain fine powder. This poses health concerns due to the aforementioned toxic nature of the chemicals. As a result, DDS is a more common curing agent used in the aerospace industry for the production of epoxy composites (Mallick, 2017a).

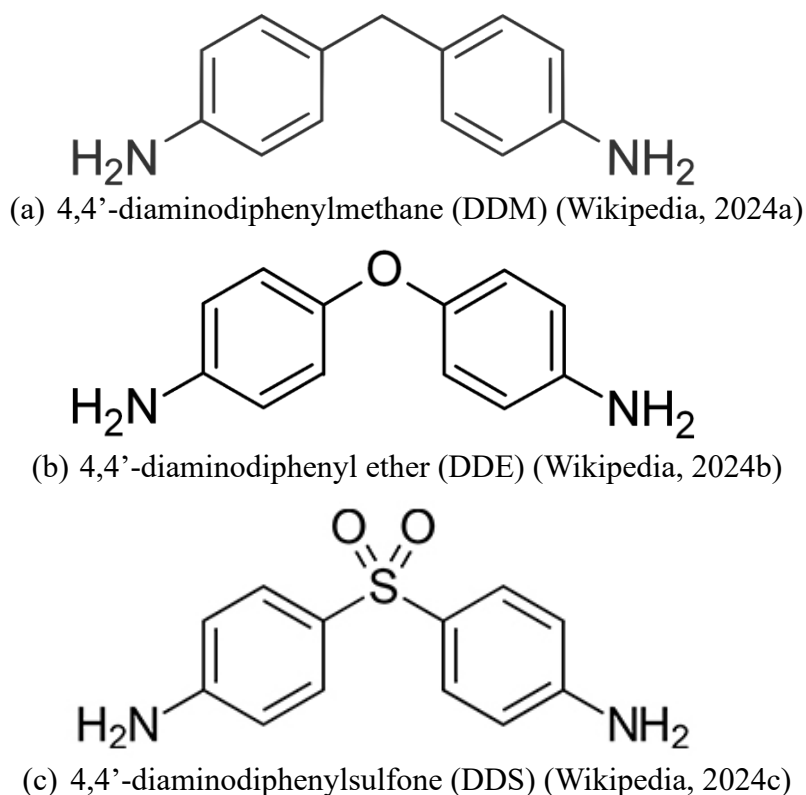


Figure 10. Examples of aromatic amines used in curing of epoxy resins

### 3.3. Advantages of Epoxy Resins

From a chemical perspective, the use of aromatic monomers in epoxy resin production facilitates excellent mechanical properties at elevated temperatures and dimensional stability (i.e., minimal shrinkage). Additionally, the hydroxyl groups formed during curing impart favourable adhesion properties.

In addition, epoxies possess superior chemical resistance owing to the ether linkages present in the molecule (Kumar et al., 2018). At the same time, low shrinkage and relatively high toughness of the resin benefit the processing and performance of the composite. On top of that, the processability is further enhanced due to the liquid nature of the pre-polymers (Liu et al., 2021).

As a result, epoxy resins are widely used across multiple industries owing to their dimensional and thermal stability, chemical and corrosion resistance, as well as excellent mechanical properties. The aforementioned properties can be optimised by adjusting various parameters, such as the curing temperature and time, curing agent and epoxy monomer used.

### 3.4. Limitations of Epoxy Resins

Section 2.5.2 introduced the environmental problems associated with the use of epoxies in polymer-matrix composites. The major concerns are briefly summarised in the following manner:

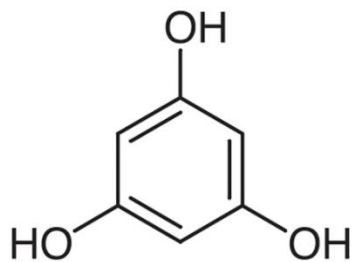
- 1) BADGE is derived from BPA and epichlorohydrin as per the reaction given in Figure 7. BPA is obtained via the process of condensation of acetone and phenol, which are derived from benzene and propylene. The latter two compounds are derivatives of hydrocarbon extraction and refining. Thus, **the production of epoxy monomers and, consequently, aerospace composites is strongly dependent on fossil fuel extraction**, contradicting the principles of sustainable aviation outlined in Section 1.1.1.
- 2) **Utilisation of BPA for large-scale industrial purposes poses significant health risks to people and wildlife** for the reasons discussed in Section 2.5.2.
- 3) Recycling options for epoxy composites are limited to energy-intensive and inefficient processes. **Therefore, the majority of aerospace composites at the end of life are disposed of in an unsustainable manner**, such as by landfilling.

### 3.5. Bio-Based Epoxies

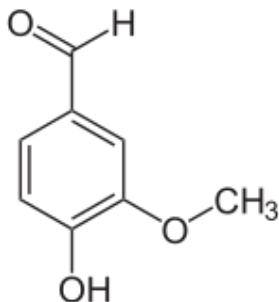
To mitigate the environmental impact of PMCs, various alternative matrix materials have been proposed as substitutes for petroleum-based epoxy resins. The scientific community has divided its attention between several methods of solving the sustainability issue. Active research is conducted on thermoplastic alternatives, reworkable vitrimers, bio-based, and bio-degradable thermosets. These materials can be sourced in different ways, such as from organic waste residues, via microorganisms or from naturally occurring polymers (i.e., cellulose or starch).

The scope of interest of the current paper is limited to bio-based epoxy resins for the reasons described in Section 2.6.2. Bio-based epoxies promise to reduce the carbon dioxide intensity of the PMC manufacturing process by eliminating petroleum-based starting materials. They can improve the cost-efficiency and sustainability of the polymer matrix disposal and recycling, making it a more industrially appealing option. On top of that, the bio-based starting materials are on average significantly less toxic than the petroleum-based monomers. However, to be considered viable for aerospace applications, the bio-based epoxies must also provide adequate thermal, mechanical and thermal performance to the PMC system.

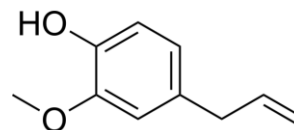
Extensive research has been conducted on the topic of bio-based epoxy monomers. The literature is abundant with papers investigating various formulations with aromatic/aliphatic starting compounds and different types of curing agents. Starting material for epoxy monomers can be procured from different sources, including plant oils, saccharides, phenols, natural resins, lignin derivatives, etc. However, it should be noted that the properties of the cured epoxy resin depend on the chemical structure of the starting material. As such, aliphatic compounds usually exhibit subpar mechanical properties due to the long molecule chains and lack of aromatics. This limits their application as matrix material in high-performance composites. However, they can be used as coatings. Plant oils, such as karanja, soybean and linseed, are some examples of aliphatic starting materials for epoxy formation (Liu et al., 2021). On the contrary, the use of starting monomers with aromatic structures, such as phenols, imparts superior mechanical properties and thermal stability to the epoxy resin. Furthermore, the presence of the alcohol group in the phenolic structures enables chemical modification (Dyer & Kumru, 2023). Figure 11 contains some of the bio-based starting monomers used for epoxy formation.



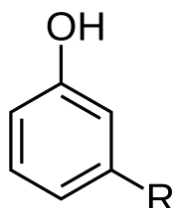
**Phloroglucinol**



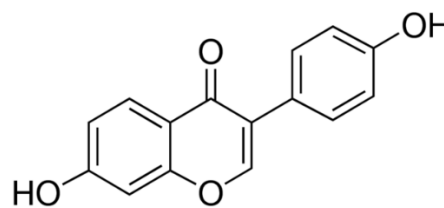
**Vanillin**



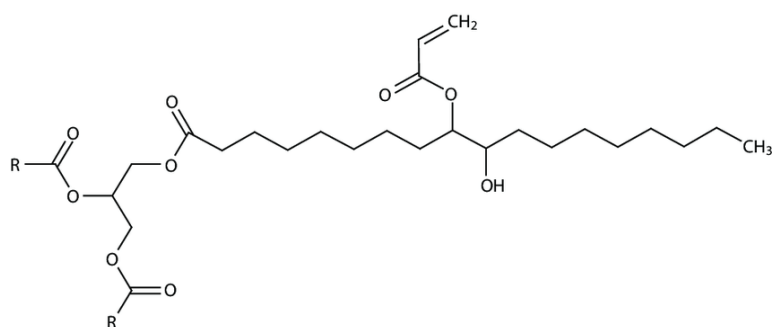
**Eugenol**



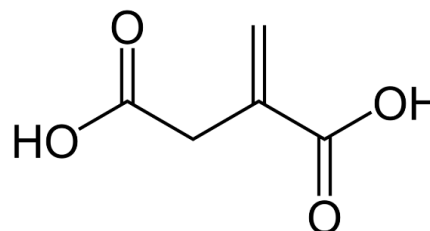
**Cardanol**



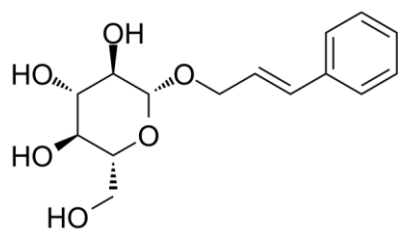
**Daidzein**



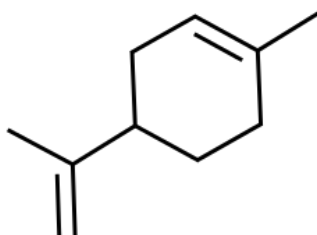
**Soybean Oil**



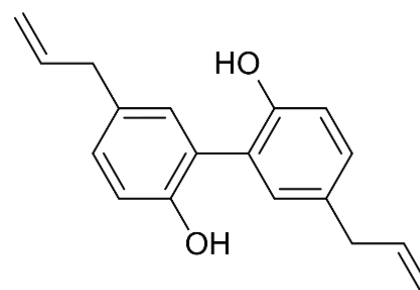
**Itaconic Acid**



**Rosin Acid**



**Limonene**



**Magnolol**

Figure 11. Overview of bio-based molecules used as starting material for epoxy formulation (Wikipedia, 2024f)

### 3.5.1. State of Research of Bio-Based Epoxy Monomers

A study conducted by Apostolidis et al. (2024) investigates the use of phloroglucinol as a starting material for epoxy resin formulation. Phloroglucinol is a phenolic compound that can be obtained in high quantities from brown algae. Epoxidised phloroglucinol (phloroglucinol trisepoxy or PHTE) was mixed with a commercial aliphatic curing agent and used to manufacture glass fibre composite panels. The resin and composites were then compared to a reference epoxy resin based on BADGE. The PHTE resin was found to possess a pot life of 40 minutes, significantly lower than the 300 minutes of the BADGE system, thus, potentially limiting the application of PHTE in industrial composite manufacturing. Thermogravimetric analysis of the PHTE resin demonstrated high thermal stability up to temperatures of 320°C. A mass loss of around 50% was then observed within the next 40°C. The degradation profile of the PHTE resin was found to be superior to that of BADGE resin. The  $T_g$  of the resin was observed to be around 123°C after post-curing. This value was two times higher than for the BADGE resin. On top of that, the PHTE composite panel offered superior tensile and flexural properties when compared to the BADGE panel. However, the PHTE resin possessed a higher moisture intake and density, potentially limiting applications in the aerospace field.

Similarly, multiple studies focused on the application of vanillin as a sustainable monomer for designing bio-degradable and re-processable epoxy resins. As such, Yu et al. (2019) created an epoxy vitrimer by curing the mono-glycidyl structure of vanillin (Van-Ep) with an isophorone diamine (IPDA) hardener. It was found that the vanillin resin is thermally stable up to a temperature of 222°C and possesses a high char yield when compared to the BADGE – IPDA system. However, the overall thermal stability was found to be lower than that of the BADGE. At the same time, the reported glass transition temperature was 109°C, several degrees lower than for the BADGE system. The tensile strength at break of the vanillin system was found to be around 65 MPa, 11.7 MPa lower than for the BADGE system. Most importantly, it was proved that the vitrimers can be reprocessed up to 3 times without noticeable degradation of mechanical properties.

Another study investigated the properties of hydrovanilloin epoxy oligomer cured with various aliphatic diamine curing agents at room temperature. When cured with 1,6-diaminohexane and isophorone diamine (IPDA) curing agents, the achieved  $T_g$  values were 149°C and 146°C respectively, which is comparable with BADGE systems. The degradation onset temperature of diamine-cured resins was around 230°C. Additionally, Shore hardness measurements were performed on the resins showing values of around 76 units, comparable with diamine-cured BADGE resin (Amarasekara et al., 2019).

Furthermore, a vanillin-based Schiff-base epoxy monomer was cured with DFA and demonstrated a relatively high glass transition temperature of 170°C. At the same time, the tensile strength (60 Mpa), elongation (2.8%) and storage modulus (3271 MPa) of the resin were found to be superior to the BADGE-DDM system. The Schiff base structure of the epoxy monomer exhibited good dissolution behaviour in various acids. Thus, vanillin-based resins can be degraded in moderate conditions allowing for more efficient recycling (Nabipour et al., 2021).

Another thermoset resin based on the triglycidyl eugenol derivative (3EPOEU) and bio-based IPDA/Jeffamine was investigated by Santiago et al. (2020). According to the Differential Scanning Calorimetry (DSC) data, 3EPOEU resin obtained lower total enthalpy of reaction when compared to BADGE (90 kJ/mol vs 114 kJ/mol). This is attributed to the compact rigid structure of 3EPOEU which prevents complete cross-linking. Nevertheless, the eugenol-based resin exhibited a  $T_g$  of 174°C when cured with IPDA, which is 50°C higher than the analogous BADGE formulation. This is, once again, explained by the compactness and rigidity of the eugenol molecule, which allows higher crosslinking density. Thermogravimetric Analysis (TGA) revealed that the onset of degradation of the eugenol-based resin (300°C) is slightly lower than in the case of BADGE resin. At the same time, the compactness and rigidity of the 3EPOEU molecule led to higher stiffness (6298 vs 3096 MPa) and hardness (13.9 vs 12.5 HV) values.

Another research group proposed an alternative eugenol-based trifunctional epoxy monomer that had been created by epoxidising the allyl group of each eugenol moiety. The epoxy monomer was cured with DDS, an aromatic amine hardener. The resulting glass transition temperature of the eugenol system was recorded at 241°C, significantly higher than most other bio-based and conventional BADGE formulations. However, it should be noted that the synthesis of the trifunctional monomer involved the use of toxic cyanate halogens (Schutyser et al., 2018).

Several studies focused on the use of epoxidised cardanol, a terpene derived from cashew nut shell liquid (CNSL), as a bio-based starting monomer for epoxy resin formulation. It contains both aromatic and aliphatic moieties, which can theoretically result in resins with both toughness and strength. (Jaillet et al., 2014) used commercially available cardanol diepoxy NC-514 to create epoxy formulations with IPDA and Jeffamine 400 hardeners. As in the previous studies, the performance of the cured resins was compared with BADGE formulations. According to the findings of the study, the  $T_g$  of the Cardanol – IPDA network was 50°C, about 3 times higher than the formulation using Jeffamine but more than 3 times lower than the BADGE derivative. The Cardanol – IPDA resin demonstrated thermal stability up to temperatures of around 367°C. A very low char yield of less than 2% was observed at 600°C. The cross-linking density of the cardanol-based epoxy was compared with the BADGE formulation. It was 5 times lower in the case of the IPDA formulation. This was attributed to the long aliphatic chains present in the NC-514 monomer which leads to larger distances between epoxy groups.

Another study investigated the use of cardanol as a raw material for creating bio-based epoxy vitrimers. The goal was to achieve improved degradability, re-processability, welding, and self-healing properties of the resin and subsequently apply it to CFRP composites. First, cardanol was esterified using succinyl chloride and adipoyl chloride. It was then epoxidised to acquire epoxy dicardanol-based succinate (EDCS) and epoxy dicardanol-based adipate (EDCA), both 100% bio-based epoxy monomers. The curing agent used to activate the polymerisation reaction was hexahydro-4-methylphthalic anhydride (HP). The  $T_g$  of EDCS-HP reached around 68°C, higher than EDCA-HP but lower than most other BADGE formulations. It was shown that the tensile strength of the cured epoxy resins strongly depends on the molar ratio of the epoxy to anhydride groups. It was argued that the decrease in tensile strength is related to the cross-linking density and stiffness of the network. Thus, the reduction in tensile strength was due to a lower benzene ring

content of the epoxy monomer. Using TGA, the 5% weight loss of EDCS-HP resin was recorded between 286°C and 317°C. Full thermal decomposition was reached at around 450°C with char yields of less than 2%. The storage modulus of the cardanol-based resin was recorded to be in the range of 1351.2 – 1752.6 MPa (Hu et al., 2023).

Daidzein is another bio-based molecule that can be used for epoxy monomer synthesis. It is a diphenolic compound which is usually obtained from soybeans. In the work of Dai et al., daidzein was used to prepare a flame-retardant diglycidyl ether of daidzein (DGED) epoxy monomer. It was then cured with 4, 4'-diaminodiphenylmethane (DDM) and the properties of the resulting resin were compared with the conventional BADGE variant. According to the investigation, the DGED – DDM resin reached the  $T_g$  of around 205°C, about 30°C higher than BADGE (Ma & Li, 2019).

Another promising bio-based starting material was investigated by Soto et al. Limonene can be obtained as a valuable by-product of citrus processing. This compound possesses two alkene groups, both of which can undergo epoxidation. The limonene dioxide monomer was cured with bio-based glutaric anhydride as a curing agent. This resulted in a resin with a glass transition temperature of 98°C. The obtained  $T_g$  value was lower than the comparable BADGE system, which reached 143°C. Nevertheless, the limonene-based resin showed a competitive storage modulus value of 1.65 GPa, slightly surpassing the 1.6 GPa observed in the DGEBA system (Soto & Koschek, 2018).

Other bio-based starting materials for epoxy resin formulation include itaconic acid (Gonçalves et al., 2021), rosin acid (T. Li et al., 2016), soybean oil (Nepomuceno et al., 2023), Karanja oil (Kadam et al., 2015), magnolol (Bu et al., 2022), linseed oil (Samper et al., 2015), castor oil (Huang et al., 2016), etc.

### 3.5.2. Limitations of Existing Bio-Based Resins

As can be concluded from the overview of the existing bio-based epoxy resins presented in Section 3.5.1, there are a number of drawbacks that may limit their application in such high-performance industries, as aerospace.

Most of the biobased monomers (i.e., plant oils, itaconic acid, isosorbide, cardanol, etc.) have chemical structures containing alicyclic and aliphatic molecular chains. This results in:

- 1) Limited thermal stability (low  $T_g$ );
- 2) Low mechanical properties;
- 3) Low heat resistance and early onset of material degradation.

Furthermore, the hydrophilic nature of bio-based monomers is attributed to the fact that they are derived from natural compounds that contain inherently polar functional groups such as hydroxyl, carboxyl, or ether groups. As a result:

- 4) Bio-based epoxy resins have increased moisture absorption which can have a negative effect on the performance of PMC.

Although some bio-based epoxy resins possess superior thermal and mechanical performance, to achieve it, a complex multi-step synthesis process involving toxic chemicals is required to epoxidise the corresponding monomers (e.g., eugenol, vanillin (Qi et al., 2021)). This results in:

- 5) The high cost of the resin and its health hazards.

Finally, bio-based monomers are often derived from lignin and plant oils (many of which constitute agricultural products). If bio-based monomers are sourced from crops that are also used for food, there could be competition between industrial and food uses. This competition might affect food availability or prices, especially if the demand for bio-based materials increases significantly. As a result:

- 6) Bio-based resin production can undermine food security in certain areas and communities.

A bio-sourced molecule, known as resveratrol, holds the potential to alleviate some of the mentioned issues.

### 3.5.3. Resveratrol

3,5,4'-trihydroxy-trans-stilbene, also known as simply resveratrol, is a naturally occurring polyphenol that can be found in more than 70 different plant species, including berries, buckwheats, legumes (e.g., peanuts), pines, etc.

Even though resveratrol naturally occurs in various plants, its extraction in industrial quantities is hindered by low concentrations, complex extraction procedures with multiple steps of isolation and purification, as well as seasonal dependence (Thapa et al., 2019). Nevertheless, resveratrol has been commercially procured from Japanese knotweed (Jeandet et al., 2014), grape skin and seed (Zwingelstein et al., 2019), as well as the giant knotweed of China. An alternative pathway for resveratrol production is the chemical synthesis. However, the challenge with this production method is the formation of toxic side-products and contaminants, which complicate purification and negatively impact the sustainability of resveratrol (Thapa et al., 2019).

To address these issues, different approaches have been developed to enable the bio-sustainable production of resveratrol. The biotechnological approaches include tissue culture, plant cell suspensions and genetic engineering (Jeandet et al., 2014). More specifically, lignin and biomass sugar fermentation with metabolically engineered microorganisms has advanced to the point that biosynthetic resveratrol is currently commercially available (Halls & Yu, 2008).

Resveratrol is also recognised for its benefits to human health. It acts against pathogens, including bacteria and fungi, as well as possesses high antioxidant potential. On top of that, through multiple studies, resveratrol is shown to have anticarcinogenic properties, making it a potential candidate for cancer prevention and treatment. Furthermore, other bioactive effects, such as cardioprotective (Yan et al., 2018), neuroprotective (Wahab et al., 2017), vasorelaxant (Sato et al., 2002), and anti-inflammatory (Dvorakova & Landa, 2017).

Structurally, resveratrol represents a polyphenolic stilbenoid consisting of two phenol rings which are connected via a carbon-carbon double bond (ethylene). On top of that, it possesses three hydroxyl groups that enable easy chemical modification (Garrison et al., 2020). Furthermore, as a result of its stilbene structure and higher crosslink density, resveratrol is expected to have high thermal stability, heat resistance and mechanical properties (Tian et al., 2021). Furthermore, resveratrol has the potential to increase char yields and reduce flammability. This is attributed to the absence of methoxy groups, which can be found in such lignin-derived phenols as vanillin and eugenol since they can reduce the glass transition and decomposition temperatures (Garrison et al., 2020).

Figure 12 (a) shows the chemical structure of resveratrol, while Figure 12 (b) demonstrates the resveratrol triglycidyl ether (RTE) monomer which is obtained by reacting resveratrol with epichlorohydrin in a NaOH environment, as demonstrated in Figure 6 of Section 3.1. Chemically, the RTE monomer is similar to Tactix 742, having an identical tri-functional nature.

Thus, resveratrol presents itself as a promising candidate for epoxy resin formulation. It has a combination of properties that allows it to alleviate many of the problems of BPA and BPA-derived epoxies. Moreover, resveratrol-based epoxy resins can directly compete with some of the high-performance tri-functional resins, such as Tactix 742. Firstly, it can be naturally obtained from bio-sources or produced industrially using bio-engineered microorganisms. Secondly, it has minimal toxicity and does not present any health hazards to people, unlike BPA.

Although there are several previous studies (Tian et al., 2020) (Liu et al., 2023a) which research the use of resveratrol as a bio-based monomer for epoxy formulation, they mainly focus on the synthesis and characterisation of the epoxy from the standpoint of chemistry and chemical engineering. At the same time, none of the existing investigations explore the applicability of resveratrol resins for high-performance aerospace composite production.

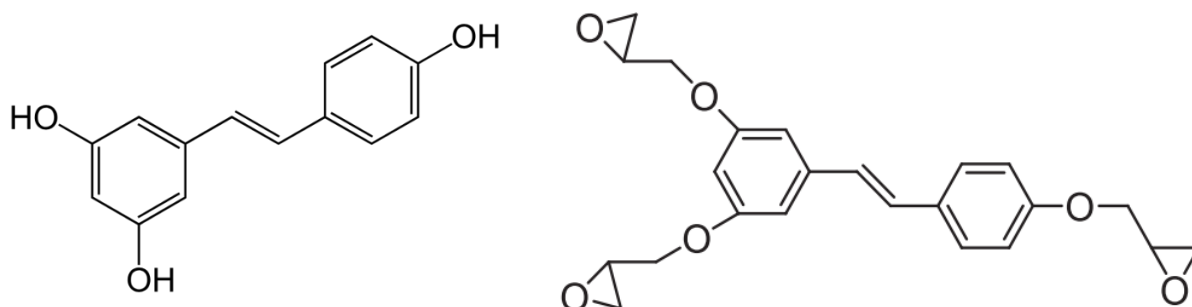


Figure 12. Chemical structure of (a) trans-resveratrol and (b) resveratrol triglycidyl ether (RTE) (Tian et al., 2020)

## 4. Methodology

As can be concluded from the previous chapter, there exists a knowledge gap in the research of resveratrol resins for use in sustainable composite applications. It is the intention of the current investigation to fill in the defined knowledge gap, which leads to the main research goal to be formulated as follows:

*Investigating the potential of sustainable epoxy based on resveratrol triglycidyl ether (RTE) as a high-performance alternative to petroleum-based matrix materials in aerospace composite applications.*

To achieve the outlined goal, the following objectives must be completed:

- Perform an initial literature review of bio-based epoxies, resveratrol-based epoxies, and CFRP composites.
- Identify valuable properties and characteristics of starting monomer and cured epoxy that must be investigated in the context of composite structure applications.
- Perform thermal analysis of resveratrol-based resin and find optimal processing and curing parameters for resveratrol resin.
- Gather data about the physical and mechanical properties of resveratrol-based epoxy resins following available ASTM standards.
- Analyse the properties of RTE-DDS resin and compare them to petroleum-based systems of BADGE and Tactix 742, as well as other bio-based epoxy systems.
- Manufacture CFRP composite laminates using resveratrol-based epoxy as the matrix material.
- Characterise the mechanical performance of the manufactured composites following available ASTM standards and compare them to the BADGE, Tactix 742 and other bio-based epoxy systems.

This thesis is poised to deliver crucial insights into the mechanical performance and thermal behaviour of resveratrol-based epoxy resins from the perspective of their potential use in high-performance composite applications.

Consequently, the research questions that the current study addresses are as follows:

- Does resveratrol-based epoxy alleviate some of the sustainability issues of synthetic epoxy resins?
- Can resveratrol-based resins alleviate some of the problems of existing bio-based epoxies, such as hydrophilicity and poor thermomechanical performance?
- Can the conventional composite manufacturing methods be used to produce resveratrol-based PMCs?
- Do resveratrol-based PMCs possess adequate quality and mechanical performance?

## 5. Resin Characterisation

To get a better understanding of resveratrol-based epoxy resin and conduct a comparison study with the existing commercial and bio-based resins, it was decided to first complete the characterisation of neat resin without the reinforcing phase. The resin characterisation was split into 3 main parts:

- Thermal Property Analysis;
- Physical Property Analysis;
- Mechanical Property Analysis.

Each analysis type involved the use of various characterisation techniques and testing methods, the purpose of which was to gather valuable data related to the processing of uncured resin, the manufacturing of cured specimens, and the thermal and mechanical performance of cured resin. Based on the literature review, it was decided to use DDS as the hardener. Consequently, the optimal mixing ratios of RTE-DDS and T742-DDS were taken as 2.39:1 and 2.69:1, respectively. Appendix A.1 explains the procedure that was used to determine the mixing ratios.

### 5.1. Thermal Property Analysis

The characterisation of the thermal properties of the resin is essential for a better understanding of the curing behaviour. For practical engineering applications, such as composite manufacturing, it is essential to derive a viable cure cycle which maximises the projected properties of the cured resin. The curing cycle is defined by such parameters as the monomer melting point, resin glass transition temperature, gel times, curing onset temperature, degradation temperature, and others. On top of that, the mechanical response of the cured resin to thermal variations is vital for designing high-performance materials expected to operate in harsh environments. Finally, the ease of processing of the resin, which leads to faster manufacturing, can be optimised by knowing how the viscosity of the resin changes with temperature.

The aforementioned parameters were defined using the following characterisation methods, each of which is discussed in the corresponding section:

- Thermogravimetric Analysis (TGA);
- Differential Scanning Calorimetry (DSC);
- Dynamic Mechanical Analysis (DMA);
- Dynamic Rheometry.

#### 5.1.1. Thermogravimetric Analysis

TGA is a material characterisation method in which the mass of a sample is monitored in response to the change in temperature. The material sample is subjected to a controlled temperature program in a controlled environment. Upon heating, the sample's weight changes due to different possible thermochemical processes (PerkinElmer, 2022). Normally, a weight loss can be observed due to

the breaking of chemical bonds (i.e., decomposition) of the material. The weight can also be reduced because of the evaporation of volatiles from the sample. Alternatively, an increase in weight can be seen as a result of oxidation (TA Instruments, 2020b).

The sample is placed on a sample pan which is usually made of high-temperature material (e.g., ceramic). When the pan is located inside the TGA, it is supported by a precision balance inside a furnace. The balance measures the change in mass of the sample during the experiment. The furnace environment is controlled by purge gas which may either be reactive (air) or inert (nitrogen or argon), depending on the experiment type (PerkinElmer, 2022).

The TGA used for performing the experiments was a TGA 4000 produced by PerkinElmer. According to PerkinElmer, the sample size should be between 2 and 50mg. As a result of the limited material available and the sample pan volume, a sample mass of 7.5mg ( $\pm 2.5$ mg) was considered optimal for the experiment. Both RTE-DDS and T742-DDS resins were mixed in appropriate stoichiometric ratios, as defined in Appendix A.1. The sample material for TGA tests was taken from the left-over cured resin used in 3-point bending (See Section 5.3.3).

Following a literature review of other TGA studies of bio-based resins, it was decided to conduct the experiment in the following conditions, to allow result comparability. The temperature was increased from 20°C to 900°C at a heating rate of 10°C /min in the air environment. The gas flow was held at 20ml/min for the duration of the experiment.

Figure 13 displays the mass loss of RTE-DDS and T742-DDS as a function of temperature. At the same time, Table 3 shows the temperatures which correspond to 5%, 15%, and 30% mass loss. On top of that, the heat resistance index temperature ( $T_{HRI}$ ) and the char yield at 900°C are given.  $T_{d5\%}$ ,  $T_{d15\%}$ , and  $T_{d30\%}$  are commonly used indices of performance in thermogravimetric analysis. At the same time,  $T_{HRI}$  has been used by other authors to evaluate the thermal stability of polymers, specifically, epoxies (Lu et al., 2022). The following formula was used to calculate  $T_{HRI}$ :

$$T_{HRI} = 0.49[T_{d5\%} + 0.6(T_{d30\%} - T_{d5\%})] \quad (2)$$

As can be seen from the collected data, both T742 and RTE resins have negligible mass loss before 350°C. Rapid decomposition of RTE-DDS starts progressing sooner than in the case of T742-DDS. This is quantified by  $T_{d5\%}$  which is equal to 364.56°C for RTE and 376.10°C for T742.  $T_{d15\%}$  and  $T_{d30\%}$  are equal to 383.16°C and 403.59°C for RTE, and 388.28°C and 399.48°C for T742, respectively. The data from TGA was used to define a safe temperature region to conduct further experiments with DSC and DMA to avoid rapid combustion of the resin and potential damage to the equipment. It was decided to set the higher temperature limit at 350°C for RTE-DDS resin. At the same time, Figure 14 shows the mass loss with respect to temperature for both resins. A maximum rate of mass loss is observed for both resins in the range of 390°C to 400°C. It can also be observed that, at its peak, the rate of mass loss of T742-DDS is higher than that of RTE-DDS.

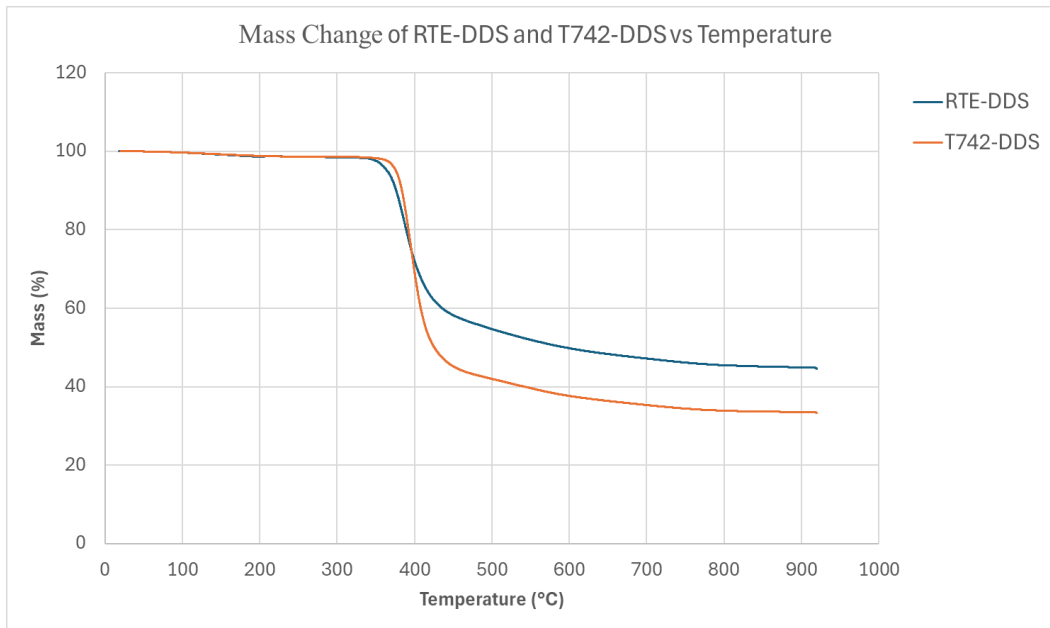


Figure 13. TGA results of RTE and T742 resins in air

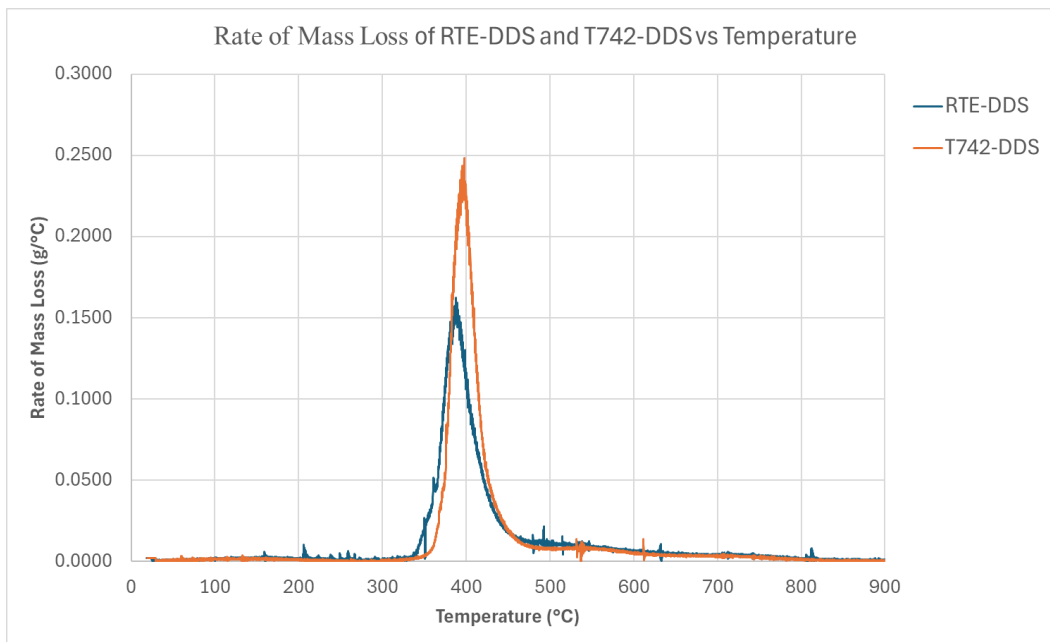


Figure 14. Rate of mass loss with respect to temperature

Sample	$T_{d5\%}$ °C	$T_{d15\%}$ °C	$T_{d30\%}$ °C	$T_{HRI}$ °C	Char Yield @900°C %
RTE-DDS	364.56	383.16	403.59	190.11	44.49
T742-DDS	376.10	388.28	399.48	191.16	33.30

Table 3. Weight loss data of RTE and T742 resins

### 5.1.2. Differential Scanning Calorimetry

Differential Scanning Calorimetry (DSC) measurements were conducted using the DSC 250 produced by TA Instruments. The instrument used in this study belongs to the heat flux type. In a heat flux DSC, the furnace contains a sample pan and a reference pan holder. A sample material is placed into a pan and onto the sample holder inside the furnace (Hitachi, 2022). At the same time, a reference pan (the same pan as the one used for the sample but empty) is placed into the furnace. During a DSC experiment, heat from the heating elements is supplied uniformly to both pans at a controlled heating rate. If a sample undergoes an endothermic (heat-absorbing) or exothermic (heat-releasing) process, the temperature of the sample will change differently than the reference, creating a temperature gradient. The thermocouples register the difference in temperature placed near the reference and sample pans (TA Instruments, 2023). Using the Fourier Law of heat conduction, the temperature difference is converted into the rate of heat flow difference, which is recorded with respect to time or temperature. An increase in heat flow is indicative of an exothermic event, which implies that the sample undergoes a process releasing heat, such as cross-linking or crystallisation. If the sample experiences a thermal event where it begins to absorb more heat (endothermic event), such as melting, then a decrease in heat flow is registered (EAG Laboratories, 2020).

In addition to the conventional DSC process described above, a modulated DSC (mDSC) can be applied to increase the resolution of the measurements. As opposed to the linear heating profile used in conventional DSC, mDSC employs a sinusoidal temperature modulation or oscillation which is overlaid on the standard linear heating profile. As a result, the instrument is able to separate the total heat flow into two components: reversing and non-reversing heat flow. Reversing heat flow can be used to analyse properties that respond to cyclic heating, including glass transition, heat capacity and melting. A non-reversing signal is used to analyse properties that do not respond to temperature modulation, such as crystallisation, decomposition and evaporation (EAG Laboratories, 2020).

Following a literature review of similar studies using DSC to characterise epoxy polymers, it was decided to run a series of experiments including isothermal and non-isothermal measurements. For each measurement, approximately 5-10 mg of material was placed in hermetic pans made of aluminium. The hermetic pans were used to avoid contamination of the DSC furnace due to gas dissipation and to seal the samples from any contamination from the outside.

Initially, a number of non-isothermal DSC experiments were conducted with RTE and DDS mixed at stoichiometric ratios. An amount of uncured resin was sealed in 5 different hermetic pans. Each pan was then subjected to a temperature program from -70 to 320°C at different heating rates (2, 5, 10, 15 and 20 °C/min). Figure 15 shows the plots of heat flow against temperature for 5 non-isothermal runs.

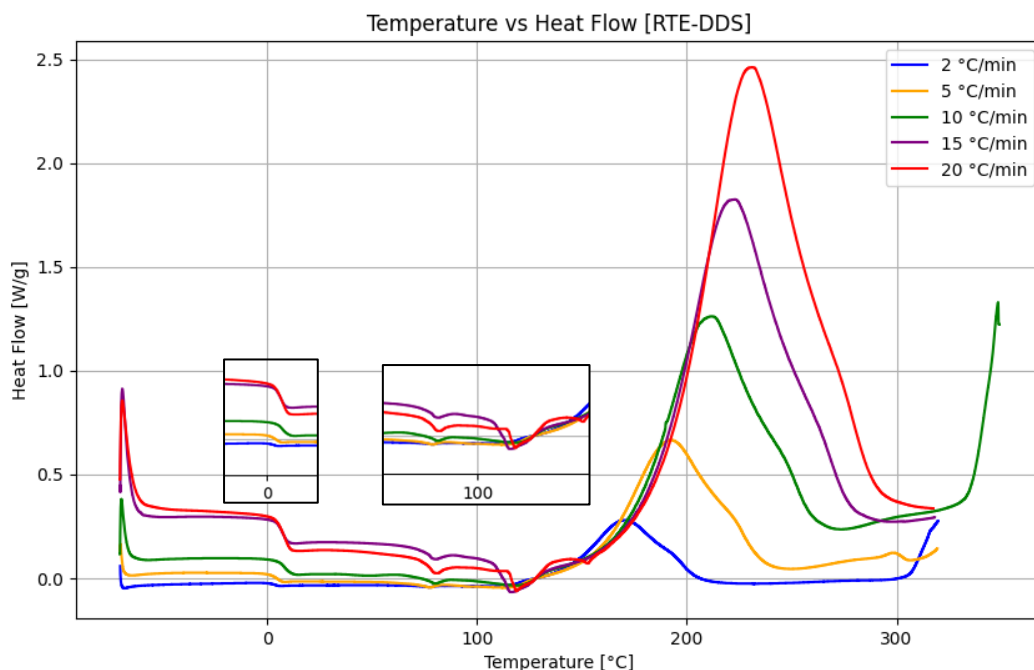


Figure 15. Heat flow vs temperature non-isothermal DSC plot

### Initial Glass Transition and Melting Temperature of the Monomer

The non-isothermal runs with uncured resin had the purpose of initial resin characterisation, including such parameters, as the glass transition temperature of unreacted resin ( $T_g$ ) and melting temperature monomer in the mixture. Both of these properties are important when considering resin storage and future processing.

The glass transition temperature occurs in fully amorphous or within the amorphous phase of semicrystalline materials. It implies the transition of the material from a more rigid state to a rubbery state upon heating. For the RTE monomers in their unreacted state, the molecule mobility is relatively high as a result of the absence of crosslinks, leading to very low initial glass transition temperatures. As a result, the resin behaves like a soft viscous liquid. Once the epoxy starts curing, the  $T_g$  rises, reflecting the increase in stiffness and thermal resistance of the crosslinked polymer network.

Generally, the glass transition temperature shows itself as a step change in the heat flow–temperature curve. Such a step transition can be observed in the initial segment of the curve in Figure 15, right after 0°C. The glass transition temperature can be quantified using one of the available mid-point analysis options, the most common of which is the inflection point. In this case, the  $T_g$  corresponds to the steepest point of the glass transition step. The limits of the glass transition step are defined using the 3 analysis construct lines, 2 of which are tangent to the lower and upper step portions. The third one is tangent to the central step portion and intersects the other two lines at points known as the onset and endset temperatures (TA Instruments, 2020a).

The aforementioned analysis of the data was performed using the TA Instruments Trios Software. Figure 16 contains the initial segments of 2°C/min and 20°C/min heat flow-temperature curves with the 3 construct lines added to the curve. As can be seen from the two plots, the  $T_{g0}$  changes depending on the heating rate. The shift of  $T_{g0}$  in response to changing heating rate is a well-known phenomenon and is attributed to the kinetic nature of glass transition. At faster heating rates, the polymer chains have less time to respond to temperature changes, leading to a higher apparent  $T_{g0}$  (Foreman *et al.*, 2010). As a result, depending on the heating rate (2-20°C/min), the  $T_{g0}$  is between 3.9°C and 8.4°C. At the same time, the melting point of the RTE monomer can be seen in Figure 15. It varies between 75°C and 80°C depending on the heating rate.

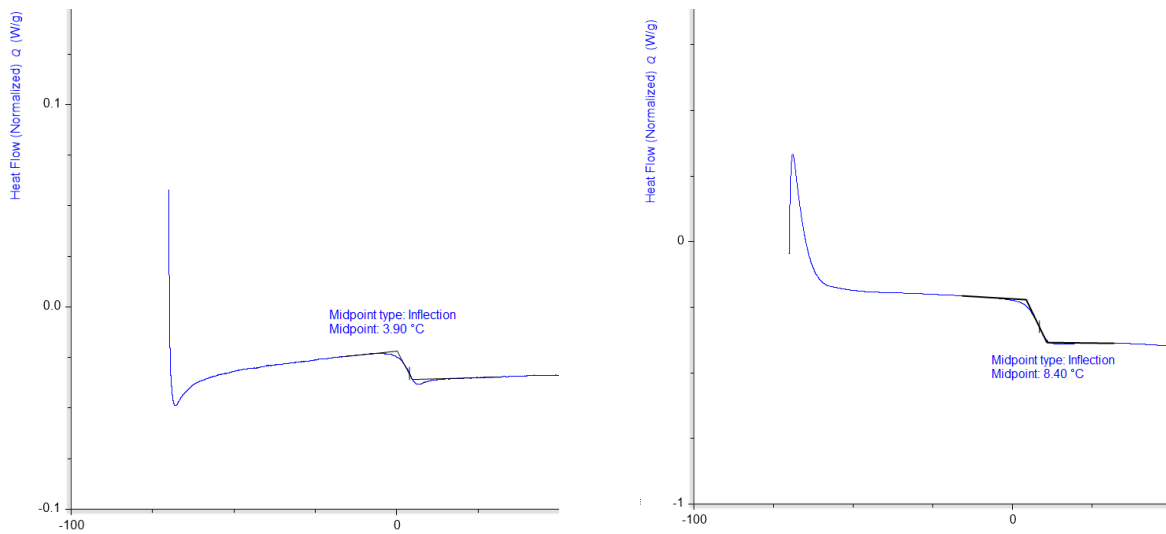


Figure 16. Estimation of  $T_g$  of the uncured resin at different heating rates

### Kissinger's Model Application

Furthermore, the dependence of the peak temperature of the exotherm on the heating rate was examined to determine whether Kissinger's model can be applied to determine the activation energy of RTE-DDS resin and compare it with T742-DDS. Activation energy is an important parameter which indicates how much energy is required to initiate the curing reaction. According to Kissinger, the activation energy of a chemical process can be estimated from data acquired with the help of several non-isothermal tests. Each test must be conducted at a different heating rate. However, the heating rate remains constant within each test (Wellen & Canedo, 2014).

Kissinger's analytical model can be represented with the following equation (Kissinger, 1957):

$$\ln\left(\frac{\beta}{T_p^2}\right) = \ln\left(\frac{AR}{E_a}\right) - \frac{E_a}{RT_p} \quad (3)$$

where  $R$  – universal gas constant ( $8.314 \frac{J}{mol \cdot K}$ ),  $\beta$  – heating rate ( $\frac{K}{min}$ ),  $T_p$  – peak temperature of the exotherm ( $K$ ),  $E_a$  – activation energy of the curing reaction ( $\frac{J}{mol}$ ),  $A$  – pre-exponential factor ( $\frac{1}{s}$ ).

By plotting  $\ln\left(\frac{\beta}{T_p^2}\right)$  versus  $\frac{1}{T_p}$  for 5 available data points and by adopting a linear fit, one can derive the average activation energy from the slope of the fitted line. The slope of the line is then equal to  $\frac{E_a}{R}$ .

Figure 18 shows the results of non-isothermal measurements for RTE-DDS and T742-DDS side by side. The graphs are now limited to the range of interest containing the exothermic peaks. As expected, the magnitude of the exotherm and the peak temperature increase with the heating rate. This is attributed to the fact that the reaction has more time to proceed and the polymerisation is more complete at lower temperatures (Tziamtzi & Chrissafis, 2021). Table 4 contains numerical values of peak temperatures for both resins. At the same time, Figure 17 presents the results of linear fitting to Kissinger's model for RTE-DDS and T742-DDS resins.

Heating Rate	RTE – DDS $T_p$ °C	T742 – DDS $T_p$ °C
2	169.43	170.22
5	191.97	192.20
10	211.42	209.37
15	222.38	218.09
20	231.32	228.37

Table 4. Peak temperature values for RTE and T742 resins

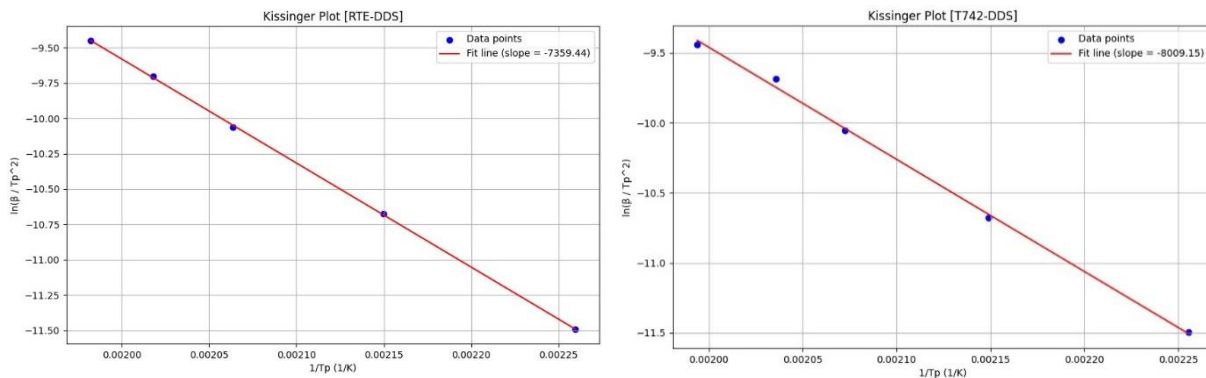
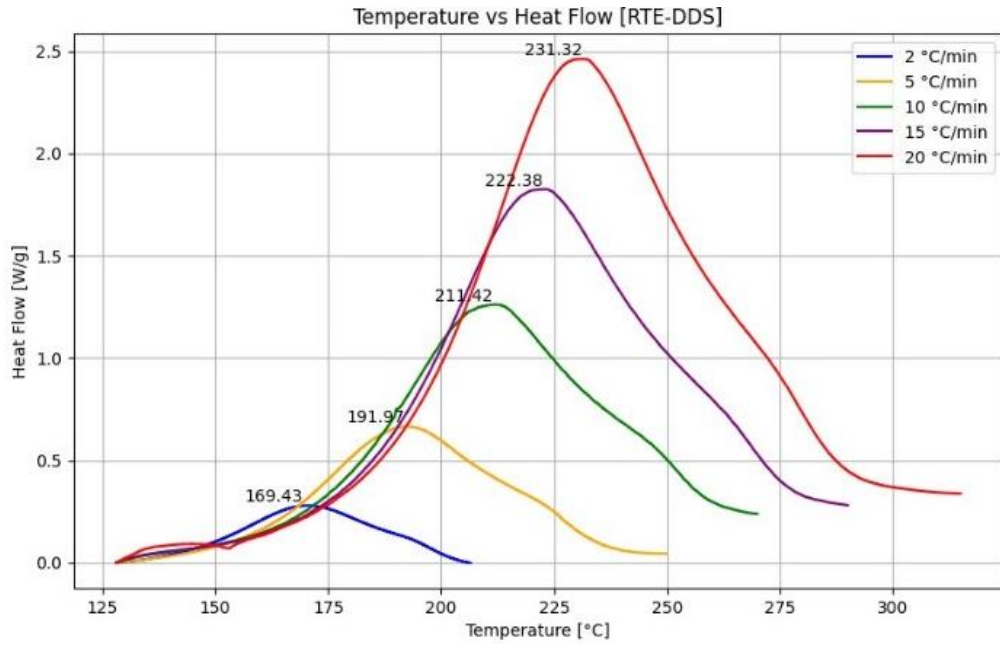
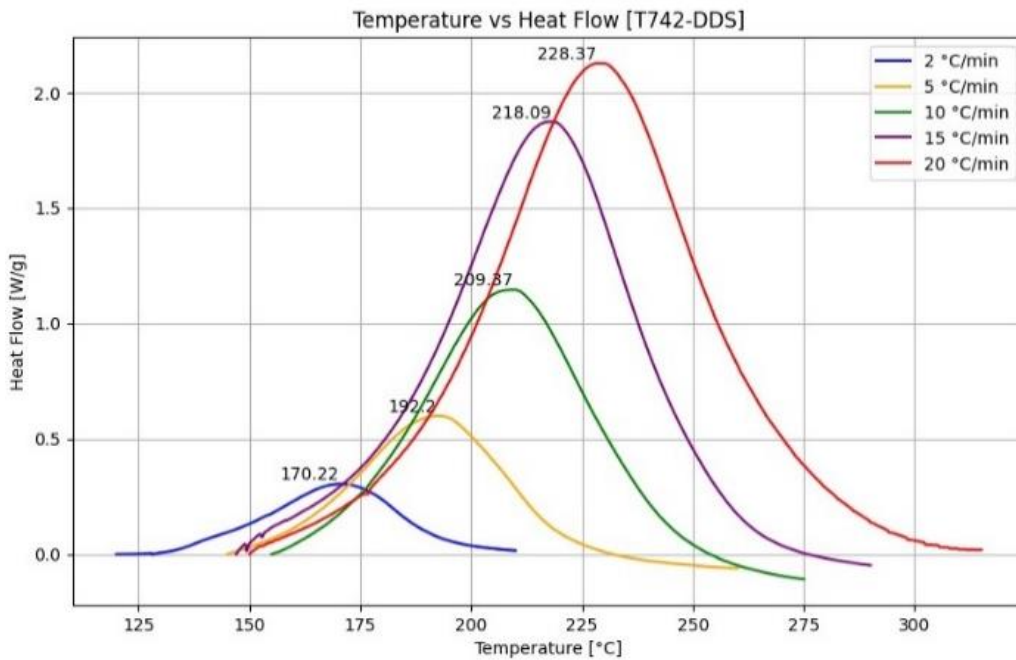


Figure 17. Kissinger model linear fitting plots for RTE and T742 resins

Using the slope of linear fit, the average activation energy was calculated for both resins. It was found that resveratrol-based resin has a lower activation energy of 61.2 kJ/mol, while for T742 resin it stands at 66.6 kJ/mol.



a)



b)

Figure 18. Non-isothermal DSC exotherms for a) RTE and b) T742 resins

## Glass Transition Temperature of Cured Resin

As with determining the  $T_{g0}$  of the uncured resin, it was attempted to characterise the  $T_g$  of the cured resin. At first, the sample which had been cured at the heating rate of 10°C/min was subjected to a second non-isothermal heating run from 10°C to 350°C. As can be seen from Figure 19, the sample was fully cured which can be concluded from the absence of residual heat of enthalpy (an exothermic peak). One can also observe an exothermic event beginning to occur at around 300°C. Although, according to Section 5.1.1, major decomposition begins at around 350°C, a mass loss of around 1.6% can already be observed at 300 °C. Given that organic compounds, such as resveratrol-based epoxy resin, tend to have an exothermic decomposition reaction, it can be assumed that the material starts degrading around that temperature. The exothermic behaviour may result from the release of volatile compounds (e.g., CO<sub>2</sub>) due to a high-temperature oxidation reaction. However, it should be considered that the DSC measurements have been performed in N<sub>2</sub> environment and the influence of oxidation reaction is reduced. Nevertheless, the thermal degradation of the resin (or pyrolysis) still takes place and can be represented by exothermic heat release. Pyrolysis results in the breaking of C-O and C-H bonds, forming free atoms. They are then recombined into H<sub>2</sub>O and CO<sub>2</sub> (Wen et al., 2018). Although the exothermic event beginning at 300 °C could be explained by the onset of degradation, it should be noted that the use of N<sub>2</sub> environment usually delays the onset of degradation, as compared to the air environment of TGA.

In the previous test, no characteristic step-change was observed in the plot which could be associated with the glass transition of the polymer. Thus, it was decided to run a series of additional non-isothermal runs to identify the  $T_g$ . This was done by preparing 1 more sample of larger mass, around 10mg, as recommended by ASTM D3418 standard. According to the standard, the glass transition is more prominent at higher heating rates (ASTM, 2021). Thus, after the sample had been initially cured at 10°C/min from 30 to 300°C, it was subjected to a second heating cycle from 30 to 350°C at the heating rate of 25°C/min. The resulting heat flow diagram can also be observed in Figure 19. A final attempt to determine the  $T_g$  was undertaken using the more sensitive modulated DSC. In mDSC, the  $T_g$  is represented by a characteristic step change in the reversing heat flow measurement. Despite the increased sensitivity of the analysis, the  $T_g$  was not detected in either case.

After a further literature review of similar epoxy systems containing RTE and aromatic amines, it was concluded that a possible explanation for the lack of  $T_g$  is the very high crosslinking density of the resin. In other studies, it led to very high glass transition temperatures in excess of 250°C. Thus, it was assumed that the glass transition region of the RTE-DDS system may overlap with the decomposition region. Hence, it was decided to investigate the  $T_g$  of the system using another characterisation technique – dynamic mechanical analysis (See Section 5.1.3).

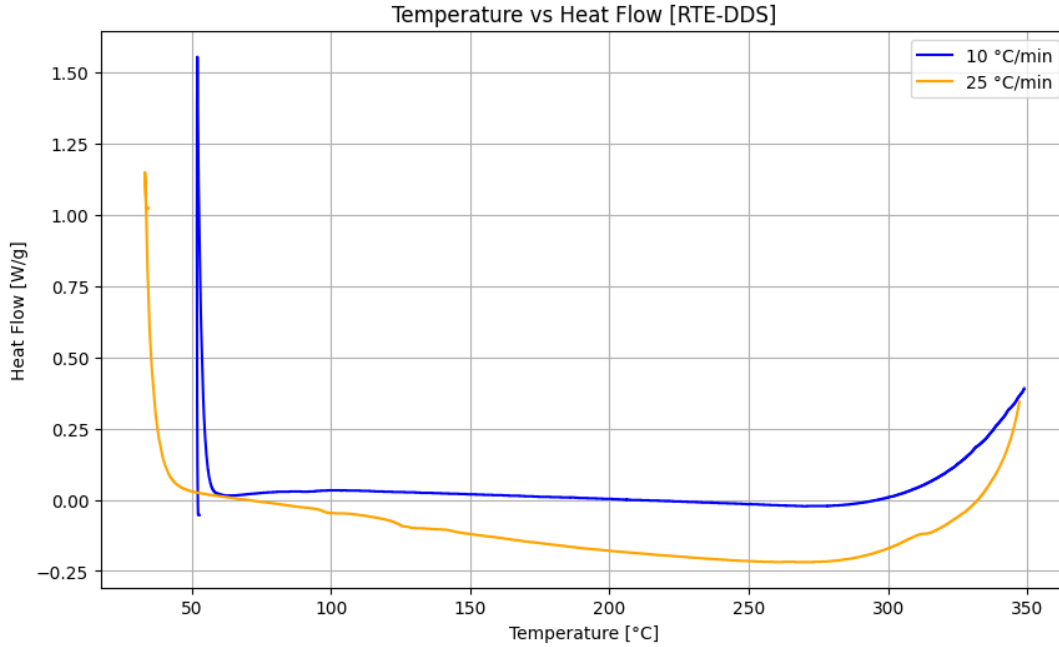


Figure 19. Non-isothermal DSC runs at 10°C/min and 25°C/min

### Isothermal Curing and Kinetic Modelling

In industrial applications, the curing process of PMCs usually takes place in isothermal conditions. In order to explore the curing process of RTE-DDS at different temperatures, another set of DSC experiments was run. The isothermal curing behaviour was studied at 140, 160, 180, 200, and 220°C.

The amount of heat released while curing at a constant temperature for a certain period of time can be calculated as an area under the heat flow – time diagram and is represented using the following formula (Mallick, 2017b):

$$H = \int_0^t \left( \frac{dQ}{dt} \right) dt \quad (4)$$

where  $H$  is the amount of specific heat released during isothermal curing at temperature  $T$  over the time  $t$  and  $\frac{dQ}{dt}$  is the rate of heat generation.

At the same time, the degree of cure is found using the following equation:

$$\alpha = \frac{H_t}{H_R} \quad (5)$$

where  $\alpha$  is the degree of cure,  $H_R$  is the total heat (or enthalpy) of the reaction and  $H_t$  is the enthalpy up to a specific time  $t$ .

Figure 21 presents the evolution of heat flow over time for different isothermal temperatures. It can be noticed that an exothermic peak develops for every experiment. Furthermore, as the temperature increases the exothermic peak becomes higher and less broad. As a result, for higher temperatures, the higher conversion is reached in the same amount of time. It can also be noted that the exothermic peak of each reaction did not appear at the start of the experiment but after a certain amount of time had passed, indicating that the curing reaction can be justified to have the autocatalytic mechanism. This implies that the initial products of the reaction serve as catalysts in the further stages (Mallick, 2017b). From the chemical perspective, it can be explained by the formation of additional hydroxyl groups as a product of epoxy groups and primary amines. Subsequently, these hydroxyl groups can activate additional epoxy groups via hydrogen bonding (Shang et al., 2018a).

The degree of cure is plotted against time in Figure 22 showing that the conversion increases over time. It should be noted that the maximum degree of cure ( $\alpha = 0.91$ ) in this case is below 1, indicating that full cure is not achieved. This is because the total enthalpy of the reaction ( $H_R$ ) was taken from the non-isothermal DSC runs to 300°C. It was found that the average enthalpy of dynamic DSC runs was higher than the enthalpy calculated for each of the isothermal runs. This fact was attributed to the incomplete curing at isothermal conditions as a result of vitrification.

As the curing reaction progresses, the cross-linking of polymer chains takes place, leading to a change in the physical properties of the resin (e.g., molecular weight, viscosity). There are two main points that have to be considered in the context of this physical change: gelation and vitrification. Gelation refers to the conversion of the resin from a liquid to a cross-linked gel or a rubbery state. It can be investigated with dynamic rheometry and is discussed more in Section 5.1.4. At the same time, vitrification happens when the glass transition temperature reaches the curing temperature of the resin. This marks the transition of the resin from a liquid into an ungelled glass (if gelation has not occurred) or from a gelled rubber into a gelled glass (if gelation has occurred) (Davé & Loos, 2000a). These two transitions are characterised as a function of temperature and time using the Time-temperature-transformation (TTT) diagram, an example of which is given in Figure 20.

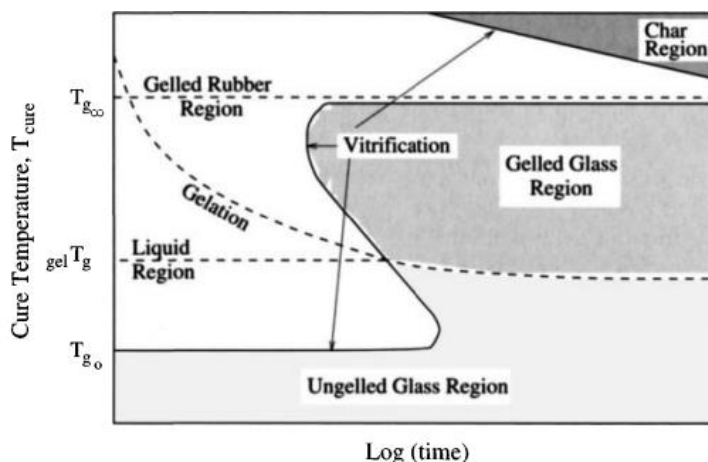


Figure 20. Example of TTT diagram

For an isothermal curing process, if the curing temperature is below the ultimate glass transition temperature of the resin ( $T_{g\infty}$ ), then the system will vitrify. As a result, the polymer chains will experience restricted mobility or may even become immobile (Tziamtzi & Chrissafis, 2021), significantly slowing down the curing rate. At this point, the curing process may no longer be governed by kinetic but by diffusion. A fully cured resin is achievable only when the curing temperature is above the ultimate glass transition temperature, allowing sufficient molecule movement for the reaction to proceed (Davé & Loos, 2000a). The indications of vitrification were later observed in Section 5.1.3 using DMA analysis.

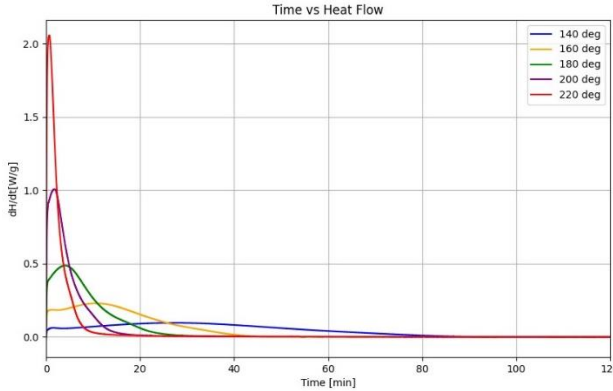


Figure 21. Isothermal DSC heat flow vs time

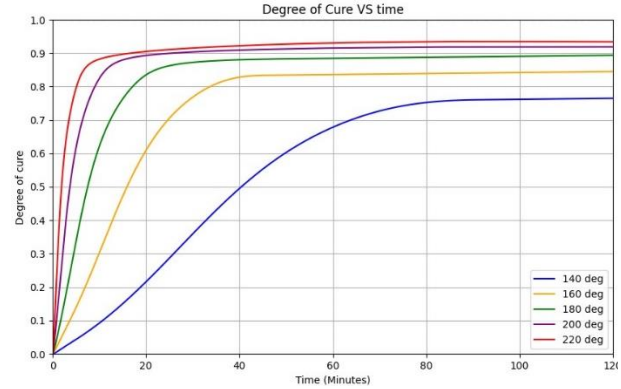


Figure 22. Isothermal DSC conversion vs time

It was then decided to model the curing behaviour of the resin using the Kamal – Sourour model. The authors of the model proposed the following empirical equation for the isothermal cure rate of a thermosetting resin:

$$\frac{d\alpha}{dt} = (k_1 + k_2\alpha^m)(1 - \alpha)^n \quad (6)$$

where  $m$  and  $n$  are constants describing the order of the reaction, while  $k_1$  and  $k_2$  are reaction rate constants. The values of these constants are determined by the non-linear least-squares curve fitting to the experimental data.

The reaction rate constants are defined according to the Arrhenius equation:

$$k_1 = A_1 \exp\left(-\frac{E_1}{RT}\right) \quad (7)$$

$$k_2 = A_2 \exp\left(-\frac{E_2}{RT}\right) \quad (8)$$

where  $A_1$  and  $A_2$  are constants,  $R$  is the universal gas constant,  $T$  is the curing temperature, and  $E_1$  and  $E_2$  are the activation energies.

Figure 23 shows the experimentally acquired degree of cure and rate of cure data and the corresponding approximation of the curing behaviour with the Kamal-Sourour model. It was decided to analyse the accuracy of the model fitting by calculating the Mean Squared Error (MSE) and Root Mean Squared Error (RMSE). These two metrics were chosen to assess the accuracy since the Kamal-Sourour model uses least squares regression to minimise the sum of squared differences between the predicted and actual values (i.e., residuals). At the same time, MSE calculates the average of the squared residuals, which aligns directly with how least squares regression fits the model. It is mathematically consistent with the method used to fit the regression line. RMSE is often used alongside MSE. Mathematically, it is the square root of MSE, representing the data in the original units. Thus, MSE and RMSE were calculated for each dataset. Their averages alongside the Kamal-Sourour model parameters can be seen in Table 5. The closer the value of error is to 0, the higher the accuracy of the model is. As can be seen from the table, the value of MSE is very low, indicating a high level of accuracy.

It should be noted however that the accuracy of the model can be influenced by various factors including experimental uncertainties in the measured data and the inability of phenomenological models to fully capture the complex behaviour of epoxy resin curing (Hardis et al., 2013). On top of that, the presence of vitrification in the system can change the behaviour of the system introducing diffusion processes at the later stages of curing (Mallick, 2017b). In order to account for diffusion effects due to vitrification, other more complex curing models should be investigated. One of such models is proposed by Chern and Poehlein (Davé & Loos, 2000b). Alternatively, a modified Kamal-Sourour model with the Rabinowitch diffusion-control modification. It assumes that the reaction becomes diffusion-controlled as the glass transition temperature approaches the current curing temperature. To define the change in glass transition temperature, the DiBenedetto equation can be used (Javdanitehran et al., 2016).

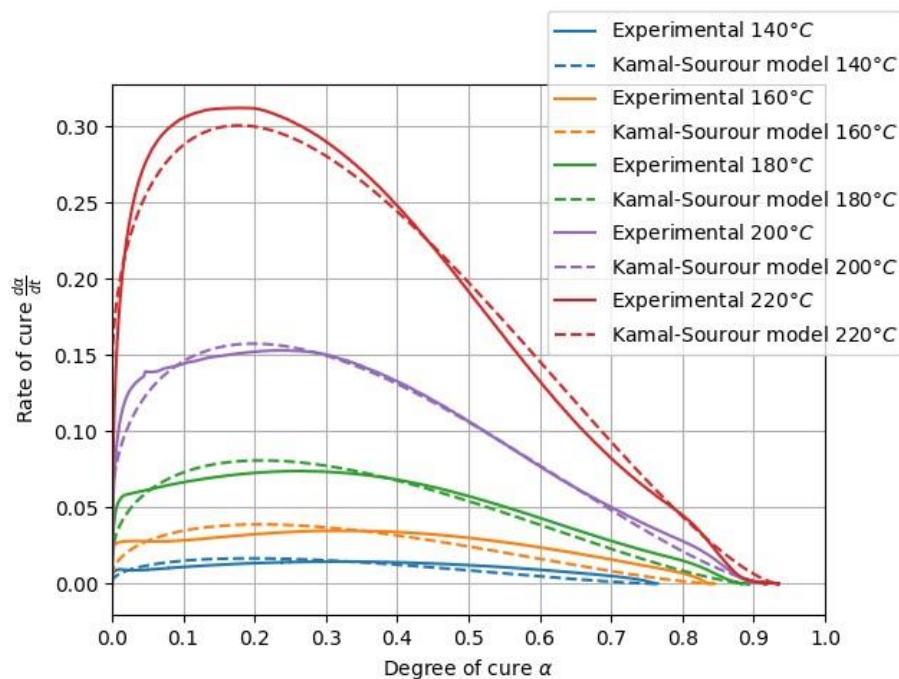


Figure 23. Rate of cure vs conversion and the overlaid Kamal-Sourour model

Parameter	$A1$	$A2$	$E1$	$E2$	$m$	$n$	MSE	RMSE
	-	-	kJ/mol	kJ/mol	-	-	-	1/K
RTE-DDS	280231 628	5207	51.660	35.518	0.506	1.434	8.271 * $10^{-6}$	0.0026

Table 5. Kamal-Sourour model parameters

### Implications for the Curing Cycle

The data from isothermal and non-isothermal DSC runs was used to define the curing cycle used for manufacturing samples for further experimentation. From the isothermal data on conversion, it can be seen that only curing at 180°C, 200°C and 220°C led to a conversion higher than 0.85 in a reasonable amount of time (120 min). Ultimately, a decision was made to proceed with a curing cycle of 2 hours at 180°C. The decision was based on several considerations. First of all, the conversion of  $\alpha \approx 0.9$  was achieved at this temperature in a limited amount of time. Secondly, the curing temperature of 180°C matches the melting temperature of DDS (179°C), which is desirable for achieving a more homogeneous mixture. At the same time, curing at a higher temperatures (200°C or 220°C) can potentially lead to residual stresses forming in the resin as a result of high thermal gradients. In turn, this can lead to geometric distortions of the cured composite panel, as was found in another study (Alleman, 2018). As a way to avoid this, it is common practice in industry to utilise a 2-step curing cycle with the primary curing reaction taking place at a lower temperature, followed by post-curing at a higher temperature. This way, most of the curing reaction will take place at lower temperatures giving the structure its final rigid shape. The remaining cross-linking can then be completed at a higher temperature without any geometric distortions.

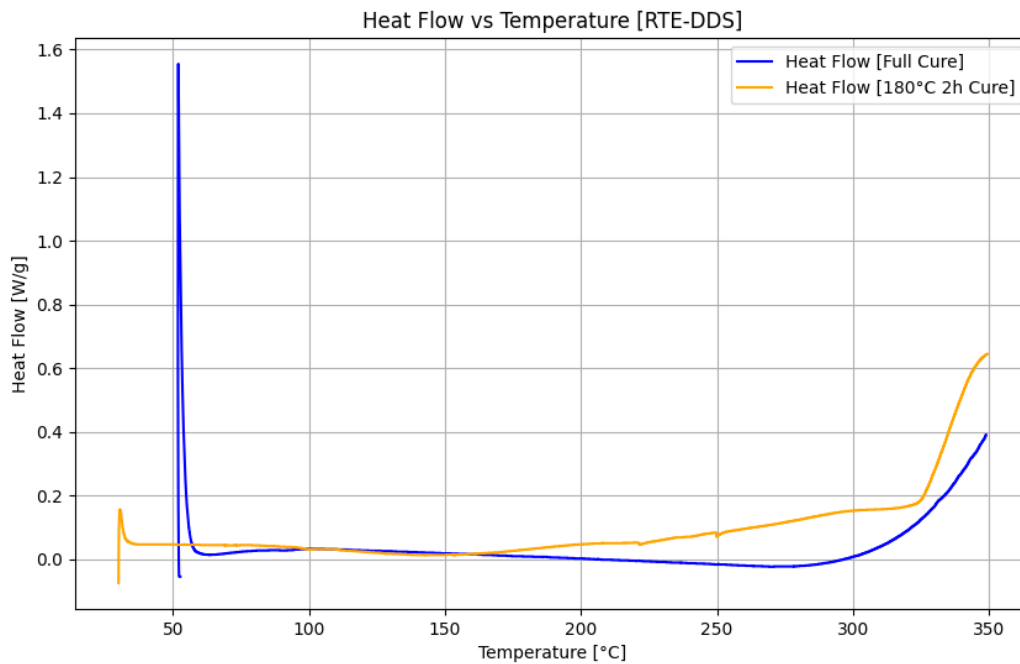


Figure 24. Non-isothermal DSC run on a sample cured at 180°C for 2 hours

Finally, the need for post-curing can be observed from Figure 24 showing a heat flow diagram of a non-isothermal DSC completed on a sample cured at 180°C for 2 hours compared to a fully cured sample. As can be seen, an increase in heat flow around 180°C indicates re-initiation of curing. This behaviour is attributed to the de-vitrification of the system. The application of a post-curing cycle is explored in more detail in Section 5.1.3.

### 5.1.3. Dynamic Mechanical Analysis

Dynamic Mechanical Analysis (DMA) is a technique in which a small cyclic deformation is applied to a sample, allowing the material's response to stress, temperature, frequency, and other variables to be studied. DMA operates by applying a sinusoidal deformation to a sample with a known geometry, where the sample can experience either controlled stress or controlled strain. When stress is applied, the sample deforms, and the amount of deformation is related to the material's stiffness (Singh & Singh, 2022).

DMA measures two key properties: stiffness and damping, which are reported as the modulus and  $\tan(\delta)$ , respectively. Since the force applied is sinusoidal, the modulus can be broken down into two components: the storage modulus ( $E'$ ), representing the in-phase or elastic behaviour of the sample, and the loss modulus ( $E''$ ), representing the out-of-phase or viscous behaviour. The aforementioned  $\tan(\delta)$  represents the ratio of the loss modulus to the storage modulus. This ratio provides a measure of the material's ability to dissipate energy.

Generally, DMA is considered to be a more sensitive  $T_g$  measurement technique than DSC. This is attributed to the fact that the dynamic modulus and damping experience more noticeable changes when a polymer sample undergoes a thermal transition. As such, a significant change in mechanical properties can be observed when the structure of a sample goes through a glass transition.

The acquisition of the aforementioned dynamic properties (i.e.,  $E''$ ,  $E'$  and  $\tan(\delta)$ ) opens up three possible ways of determining the  $T_g$  of a polymer: the peak of  $E''$ , the peak of  $\tan(\delta)$  and the drop of  $E'$ . The drop of storage modulus usually gives the most conservative assessment of  $T_g$ . This method is based on calculating the intercept of two tangents – to the glassy plateau and the rapid drop in the transition region of the storage modulus. The  $T_g$  measurement from the peak of loss modulus and damping provide less conservative results than from the storage modulus intercepts. The  $T_g$  is simply taken as the temperature which corresponds to the highest value of either  $E''$  or  $\tan(\delta)$  (TA Instruments, 2015).

### Test Setup and Sample Characteristics

The main purpose of the DMA experiments was the determination of the glass transition temperature of polymer samples cured with a specific cycle. The tests were set up based on the literature review and the ASTM D5023 standard for determining the dynamic mechanical properties of plastics in flexure. Thus, a three-point bending fixture was used to analyse the samples. To determine the  $T_g$  of cured RTE-DDS resin, the samples were subjected to a temperature sweep from 30 to 350°C, limited by the onset of rapid decomposition. The temperature

was increased at a constant specified rate, while a force was applied to the sample at a frequency of 1 Hz and a displacement amplitude of  $7.5\mu\text{m}$ . Various heating rates (3, 5, 10,  $20^\circ\text{C}/\text{min}$ ) were used to see the influence of the parameter on the  $T_g$ . The DMA samples were prepared using an available mould and sized following the ASTM D5023 standard. After curing, each sample was cut with the following dimensions:  $35\times 9\times 2\text{mm}$ . A support with a 25mm span was used, allowing a 5mm overhang on each edge. Finally, a normal force of 0.1 N was used to continuously maintain contact with the specimen and the fixture

### Initial DMA Tests (No Post-Curing)

Initially, 3 DMA runs were performed on the samples that had been cured at  $180^\circ\text{C}$  for 2 hours. Each experiment was performed at a different heating rate (5, 10,  $20^\circ\text{C}/\text{min}$ ). This was done to see how the heating rate influences the detected  $T_g$  of the resin. For the purpose of the experiment, it was decided to define the  $T_g$  using the peak of  $\tan(\delta)$ . Figure 25 shows the evolution of  $\tan(\delta)$  with temperature.

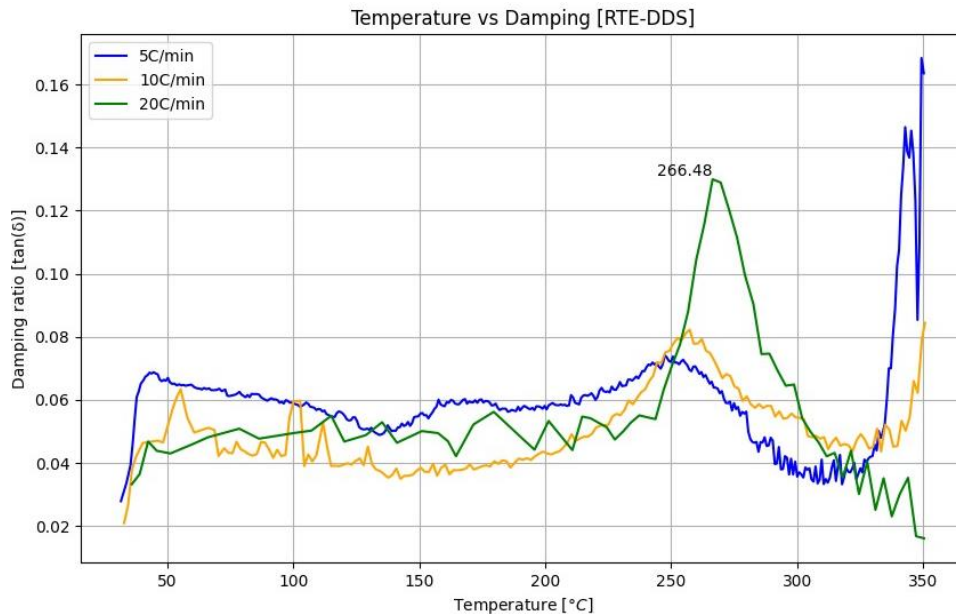


Figure 25. Damping vs temperature for various heating rates (no post-curing)

From the presented data, it was concluded that curing occurred during the experiment. It is assumed that due to vitrification, the resin had not fully cured during the previously defined curing cycle. As a result, an intermediary peak in  $\tan(\delta)$  can be observed for each heating rate in the range of  $250^\circ\text{C}$  to  $270^\circ\text{C}$  which indicates the de-vitrification of the sample. This peak becomes more pronounced at  $20^\circ\text{C}/\text{min}$  which is attributed to the fact that at a higher heating rate, the resin has less time to cure. Therefore, a more significant and instantaneous change in material response can be observed. At the same time, the peak is less pronounced for  $5^\circ\text{C}/\text{min}$  and  $10^\circ\text{C}/\text{min}$  since the transition region is wider and the material response changes more gradually over time. Finally, a rightward shift in the intermediary peak is observed as the heating rate increases. This is expected

since a higher heating rate shifts the measured  $T_g$  to a higher temperature due to the kinetic nature of the glass transition and thermal lag in the sample.

After the intermediary peak, the  $\tan(\delta)$  eventually reaches the final peak at around  $340^\circ\text{C}$ . Due to the shift in  $\tan(\delta)$ , the final peak is not observable for  $20^\circ\text{C}/\text{min}$  heating rate. As a result of these experiments, it can be concluded that the  $T_{g\infty}$  of the RTE-DDS is in the excess of  $300^\circ\text{C}$  and overlaps with the decomposition region that was defined in Section 5.1.1. Using the peak of  $\tan(\delta)$ , the  $T_{g\infty}$  can be estimated at around  $340^\circ\text{C}$ . However, the  $T_g$  of the resin after the isothermal curing cycle at  $180^\circ\text{C}$  for 2 hours is assumed to be closer to  $260^\circ\text{C}$ . In fact, it is assumed to be somewhere between  $200^\circ\text{C}$  and  $260^\circ\text{C}$  since high heating rates lead to the rightward shift in the peak of  $\tan(\delta)$ .

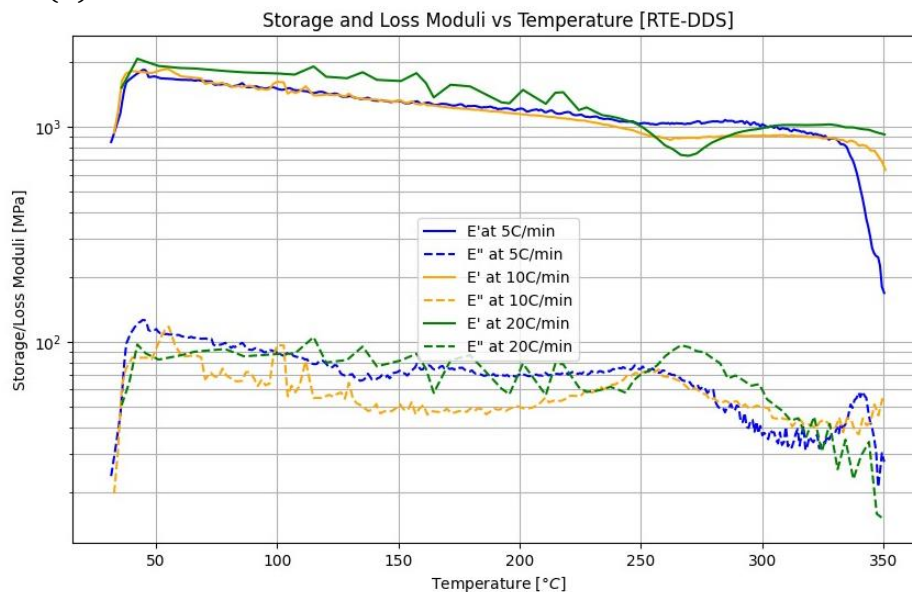


Figure 26. Storage and loss moduli for various heating rates (no post-curing)

This argumentation is also represented by the changes in storage and loss moduli, as seen in Figure 26. A minor decrease in storage modulus is seen around  $260^\circ\text{C}$  which corresponds to a standard behaviour of a resin entering the glass transition region where the molecular motion increases and the polymer chains start sliding against each other. This behaviour is accompanied by an initial increase in loss modulus due to increased heat dissipation resulting from friction during segmental motion. This is followed by a decrease in loss modulus when the friction forces are reduced as the molecules become less entangled and some chemical bonds start to break down, thus, reducing the heat dissipation. One can also observe clearly that at  $20^\circ\text{C}/\text{min}$  the storage modulus quickly recovers to a higher value shortly after the initial drop. This can be explained by the de-vitrification of the system and continued cross-linking.

### DMA Tests (With Post-Curing)

Additional DMA measurements were performed on the samples that had been post-cured at  $220^\circ\text{C}$ . Once again, the samples were tested at different heating rates, 3 and  $10^\circ\text{C}/\text{min}$ . The tests were run until  $350^\circ\text{C}$ . As can be seen from Figure 27, an initial  $\tan(\delta)$  peak appears at around  $260^\circ\text{C}$  for

3°C/min and at 280°C for 10°C/min, indicating some curing takes place. Additionally, for 3°C/min, a clear peak can be observed around 341°C. As can be seen in Figure 28, no significant decrease in storage moduli can be observed. However, a small increase in loss moduli can be seen for both heating rates.

Concerning the storage modulus, it should be noted that the maximum value was recorded for a 3°C/min heating rate at room temperature and was approximately 2427.8 MPa. The impressive performance of RTE-DDS at high temperatures can be seen from the fact that at 300°C, the storage modulus is still 1229.5 MPa.

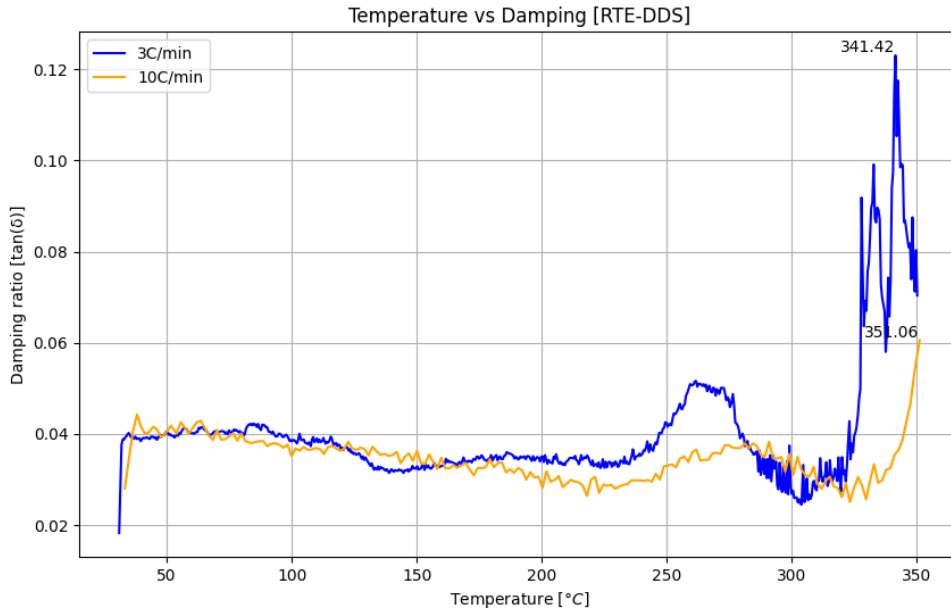


Figure 27. Damping vs temperature at various heating rates for RTE-DDS (with post-curing)

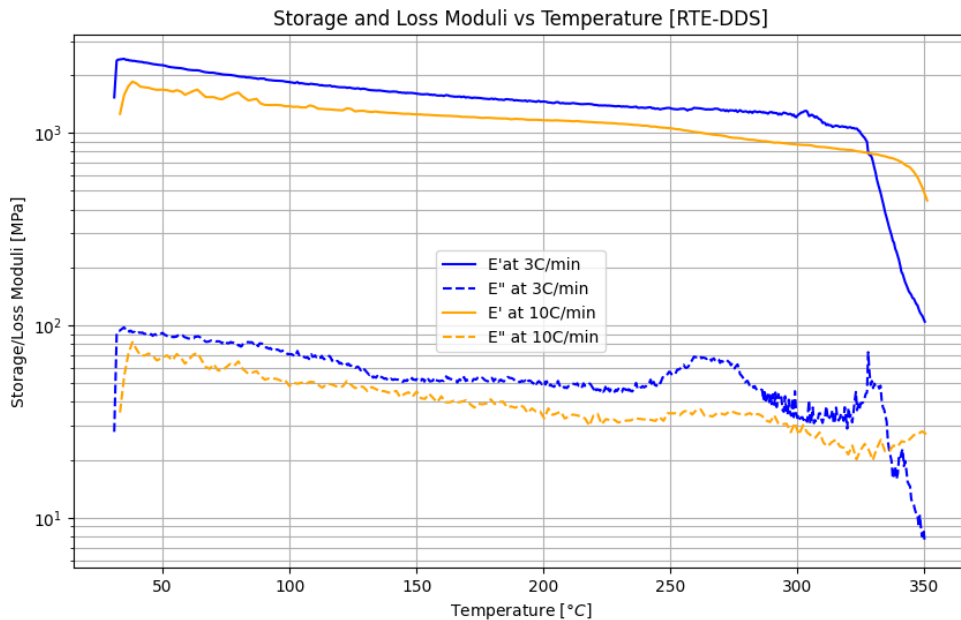


Figure 28. Storage and loss moduli at various heating rates for RTE-DDS (with post-curing)

It was attempted to define the  $T_g$  of T742-DDS resin cured at 180°C for 2 hours and 220°C for 1 hour. As can be seen from Figure 29, a peak in  $\tan(\delta)$  is seen around 237°C and 247°C for 3°C/min and 10°C/min heating rates, respectively. This behaviour indicates that akin to RTE-DDS, some residual curing takes place during the DMA runs. Furthermore, a peak around 343°C is seen for 3°C/min, which corresponds to a significant drop in modulus in Figure 30. Finally, from the 3°C/min measurement, the storage modulus of T742-DDS at room temperature is around 2216.6 MPa, while at 300°C it is 1091.8 MPa.

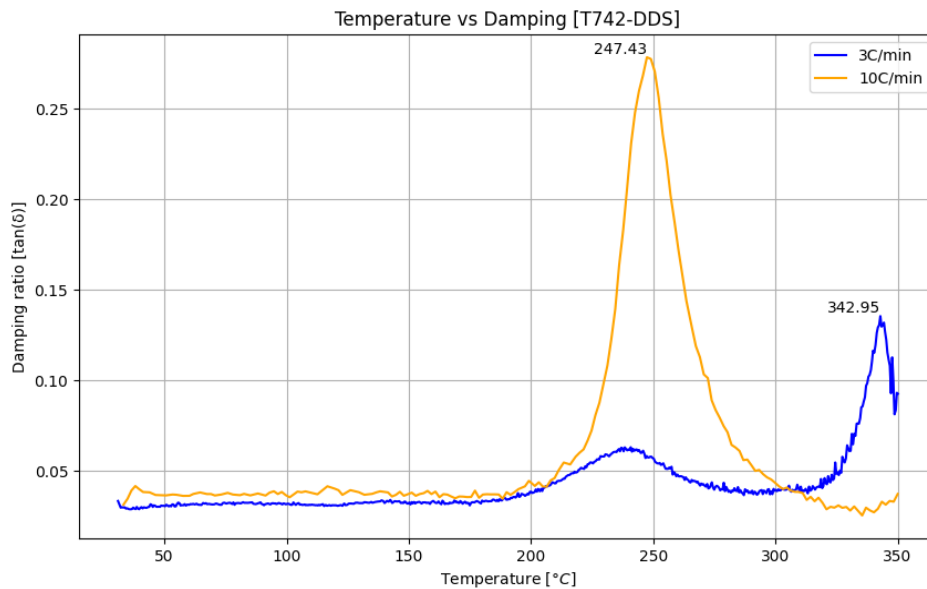


Figure 29. Damping vs temperature at various heating rates for T742-DDS (with post-curing)

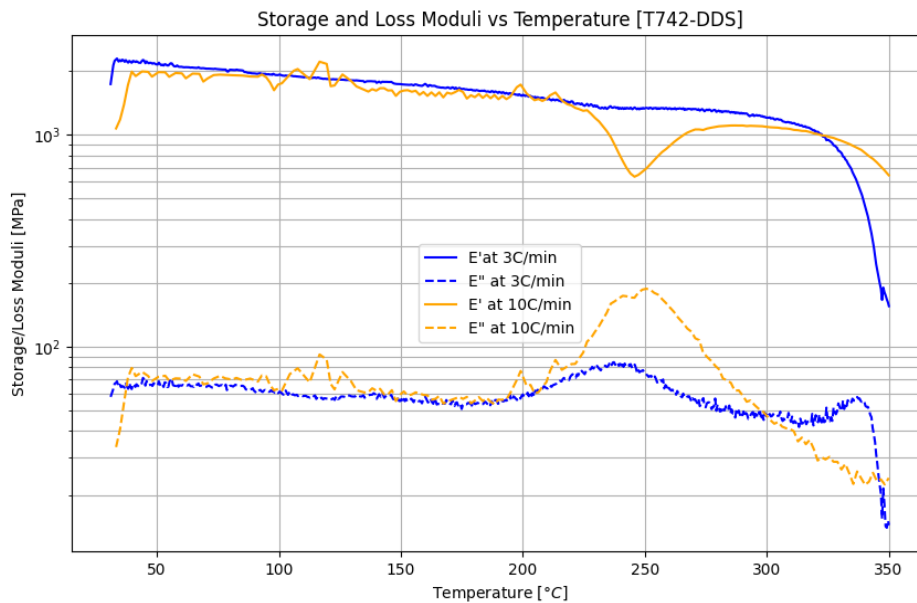


Figure 30. Storage and loss moduli at various heating rates for T742-DDS (with post-curing)

In conclusion, DMA does not provide a reliable means of accurately estimating the  $T_g$  of the resin cured with the chosen cycle. For both resins, residual curing was observed in the range from 230°C to 280°C characterised by a drop in storage modulus and an increase in loss modulus. However, the moduli recovered to the initial values shortly after. A significant drop in storage moduli of both resins happened at around 320°C. However, it is most likely attributed to the effects of material degradation due to decomposition which starts around 300°C. If it is assumed that the storage modulus drops as a result of both material degradation and glass transition, then  $T_{g\infty}$  of both resins can be estimated at around 340°C using the  $\tan(\delta)$  peak method.

#### 5.1.4. Dynamic Rheometry

Dynamic rheometry, or rheology, is the scientific study of how materials flow and deform. In this field, "deformation" and "flow" are characterised by strain and strain rate, respectively. They represent the extent to which a material displaces under an external force, known as stress. By evaluating strain, strain rate, and stress, we can understand the material's viscosity as it changes with temperature and time (Anton Paar, 2017).

In this study, it was deemed necessary to assess the viscosity and gel time of RTE-DDS resin to optimise the processing and manufacturing procedure of neat resin samples and carbon fibre-reinforced composites. Due to the overall similarities between RTE and Tactix 724 resins, the conclusions made for RTE resin were also applied to T742 resin. Rheological tests were conducted using a HAAKE MARS III rheometer. Given that resin viscosity is typically high at room temperature, it was necessary to assess how viscosity responds to temperature changes to establish an effective processing procedure. Samples with flat, 20 mm diameter disposable aluminium plates (pp20) were prepared and attached to the rheometer. The distance between two aluminium plates was set to 1mm. In total, 2 types of experiments were conducted with the rheometer.

One experiment used the Constant Rotation (CR) mode with a rotational frequency of 10 Hz, examining temperature-induced viscosity variations from 40°C to 140°C, at a heating rate of 10 °C/min. This setup was used to observe how the complex viscosity of the resin evolves across a range of temperatures. Additionally, a second type of experiment was performed to measure the change in shear storage and loss moduli at different temperatures and correlate it with the start of the gelation of the resin. The measurements were performed at 100°C and 180°C.

Figure 31 present the plots showcasing the change in viscosity of RTE-DDS and T742-DDS resins with respect to temperature, while Table 6 gives the viscosity values at specific points in the temperature range for both resins. As can be seen from the viscosity data, both resins possess very high viscosity values until around 40°C. However, the viscosity of T742-DDS is considerably higher than that of resveratrol-based resin. As the temperature increases, a major drop in viscosity can be observed already at 60°C. However, a general trend can be seen where T742-based resin has higher viscosity over the entire temperature range.

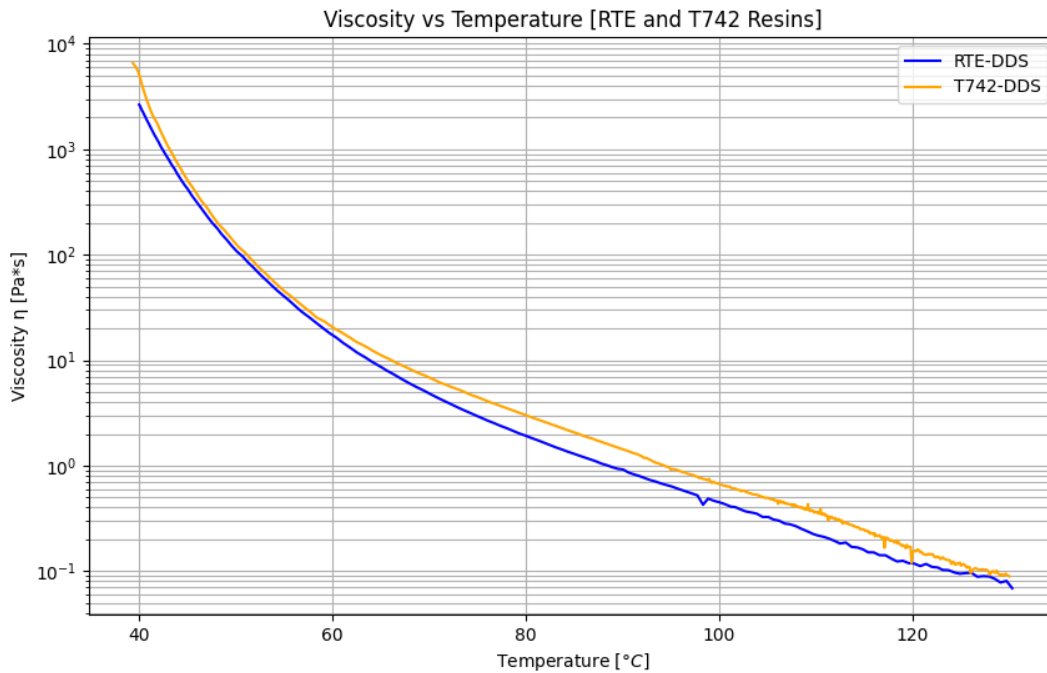


Figure 31. Change in viscosity of RTE-DDS and T742-DDS with temperature

Temperature °C	<i>RTE – DDS</i>	<i>T742 – DDS</i>
	$\eta$ Pa*s	$\eta$ Pa*s
40	2653	5441
60	18.19	21.44
80	1.92	2.98
100	0.45	0.68
120	0.12	0.15
140	0.06	0.08

Table 6. Viscosity values at specific temperatures of RTE- and T742-based resins

The gelation time also plays an important role in selecting and optimising the manufacturing process. When pre-heating the resin for processing, such as an application on a dry fabric during wet lay-up, it is important to avoid premature gelling which can prevent uniform spreading of the resin and fibre wetting. It can be seen from Figure 32 that when kept at 100°C RTE-DDS resin undergoes an increase in storage modulus at around 200min. Eventually, the storage modulus plot intersects the loss modulus curve at around 300min, which can be associated with the initial stages of curing when the cross-linking reaction progresses to the point where the epoxy transitions from a viscous liquid to a gel-like consistency (TA Instruments, 2012). Thus, the resin can be kept at 100°C for over 4.5 hours until the gelation occurs. This gives a sufficient amount of time for resin pre-heating, processing and impregnation. Furthermore, a similar set of data was obtained for

180°C, as can be seen in Figure 33. It can be concluded that at this temperature the cross-linking reaction progresses very rapidly, reaching a gel state in about 5 minutes. This corresponds with the isothermal DSC data which showed an exothermic peak around 5-7 minutes at the same temperature.

Based on the viscosity and gelation data for RTE-DDS resin, it was decided to select 100°C as the processing temperature during resin preparation (i.e., mixing, degassing). At this temperature, the viscosity is low enough to enable convenient work with the resin for a sufficient amount of time without gelation. At the same time, given the high rate of reaction at 180°C and early gelation, it was decided to modify the curing cycle with another dwell step at 120°C for 30 minutes. This is to enable uniform resin distribution in a mould or across layers of composite fabric, good fibre wetting and evacuation of trapped volatiles from the resin to reduce void content.

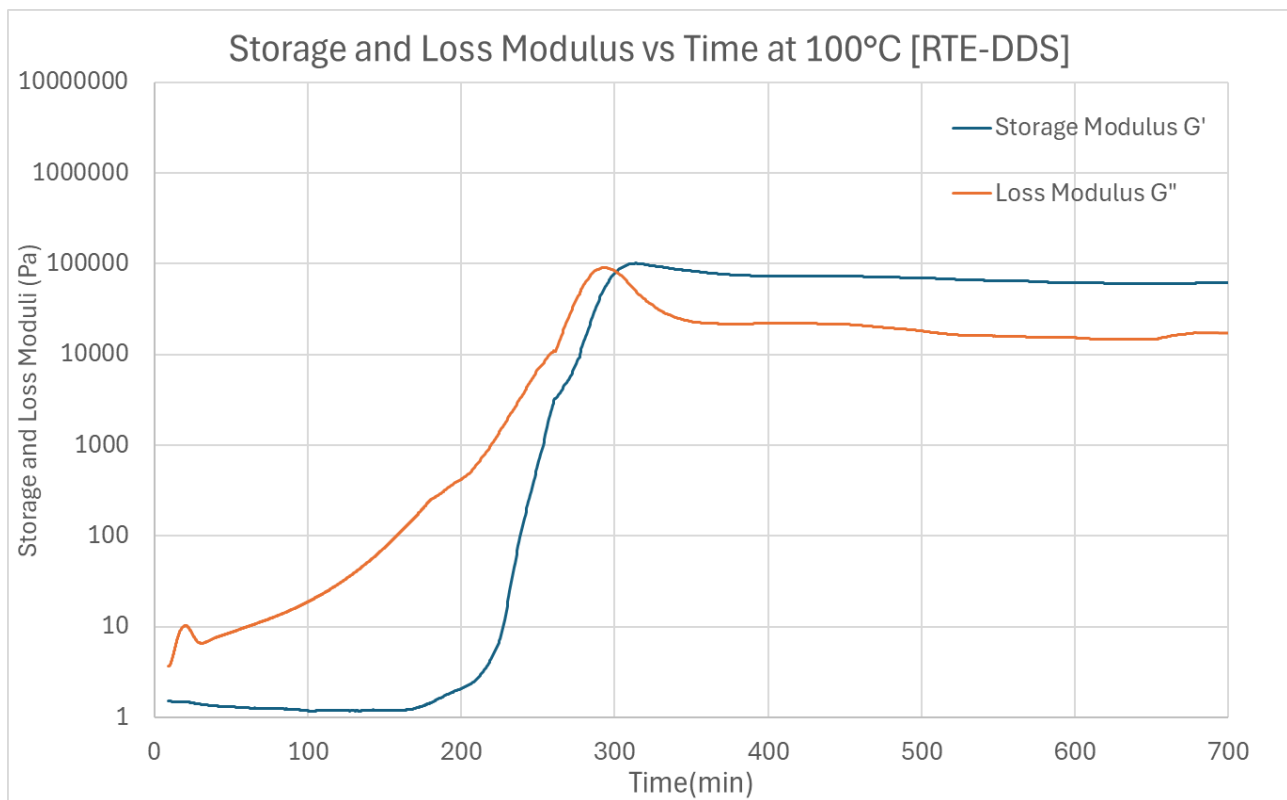


Figure 32. Change in storage and loss moduli with time at 100°C

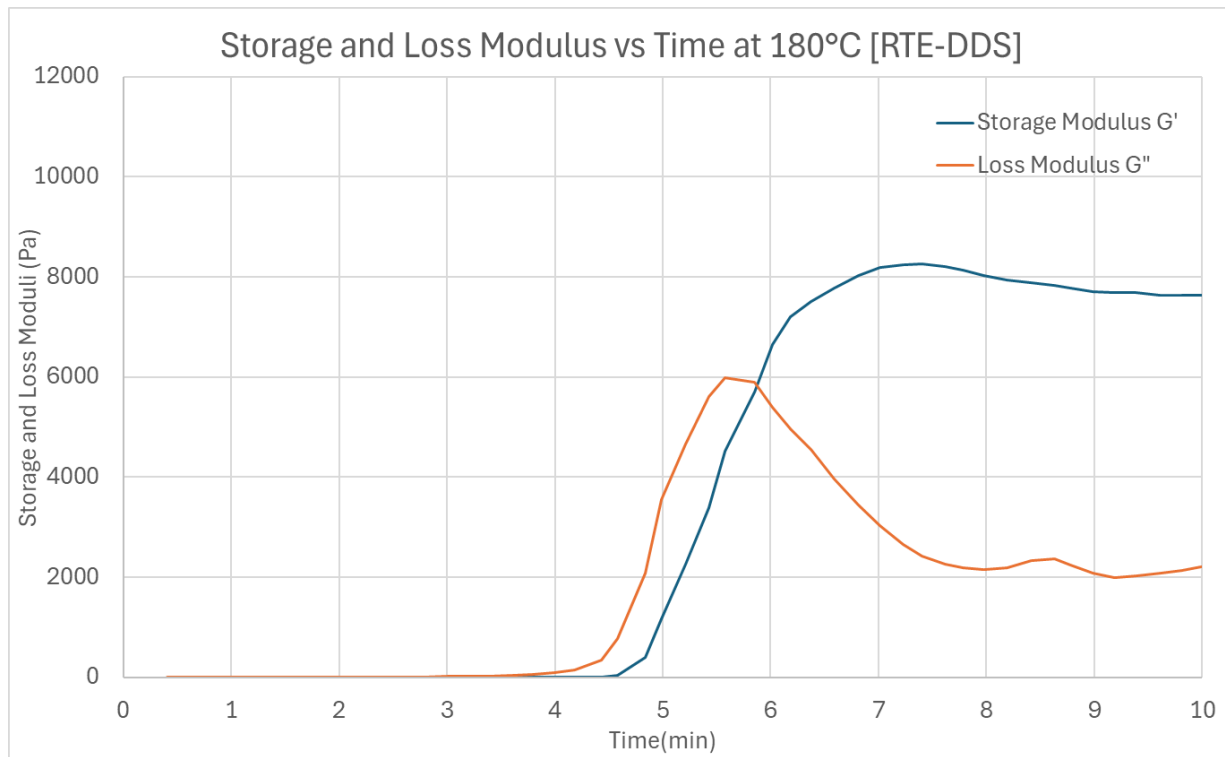


Figure 33. Change in storage and loss moduli with time at 180°C

### 5.1.5. Processing & Curing Cycle Finalisation

The information about the thermal properties of RTE-DDS resin acquired in the previous sections was used to devise the final processing and manufacturing steps for the future neat resin and composite test pieces. The procedure is outlined in Table 7 and can generally be applied for both neat samples and composite manufacturing. However, certain differences arose and are described in more detail in the corresponding sections on resin mechanical testing (See Section 5.3) and composite mechanical testing (See Section 6).

Step Number	Step Description
1.	Mix RTE and DDS in an appropriate stoichiometric ratio.
2.	Store the mixture in the freezer until further processing begins.
3.	Pre-heat the RTE-DDS resin to 100°C for mixing, de-gassing, and pouring into the mould.
4.	Dwell the resin at 120°C for 30 minutes for gas evacuation.
5.	Dwell the resin at 180°C for 120 minutes for curing.
6.	Dwell the resin at 220°C for 60 minutes for post-curing.

Table 7. Summary of processing and manufacturing steps for RTE-DDS resin

## 5.2. Physical Property Analysis

To better understand the physical nature of RTE-based resin and compare it with T742 resin, as well as other commercial and bio-based resin formulations, it was decided to conduct a series of experiments, which include density, water contact angle, water absorption, cure shrinkage, and gel content estimations. Each of the aforementioned parameters is important when considering potential engineering applications of bio-based epoxy composites. For instance, the density of the resin is crucial when determining the specific properties, of the future composite material, i.e., specific stiffness and strength. Higher specific properties of a matrix material mean higher efficiency of the whole structure.

Similarly, the water contact angle is a parameter that can quantify the wettability of the surface by a liquid. As mentioned in Section 3.5.2, one of the main limitations of the current bio-based epoxy resins is their hydrophilic nature. Thus, surface hydrophilicity, also known as wettability, is a crucial parameter that needs to be evaluated for any material potentially exposed to environments containing water. This is because a hydrophilic surface tends to attract and absorb more water, which can either be absorbed by the material or freeze into ice, potentially compromising the performance of the component.

Furthermore, water absorption tests are conducted to establish the proportion of water absorbed by a material, and, consequently, to define a relationship between moisture uptake and mechanical and/or electrical properties, and dimensional stability. Generally, the moisture content of a polymer is closely related to its mechanical performance.

Finally, the gel content is important when considering the conversion of the resin. Knowing the amount of gel content in the resin after curing can serve as an indication of the amount of unreacted material that was present in the resin.

### 5.2.1. Bio-based Content

As reflected in the main goal of the paper and the corresponding research questions, the purpose of this study is to investigate whether resveratrol can be used as a bio-based alternative to synthetic resins originating in petroleum products. Thus, a comparison can be made between RTE-DDS and the common petroleum-based resins: BADGE-DDS and T742-DDS. In the context of sustainable raw materials, the bio-based content serves as a good indication of how resveratrol-derived resin performs against the aforementioned synthetic resins. The molar ratios used in this chapter were acquired using a method described in Appendix A.1. Finally, to achieve a fair comparison it was decided to treat epichlorohydrin as fully bio-based in each epoxy formulation. However, it should be noted that there is no information about the origin of epichlorohydrin in Tactix 742 and BADGE monomers. They are most likely procured from petroleum-based sources.

As previously mentioned, BADGE is formulated using a mixture of BPA and epichlorohydrin. Given a molar ratio of epichlorohydrin to BPA of 2:1, the bio-based content BADGE can be determined. The total number of carbon atoms in BADGE is 21; of these 21 atoms, 15 are

contributed by BPA and are considered petroleum-based. Epichlorohydrin contributes 6 carbon atoms which are assumed to be bio-based. The bio-based carbon content of BADGE is then calculated to be 28.57%. Furthermore, assuming an optimal molar mixing ratio for BADGE-DDS of 2.06:1 and that DDS is fully synthetic, then the number of bio-based atoms contributed by epichlorohydrin is 12.36 ( $2.06 * 6$ ). Given that DDS has 12 carbon atoms, the total number of carbon atoms in BADGE-DDS is 55.26 ( $12 + 21 * 2.06$ ). Thus, the bio-based carbon ratio of BADGE-DDS epoxy is 22.36%.

At the same time, Tactix 742 (generally referred to as THPMTGE) is a commercial resin marketed by Dow Chemical Company. As mentioned in Section 3.1.2, THPMTGE is prepared from THPM and epichlorohydrin. The former has 3 hydroxyl groups each of which reacts with one molecule of epichlorohydrin. Thus, the theoretical molar ratio of THPM to epichlorohydrin is 3:1. If T742 has 28 carbon atoms 9 of which are contributed by epichlorohydrin, then the bio-based carbon content of uncured THPMTGE is approximately 32.14%. Given a molar ratio of T742 to DDS of 1.45:1, the bio-based carbon content of T742-DDS resin becomes 24.81%.

Applying the same logic to RTE-DDS formulation (i.e., assuming fully bio-based RTE (23 carbon atoms) and a molar ratio with DDS of 1.5:1), the bio-based carbon content of the RTE-DDS epoxy resin is 74.19%. Thus, a significant improvement in the sustainability of the epoxy resin formulation can be achieved.

### 5.2.2. Density

The resin density measurement was completed per the ASTM D792 standard for plastics (ASTM, 2020). The method is based on the Archimedes' principle. The test was conducted in standard laboratory conditions with 23 ( $\pm 2^\circ\text{C}$ ) ambient temperature and 50 ( $\pm 10\%$ ) relative humidity. In total, 5 samples were tested for each resin type.

First, the apparent specimen mass in air ( $a$ ) was measured and recorded. Following that, the apparent mass ( $b$ ) of the completely immersed specimen and sinker was measured. The specimen was submerged in distilled water. Finally, the mass ( $w$ ) of the fully immersed sinker without a sample was recorded for each measurement.

The specific gravity of the plastic was then calculated using the given formula:

$$SG_{\frac{23}{23^\circ\text{C}}} = \frac{a}{a + w - b} \quad (9)$$

The density was subsequently calculated with the following equation:

$$\rho_{23^\circ\text{C}} = SG_{\frac{23}{23^\circ\text{C}}} * \rho_{water} \quad (10)$$

where  $\rho_{water}$  – the tabulated value of water density corresponding to the water temperature at which the measurement was made.

Table 8 contains the recorded data together with final density values for RTE and T742 resins. As can be seen from the data, resveratrol-based resin possesses a higher density than T742-based commercial resin. The average density values for RTE and T742 are  $1307.6 \frac{kg}{m^3}$  and  $1288.8 \frac{kg}{m^3}$ . The corresponding standard deviations are 1.7 and 3.8, respectively.

Sample #	<i>a</i> g	<i>b</i> g	<i>w</i> g	$SG_{23}^{23}$ -	$T_{water}$ °C	$\rho_{23^\circ C}$ $\frac{kg}{m^3}$
RTE 1	1.3645	12.6998	12.3786	1.3079	21.1	1305.22
RTE 2	1.3654	12.7037	12.3787	1.3124	21.1	1309.72
RTE 3	1.3665	12.7045	12.3810	1.3102	21.1	1307.51
RTE 4	1.3379	12.6989	12.3809	1.3118	21.1	1309.14
RTE 5	1.3720	12.7058	12.3819	1.3090	21.1	1306.38
T742 1	0.8155	12.5649	12.3791	1.2951	21.7	1292.26
T742 2	0.7164	12.5426	12.3787	1.2967	21.7	1293.85
T742 3	0.7207	12.5435	12.3823	1.2881	21.7	1285.33
T742 4	0.7275	12.5451	12.3830	1.2867	21.7	1283.92
T742 5	0.7204	12.5444	12.3817	1.2917	21.7	1288.94

Table 8. Density measurement data for RTE and T742 resins

### 5.2.3. Water Contact Angle

Water contact angle measurements were performed using an Attension Theta Optical Tensiometer from KSV Instruments. The measurement data was obtained from 5 samples of cured RTE-DDS epoxy resin. Before the measurements took place, the samples were prepared by cleaning them with acetone and drying.

Five samples of each resin with flat surfaces were prepared, thoroughly cleaned with acetone, and dried. The calibration of the instrument was performed by levelling the sample platform using a metal ball 4mm in diameter, as can be seen in Figure 34.

After the calibration had been completed, each sample was placed on the base plate, and a water droplet was placed on top of it. The volume of the water droplet was measured at 5ml using a pipette. Then, a digital image of the sample-droplet interface was taken using a digital camera. The water contact angle on each side of the droplet was then calculated using Attension Theta software.

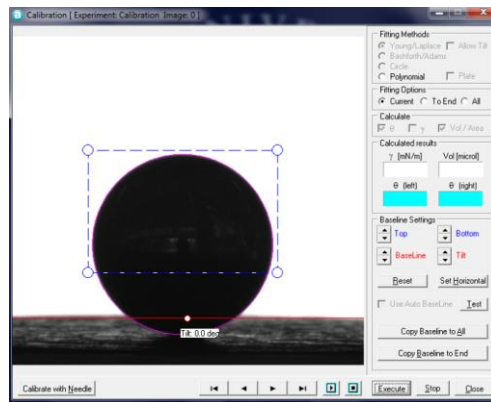


Figure 34. Calibration of the Attension Theta Optical Tensiometer

Figure 35 contains several images of RTE samples being tested. Table 9 contains the water contact angle measurements for RTE and T742 resins. The hydrophilicity of the resin is determined based on the average value of the water contact angle. If this value is equal to or larger than 90°, then the surface is considered hydrophobic. For an angle below 90°, the material surface has hydrophilic properties. As can be seen from the registered data, RTE-based resin has an average water contact angle of 75.51°, while T742 resin possesses a lower average water contact angle of 71.25°. This implies that RTE resin is more hydrophobic than T742. The standard deviation for RTE results was 2.6, while for T742 dataset it stood at 3.

Sample Number	$\theta$ (left)	$\theta$ (right)	Avg.	Sample Number	$\theta$ (left)	$\theta$ (right)	Avg.
RTE 1	78.31	79.57	78.94	T742 1	73.47	72.70	73.09
RTE 2	73.55	73.83	73.69	T742 2	67.28	67.06	67.17
RTE 3	72.24	71.31	71.78	T742 3	69.76	67.30	68.53
RTE 4	77.82	77.07	77.45	T742 4	74.61	75.84	75.23
RTE 5	75.42	75.94	75.68	T742 5	73.21	71.31	72.26

Table 9. Water contact angle measurements for RTE (left) and T742 (right) resins

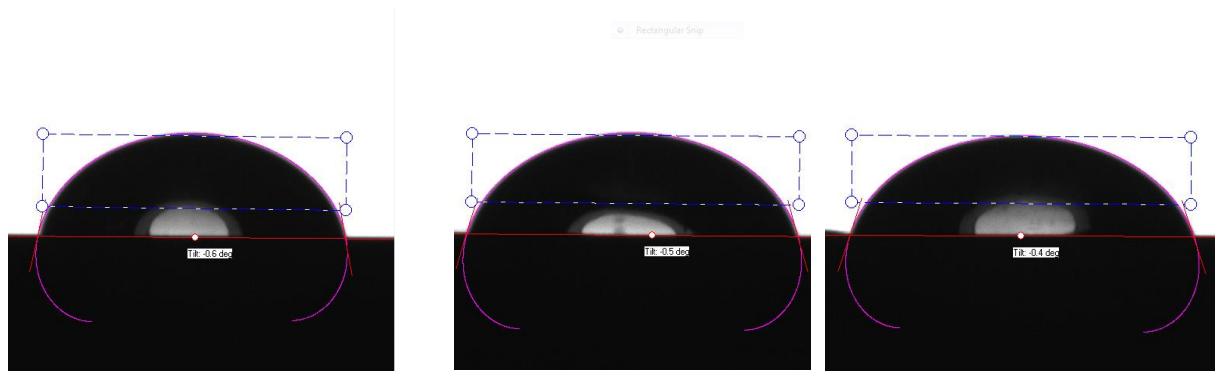


Figure 35. Images of water droplets placed on RTE 1, 2 and 3

#### 5.2.4. Water absorption

The water absorption test of RTE and T742 resins was conducted according to the ASTM D570 (ASTM, 2022a) standard for plastics. 5 test specimens were chosen for each resin type. The specimens were dried in an oven at 50°C for 24 hours prior to the experiment. After that, they were immediately weighed using an analytical balance. The mass ( $m_{dry}$ ) of the dry samples was then recorded in a table. Following that, the specimens were fully immersed in a container of distilled water for 24 hours. Then, the samples were taken out, and all surfaces were wiped off with a dry cloth, after which the samples were weighed again. The mass ( $m_{24h}$ ) after 24-hour immersion was recorded and the samples were placed back in the water container. The process was repeated again at the end of the first and second weeks, with the wet masses recorded as ( $m_{1w}$ ) and ( $m_{2w}$ ), respectively. Table 10 contains dry and wet masses of RTE and T742 specimens.

The change in mass after 2-week immersion was calculated using the following formula:

$$\Delta m = \frac{m_{2w} - m_{dry}}{m_{dry}} * 100 \quad (11)$$

As can be seen from the data RTE has higher water absorption than T742, 1.39% vs 0.97% over two weeks. The standard deviation was 0.04 for RTE and 0.01 for T742.

Sample #	$m_{dry}$ mg	$m_{24h}$ mg	$m_{1w}$ mg	$m_{2w}$ mg	$\Delta m$ %
RTE 1	323.4	325.0	327.0	328.1	1.45
RTE 2	305.6	306.6	308.3	309.7	1.34
RTE 3	317.3	318.3	320.2	321.7	1.39
RTE 4	295.3	296.4	298.1	299.5	1.42
RTE 5	305.0	306.0	307.7	309.1	1.34
T742 1	661.7	664.0	667.6	668.1	0.97
T742 2	634.9	637.1	640.5	641.0	0.96
T742 3	625.4	627.6	630.9	631.4	0.96
T742 4	668.9	671.4	674.9	675.4	0.97
T742 5	562.2	564.1	567.3	567.8	1.00

Table 10. Water absorption data for RTE and T742 resins

### 5.2.5. Gel Content

Gel content is a key indicator of the degree of cross-linking in a chemical structure. This property is assessed through a process where samples are immersed in toluene, which extracts any unreacted monomers and small molecular chains from the material. Thus, the gel content serves as an indicator of the amount of insoluble matter remaining in the sample (Kaltenegger-Uray et al., 2019). To determine the gel content of the RTE-DDS resin and compare it with the T742-DDS alternative, the ASTM D2765 standard for evaluating gel content and swell ratio in cross-linked ethylene plastics was followed (ASTM, 2024).

According to the standard, 2 samples of each resin type were tested. The procedure involved submerging resin samples in toluene for a 72-hour period. After this immersion, the samples were extracted, dried and then weighed. The gel content was then quantified using the following formula:

$$GC = \frac{m_{72h}}{m_{dry}} * 100 \quad (12)$$

where  $GC$  is the gel content in %,  $m_{72h}$  is the mass of the test sample after submersion in toluene for 72 hours in mg,  $m_{dry}$  is the sample mass before submersion.

The measured and computed values are given in Table 11. As can be seen from the data, the gel content of both resins is around 99.95% which indicates a high degree of monomer inter-linking. However, it should be noted that the gel content does not directly correspond to the degree of conversion. Gel content is also influenced by other factors, including molecular weight of the polymer, branching, crystallinity, etc (NHV Corporation, 2023).

Sample #	$m_{dry}$	$m_{72h}$	$GC$
	mg	mg	%
RTE 1	1921.1	1920.27	99.96
RTE 2	1783.0	1782.12	99.95
T742 1	1825.4	1824.55	99.95
T742 2	1641.9	1641.13	99.95

Table 11. Gel content data for RTE-DDS and T742-DDS

### 5.3. Mechanical Property Analysis

In order to get a better overall understanding of the behaviour of the cured epoxy resin under different types of loading and to obtain more data points for comparison with existing BADGE and T742 resins, it was decided to conduct a series of mechanical tests. These include tensile and 3-point bend tests. Although the tensile and flexural properties of PMCs are dominated by the fibre component, the influence of the matrix phase is still important and becomes more so depending on the type of loading. This can be demonstrated by considering the elastic behaviour of a continuous and aligned fibre-reinforced composite under longitudinal and transverse loading.

Assuming longitudinal loading, good fibre-matrix interfacial bonding and an isostrain condition (same deformation in fibre and matrix), the total load carried by the composite is a sum of loads carried by individual phases. From there, the expression for the modulus of elasticity of the composite in the longitudinal direction becomes the following (Callister, William D. & Rethwisch, 2018b):

$$E_{cl} = E_m V_m + E_f V_f \quad (13)$$

Where  $E_m$  – elastic modulus of the matrix;  $E_f$  – elastic modulus of the fibres;  $V_m$  – matrix volume fraction;  $V_f$  – fibre volume fraction.

Similarly, the longitudinal strength of the composite can be derived. Assuming that the failure strain of the fibres is lower than that of the matrix (which is the case for carbon fibre–epoxy composites), the load carried by the fibres is progressively transferred to the matrix as the fibres continue fracturing. This process continues until fibre length reaches the critical value under which it is not able to carry any loads effectively, as discussed in Section 2.2. Assuming that fibres bear no load when the critical length is reached, the load is fully transmitted to the matrix. However, in reality, the matrix failure occurs before all the fibres fail and the composite strength in the longitudinal direction is defined as follows (Callister, William D. & Rethwisch, 2018b):

$$\sigma_{cl} = \sigma_m V_m + \sigma_f V_f \quad (14)$$

where  $\sigma_m$  – stress in the matrix at fibre failure;  $\sigma_f$  – fibre tensile strength.

Given the same continuous and aligned fibre composite under transverse loading, it can be assumed that both phases experience the same stress – referred to as isostress condition. In this case, the modulus of elasticity in the transverse direction can be expressed in the following way:

$$E_{ct} = \frac{E_m E_f}{V_m E_f + V_f E_m} \quad (15)$$

The aforementioned equations are derived by applying the Rule of Mixtures (RoM) which is commonly used for the determination of composite properties (Tam et al., 2012).

At the same time, the transverse strength of a composite is not dominated by the fibre properties and is instead dependent on various factors including matrix properties, void content and fibre-matrix bond strength. However, better mechanical properties of the matrix generally improve the transverse performance of the composite.

On the other hand, the fracture toughness of the polymer matrix plays an important role in defining the overall composite resistance to crack growth. Therefore, it is crucial to define this property for the neat epoxy resin. Before testing the outlined properties of resveratrol-based resin can take place, the samples must be manufactured first. According to the desired tests, three different geometries must be created – for tensile, 3-point Bend and Fracture Toughness testing. On top of that, to facilitate the comparison with T742 resin, it was also decided to produce a set of samples for each test type using this resin.

### 5.3.1. Tensile Specimen Preparation

The geometry of tensile specimens was selected based on the recommendations of the ASTM D638 test standard for tensile properties of plastics (ASTM, 2014). Due to the limited amount of available RTE monomer, it was decided to adopt the Type 5 specimen geometry which requires less material than other geometry types due to reduced thickness. The dogbone geometry of the tensile sample is illustrated in Figure 36. The nominal dimensions of each sample must be as follows: thickness – 4mm, overall length (LO) – 63.5mm, overall width (WO) – 9.53mm, width of the narrow section (W) – 3.18mm. For the remaining dimensions and corresponding tolerances, the reader is referred to the standard.

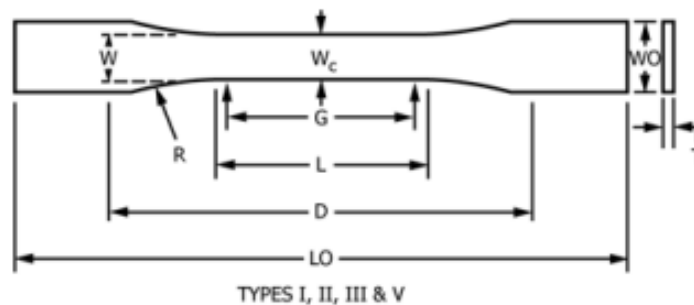


Figure 36. Illustration of a dogbone geometry used for tensile testing

The specimens were to be manufactured using a mould that consists of two outer parts with machined bolt holes and funnels to enable easy pouring of the resin. Sandwiched between these two is a central plate with 4 cavities which agree with the Type 5 geometry requirements. The central plate is made of steel to achieve lower thermal expansion and better hardness. This is important to reduce the sample-to-sample variation in dimensions and surface quality.

The preparation of the resin started with estimating the amount required to fill in all 4 sample cavities. The total amount of resin (monomer + hardener) used per manufacturing cycle was approximately 20 – 25g. The resin constituents were then weighed and mixed in appropriate

amounts following the defined mass ratios for RTE – DDS (2.39:1) and T742 – DDS (2.69:1). To prevent any premature cross-linking, the mixtures were then stored in refrigerators at  $-25^{\circ}\text{C}$ . The following process is described for the RTE-DDS resin mixture. However, the T742-DDS mixture required identical processing conditions.

Next, the mould preparation took place which involved the cleaning of the inner surfaces and funnels of the aluminium parts using acetone. Each surface was cleaned at least 3 times with 1 minute in between to allow acetone to properly evaporate. After the surfaces were properly cleaned, the application of the release agent took place. 3 layers of Marbcote 227 release agent were applied on every cleaned surface to enable simpler sample removal and mould cleaning after curing. A waiting time of 3 minutes was followed between every application to let the release agent fully dry up. On top of that, the bolts used to close the mould were treated with Beeswax to prevent the liquid resin from solidifying inside the thread holes in case a leak happens. After that, the mould was assembled and placed into an oven for preheating at  $120^{\circ}\text{C}$ .

Following the mould preparation, the mixed resin was preheated at  $100^{\circ}\text{C}$  until the monomer was fully melted and the hardener started dissolving in it. The selection of temperature for processing was based on the results of DSC and rheometry investigations of RTE. The maximum preheating temperature was also limited by the material of the available resin containers, which were made of polypropylene (PP). It was observed that at temperatures around  $120^{\circ}\text{C}$ , PP starts to soften up significantly compromising the structural integrity of the container.

To fully dissolve DDS in RTE and to achieve a fully homogeneous mixture, the resin container was then placed in a speed mixer under vacuum conditions. The vacuum was essential for de-gassing the resin before moulding. Thus, the lid of the container was punctured beforehand and a perforated bandage was placed over the hole beforehand, to allow air removal and prevent potential resin spillage inside the speed mixer. The necessity for de-gassing was established by the presence of voids in cured tensile samples as a result of entrapped air not being able to escape the mould cavity (See Figure 37). Thus, the resin was mixed for 5 minutes under 40 mbar pressure at 2000 RPM.

After the first mixing/de-gassing cycle, the resin was placed in the oven at  $100^{\circ}\text{C}$  for another 10 minutes to reheat. Subsequently, the resin was de-gassed again to further reduce void formation. The same cycle was used for de-gassing, as previously. This proved especially beneficial for tensile samples due to the narrow cross-sections of the mould cavity (as compared to 3-point bend mould). The reheating of the resin was necessary to reduce the viscosity of the resin, and to allow the air bubbles to leave the substance with more ease.

Subsequently, the resin was placed in the oven again for 10 minutes. As previously mentioned, reheating lowers the viscosity of the resin, which is crucial for successful moulding. As mentioned in Section 5.1.4, the viscosity of RTE-DDS is around 0.45 Pas at  $100^{\circ}\text{C}$ . At this value, the resin can be easily poured from the container into the cavity of the mould avoiding clogging the narrow section. After heating the resin and the mould to  $100^{\circ}\text{C}$  and  $120^{\circ}\text{C}$ , respectively, the resin is poured into the mould at a low rate to avoid clogging. After filling in approximately a third of each

specimen cavity, the resin and the mould are reheated once again for 10 minutes; the second third is then poured into the mould. The process is repeated for the third time to pour in the remaining material. Filling in the mould in three approaches is done to allow the resin to properly settle inside each cavity pushing out the air.

Next, the resin was subject to curing inside an oven with a pre-defined curing cycle which was derived based on DSC and rheometry data. The curing cycle consisted of the following steps: (1) dwell at 120°C for 30 minutes to give any entrapped air time to leave the mould before curing starts, (2) increase the temperature to 180°C at 2.5 °C/min, (3) dwell at 180°C for 120 minutes, (4) increase the temperature to 220°C at 2.5 °C/min, (5) dwell at 220°C for 60 minutes for post-curing, (6) decrease the temperature to 30°C 6 °C/min inside the oven. Cooling at a faster rate outside of the oven led to crack formation in the cured samples due to material contraction (See Figure 38).



Figure 37. Tensile mould not filled in due to trapped air

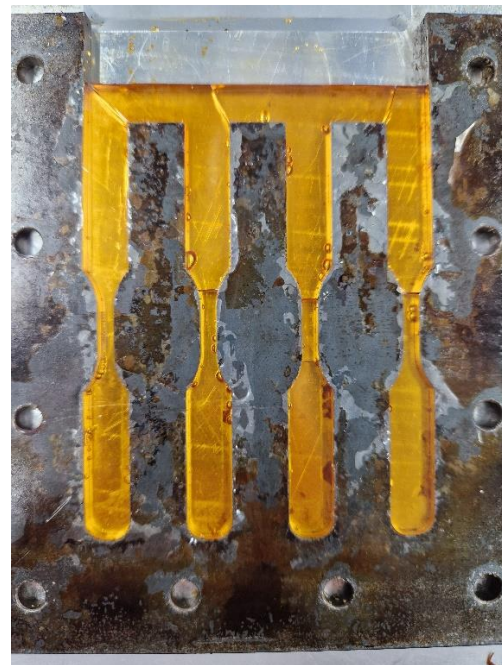


Figure 38. Cracking of tensile samples due to thermal contraction

After curing, the samples were cut to the appropriate size for testing and the dimensions were measured in accordance with ASTM D638 requirements. The dimensions were measured three times using a digital calliper with an accuracy of 0.025mm. The width and the thickness of each specimen were measured and within 5mm of each end of the gauge length. The average of these values was used for further calculations. Table 12 and Table 13 present the average dimensions of RTE and T742 samples, respectively.

Sample #	Overall Length (mm)	Overall Width (mm)	Section Width (mm)	Thickness (mm)
RTE 1	73.96	9.63	3.46	4.00
RTE 2	74.43	9.56	3.19	3.96
RTE 3	74.55	9.54	3.27	3.97
RTE 4	74.43	9.38	3.27	3.95
RTE 5	74.48	9.32	3.31	3.93

Table 12. Average dimensions of RTE tensile specimens

Sample #	Overall Length (mm)	Overall Width (mm)	Section Width (mm)	Thickness (mm)
T742 1	74.71	9.64	3.33	3.95
T742 2	75.28	9.69	3.41	3.96
T742 3	75.33	9.63	3.37	3.98
T742 4	75.38	9.65	3.42	3.98
T742 5	75.21	9.66	3.39	3.96

Table 13. Average dimensions of T742 tensile specimens

### 5.3.2. Tensile Testing & Results

The tensile testing of the specimens was conducted using the ZwickRoell Universal Testing Machine. The tests were conducted according to the requirements of the ASTM D638 standard. Thus, 5 samples were tested for each material, and the tests were considered valid as long as the specimens fractured within the narrow section. The speed of testing (i.e., the rate of crosshead motion) was selected to be 1 mm/min. The tests were conducted at the same temperature and humidity. Figure 39 presents RTE samples that were tested. As can be seen from the figure, some samples contained voids that had occurred during manufacturing. However, their influence on the test outcome was considered negligible as long as no defects had been observed in the neck section prior to testing and the failure had occurred in the neck section. The test results were considered valid only if these two criteria had been met. The samples were firmly secured with the clamps. The grip-to-grip separation was selected to be 25.4mm in accordance with Type 5 specimen geometry.

The output of each experiment was presented in the form of a dataset, which comprised the standard force applied to the sample and the standard travel of the grips relative to the initial position. Thus, after collecting the raw data, it was necessary to process it to extract the desired

output parameter, the ultimate tensile strength (UTS), for each sample. This was done by transforming the data from force-displacement into the stress-strain domain. On top of that, elastic modulus was estimated based on the initial linear portion of the stress-strain curve. Having said that, the estimated modulus values should be treated with caution since they were obtained based on the change in grip separation. This is not a recommended practice due to potential errors between actual deformation and the jaw movement. The use of an extensometer is recommended in the standard for acquiring more accurate results. However, such a device was not available when the testing took place.



Figure 39. RTE-DDS tensile samples

Sample #	Stress at Break (MPa)	Strain at Break (%)	Elastic Modulus (GPa)	Sample #	Stress at Break (MPa)	Strain at Break (%)	Elastic Modulus (GPa)
RTE 1	42.55	2.55	2.13	T742 1	72.06	3.39	2.63
RTE 2	39.95	1.85	2.49	T742 2	70.40	3.34	2.60
RTE 3	45.13	2.22	2.43	T742 3	64.20	2.94	2.59
RTE 4	42.80	2.18	2.31	T742 4	46.76	2.54	2.44
RTE 5	49.41	2.71	2.21	T742 5	68.04	4.07	2.50
Avg.	43.97	2.30	2.31	Avg.	63.36	3.05	2.57
SD	3.12	0.30	0.13	SD	10.02	0.35	0.08

Table 14. UTS, strain at break and elastic modulus values for RTE and T742 samples

Table 14 presents the values of the stress at break, strain at break and modulus of elasticity for RTE and T742 resins. Thus, the average tensile strength of RTE-DDS was 43.97 MPa with 2.31 GPa elastic modulus. For T742-DDS, these values were at 63.36 MPa and 2.57 GPa, respectively. The calculated standard deviations are also presented in the table. While for RTE samples the values of SD are relatively low for all parameters, a significantly higher variation is observed for stress at break of T742 samples. Such variation in data points can also be seen from

the load-displacement curve in Figure 40. The variation in sample failure behaviour could be attributed to manufacturing-related imperfections, such as micro-voids and cracks, that had not been detected during the pre-test inspection.

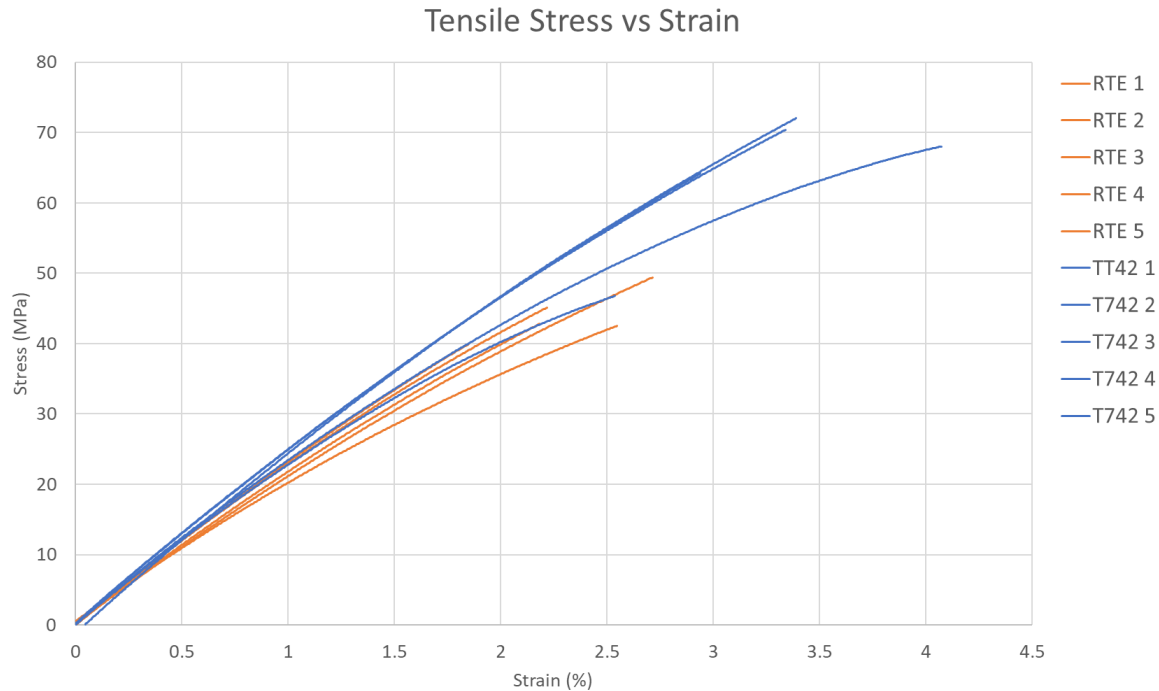


Figure 40. Tensile test load-displacement curve for RTE-DDS and T742-DDS

### 5.3.3. 3-Point Bend Specimen Preparation

The preparation of the 3-point bend samples was generally similar to the process described previously. The geometry of the samples was defined according to the standard test method for flexural properties of unreinforced plastics described in ASTM D790 (ASTM, 2010). According to the requirements presented in the standard, for materials with a thickness greater than 1.6mm, the support span shall be 16 times that, while the width shall not exceed one fourth of the span. Moreover, the overhang on each end of the specimen should be at least 10% of the support span.

The mould used for the preparation of the 3PB samples is the same as in the case of tensile specimens. The only difference constitutes a different central steel plate with one large rectangular cavity instead of 4 tensile cavities. The thickness of the central plate defines the thickness of the samples and is equal to 4mm. Thus, each 3PB sample must have a rectangular shape with the nominal dimensions as follows: length – between 72mm and 76.8mm, maximum width – 16mm.

The estimated amount of resin needed to fill in the rectangular mould turned out to be approximately 40g. Both RTE and T742 were weighed and mixed in appropriate ratios. The mould was prepared, and the resin was mixed until homogeneous and degassed using the speed mixer. The procedure is identical to that described in Section 5.3.1. However, in the case of 3-point bend sample moulding, it was not necessary to degas the resin mixture for the second time to prevent

void formation. Due to the larger cross-sectional area of the mould cavity, it was easier for the trapped air to leave the mould during pouring.

Once the resin had been properly mixed and de-gassed, it was reheated in the oven for 10 minutes at 100°C. It was then slowly poured into the mould while moving the front of the resin from one edge of the cavity to the other. Similarly to the second de-gassing, it was not necessary to perform the pouring in multiple approaches because of the larger cross-section of the mould cavity. The resin was then cured using the same cycle as described previously. The fully cured rectangular panel is shown in the Figure 41.

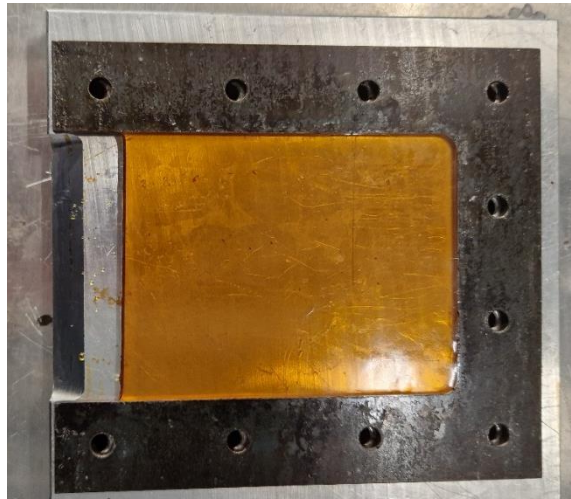


Figure 41. Rectangular RTE-DDS panel

The panel was then cut into separate 3-point bend samples and each sample was measured in a similar manner to tensile specimens. In total, 5 samples of each material were selected for testing based on their quality. The samples' dimensions are presented in Table 15 and Table 16.

Sample Number	Length (mm)	Width (mm)	Thickness (mm)
RTE 1	74.59	9.81	3.97
RTE 2	74.77	10.16	3.92
RTE 3	74.71	10.16	3.92
RTE 4	74.68	10.15	3.89
RTE 5	74.68	10.15	3.90

Table 15. Average dimensions of RTE 3-point bend specimens

Sample Number	Length (mm)	Width (mm)	Thickness (mm)
T742 1	74.54	9.63	3.95
T742 2	74.70	9.36	3.91
T742 3	74.68	9.73	3.89
T742 4	74.62	8.75	3.92
T742 5	74.73	10.47	3.89

Table 16. Average dimensions of T742 3-point bend specimens

### 5.3.4. 3-Point Bend Testing & Results

Similar to the tensile testing, the three-point bend testing was conducted on the ZwickRoell Universal Testing Machine. The test was set up and conducted according to the ASTM D790 standard for flexural testing of plastics. For the purpose of the experiment, a different tool head was used to accommodate the upper anvil with a central loading edge that has a 5mm radius as per ASTM D790. The flexure fixture that supports the specimen was adjusted to comply with the following equation, as defined by ASTM D790:

$$L = (16 \pm 1)t \quad (16)$$

In the aforementioned equation,  $L$  is the support span and  $t$  is the mean thickness of the specimen. Furthermore, the rate of crosshead motion was calculated with the following equation:

$$R = \frac{ZL^2}{6t} \quad (17)$$

where  $Z$  is the rate of straining of the outer fibre and is given as  $0.01 \frac{mm}{mm}$ . Thus, the span and the rate of crosshead motion were selected for each test considering the sample thickness. Each sample was placed in the machine so that the supports and the loading nose were parallel. The specimens were centred on the supports and tested as can be seen in Figure 42. All of the tested samples are shown in Figure 43.



Figure 42. RTE sample loaded in 3-point bending



Figure 43. RTE specimens for 3PB

The collected data for each specimen was first recorded in the standard force/travel format and compiled in an Excel table. Next, an analogous procedure to the one described in Section 5.3.2 was performed to transform the data into the stress-strain domain. However, for flexural stress and strain, a different set of equations was employed.

For a beam made of homogeneous and elastic material, simply supported at 2 ends, and loaded at midpoint, the maximum stress develops in the midpoint of the outer surface. For the derivation of the flexural stress at any point of the load-deflection curve, the following equation for the normal stress in a beam was used:

$$\sigma_f = \frac{3PL}{2bt^2} \quad (18)$$

Here, P – load at a given point of the curve, b – width of the specimen,  $\sigma_f$  – stress in the outer fibres at the midpoint. It should be noted that the equation is only valid for specimens which experience strains of less than 5%.

Similarly, the maximum strain on the outer surface of a specimen develops midspan where the maximum deflection is. The flexural strain was calculated with the following formula:

$$\varepsilon_f = \frac{6Dt}{L^2} \quad (19)$$

Finally, in order to calculate the modulus of elasticity in bending, the following equation was employed:

$$E_B = \frac{L^3 m}{4bt^3} \quad (20)$$

where m – is the gradient calculated for the tangent to the steepest initial straight-line section of the load-deflection curve.

Table 17 contains the values of flexural stress at break ( $\sigma_{fB}$ ), strain at break ( $\varepsilon_f$ ) and flexural elastic ( $E_B$ ) modulus calculated for the RTE and T742 data. Furthermore, Figure 44 shows the stress-strain curves for the corresponding data.

Sample #	$\sigma_{fB}$ (MPa)	$\varepsilon_f$ (%)	$E_B$ (GPa)	Sample #	$\sigma_{fB}$ (MPa)	$\varepsilon_f$ (%)	$E_B$ (GPa)
RTE 1	108.28	4.63	2.77	T742 1	105.48	3.67	3.20
RTE 2	98.65	4.01	2.93	T742 2	104.55	3.33	3.35
RTE 3	109.31	4.31	3.06	T742 3	126.67	4.42	3.43
RTE 4	122.93	5.04	3.07	T742 4	127.64	4.39	3.38
RTE 5	91.33	3.46	2.99	T742 5	116.54	3.75	3.40
Avg.	106.10	4.29	2.96	Avg.	116.18	3.91	3.35
SD	10.7	0.54	0.12	SD	9.91	0.43	0.08

Table 17. Flexural stress at break, strain at break and flexural elastic modulus values for RTE

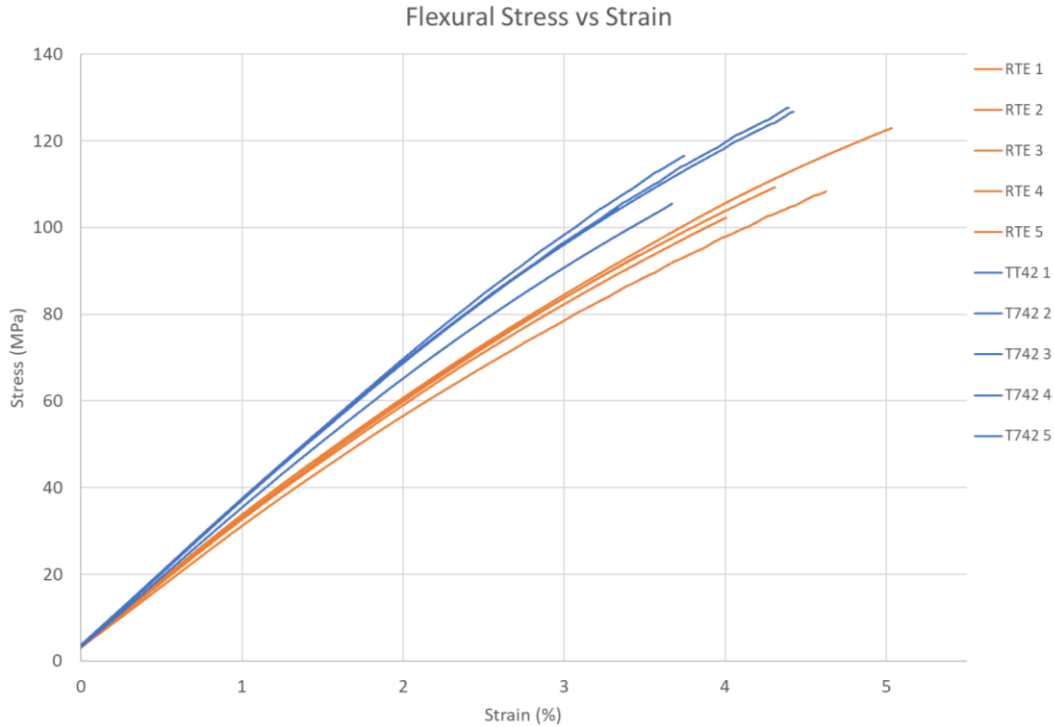


Figure 44. Flexural test load-displacement curve for RTE and T742 samples

As can be seen from the results, the flexural properties of RTE and T742 resins are very similar. However, according to the data, the T742 resin possesses higher stiffness, 3.35 GPa vs 2.96 GPa, which constitutes a 12% difference. On top of that, the flexural strength of the RTE resin is lower than that of T742 resin, at an average of 106.10 MPa vs 116.18 MPa (6.5% lower). Finally, RTE resin does have a higher deflection at break of 4.3% (vs 3.91% of T742). As with tensile test results, some variation in the data can be observed for 3-point bending. Standard deviations of 10.7 and 9.91 were calculated for the flexural strengths of RTE and T742, respectively.

### 5.3.5. Fracture Toughness Specimen Preparation

The preparation of the fracture toughness samples was completed following the ASTM D5045 standard method for plain-strain fracture toughness of plastic materials (ASTM, 2019). The test method allows for determining the critical stress intensity factor ( $K_{IC}$ ) at fracture initiation. The sample geometry corresponds to the requirements presented for the single-edge-notch bending (SENB) test. As is the case with previously discussed tests, it was first necessary to define the limits of the acceptable specimen dimensions. According to the ASTM standard, the general setup for the SENB test is as can be seen from Figure 45.

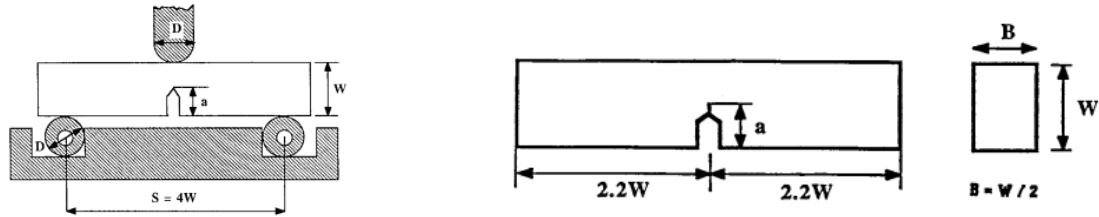


Figure 45. Test setup and sample dimensions considered in the SENB fracture toughness test

The SENB samples were manufactured using the same mould configuration as used for 3PB specimens. Thus, the sample thickness,  $B$ , is limited to 4mm nominally. As can be seen from the figure above, the width of the sample,  $W$ , must be twice the thickness. With the given nominal thickness, the width then becomes 8mm. At the same time, the length of the sample is defined as 4.4 times the width, amounting to 35.2mm.

After defining the nominal dimensions of a SENB sample for fracture toughness testing, a panel of neat resin was manufactured using the same mould configuration and process used for 3-point bend specimens. The cured panel was then cut according to the defined nominal dimensions with corresponding tolerances applied.

According to the standard, it was then necessary to initiate a crack in the width-wise direction of each tested specimen. The total crack length ( $A$ ), in this case, would be the sum of notch length ( $a$ ) and crack length ( $\delta a$ ). The standard imposes additional requirements to limit the dimensions of the crack. First of all, the total crack length is limited to between 0.45 and 0.55 times the width of the sample. Secondly, the minimal crack length must be at least 2 times longer than the width of the notch ( $w$ ). Finally, the maximal crack length must not be larger than the difference between the maximal total crack length and the notch length.

Thus, the limits are summarised with the following formulae:

$$0.45 < \frac{A}{W} < 0.55 \quad (21)$$

$$2w < \delta a < A_{\max} - a \quad (22)$$

A sharp notch (2.5 – 4mm in length) was created in each specimen using a saw of 0.4mm thickness (thinnest available). After that, a crack was initiated from the bottom of the notch by inserting a razor blade and tapping. A fresh razor blade was used for each specimen, and the tapping continued until visible crack propagation occurred in the sample. The standard recommends that at least 3 specimens should be tested for each material condition. Due to the unpredictable nature of crack propagation, multiple samples were destroyed before achieving a sufficient number of specimens.

Once a crack had been successfully initiated, the dimensions of the notch were measured using a microscope. The dimensions were then checked to be in agreement with the defined limits, which are given in Table 20. Figure 46 demonstrates the microscope measurements of crack dimensions

for the RTE 5 specimen. Table 18 and Table 19 contain the specimen and crack/notch dimensions for the valid samples that were used for testing.

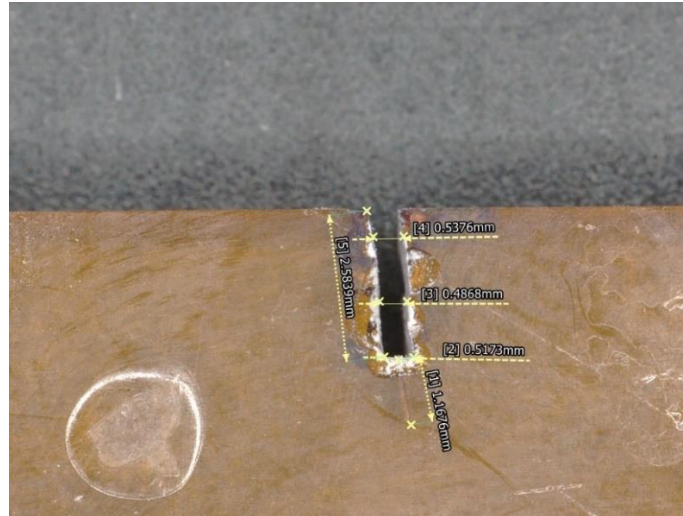


Figure 46. Crack dimensions of RTE 5 specimen

Sample #	Length, L (mm)	Width, W (mm)	Thickness, B (mm)	Total crack length, A (mm)	Notch width, w (mm)	Notch length, a (mm)	Crack length, $\delta a$ (mm)
RTE 1	35.16	8.21	3.91	3.8458	0.5080	2.5563	1.2895
RTE 2	36.1	8.09	3.90	4.0453	0.5122	2.5379	1.5074
RTE 3	35.14	8.13	3.86	3.6579	0.5041	2.3911	1.2668
RTE 4	35.89	9.20	3.89	4.1421	0.5376	2.3935	1.7486
RTE 5	36.42	7.79	3.96	3.7515	0.5139	2.5839	1.1676

Table 18. Average dimensions of RTE fracture toughness specimens and the corresponding notch data

Sample #	Length, L (mm)	Width, W (mm)	Thickness, B (mm)	Total crack length (mm)	Notch width, (mm)	Notch length (mm)	Crack length, $\delta a$ (mm)
T742 1	35.41	8.61	3.95	4.0632	0.5817	2.3937	1.6695
T742 2	35.80	8.16	3.96	3.7446	0.5791	2.5457	1.1989
T742 3	35.23	8.42	3.99	4.0785	0.5413	2.7384	1.3401
T742 4	36.28	8.05	3.98	3.9860	0.6027	2.6472	1.3388
T742 5	35.98	8.21	3.98	4.5036	0.5546	2.9322	1.5714

Table 19. T742 SENB specimen and notch dimensions

Sample #	Min A (mm)	Max A (mm)	Min $\delta a$ (mm)	Max $\delta a$ (mm)
RTE 1	3.69	4.52	1.01	1.96
RTE 2	3.64	4.45	1.02	1.91
RTE 3	3.66	4.47	1.01	2.08
RTE 4	4.14	5.06	1.08	2.67
RTE 5	3.51	4.28	1.03	1.70
T742 1	3.87	4.74	1.16	2.34
T742 2	3.67	4.49	1.16	1.94
T742 3	3.79	4.63	1.08	1.89
T742 4	3.62	4.43	1.21	1.78
T742 5	3.69	4.52	1.11	1.58

Table 20. Crack length requirements for RTE and T742 specimens

### 5.3.6. Fracture Toughness Testing & Results

The testing setup used was identical to the one used in Section 5.3.4. Figure 47 shows the fully prepared SENB samples before testing. The specimens were loaded in 3-point bending, as can be seen from Figure 48. Each SENB specimen was tested at identical ambient conditions. The rate of crosshead motion was selected to be  $1.67 * 10^{-4} \frac{m}{s}$ , according to the ASTM D5045 standard.



Figure 47. RTE-DDS SENB specimens



Figure 48. SENB sample installed in the fixture

A load-deflection curve was obtained for each specimen, such as the one exhibited in Figure 49. Further analysis was performed according to the standard. First, the initial compliance (C) was determined by drawing a best straight line (AB) to the load-deflection curve. C was given by the reciprocal of the slope of the AB line. Next, a line (AB') that corresponds to 5% greater compliance than that of AB was drawn. In case the maximum load ( $P_{max}$ ) the specimen endured falls between the AB and AB' lines, then  $P_{max}$  is used to determine  $K_Q$ . Otherwise, the intersection of AB' and the load-deflection curve must be used to find  $P_Q$ . For all tested specimens,  $P_{max}$  was used for the determination of  $K_Q$ .

$K_Q$  was calculated using the following formula:

$$K_Q = \left( \frac{P_{max}}{BW^{0.5}} \right) f(x) \quad (23)$$

Here, B – specimen thickness (in cm), W – specimen width (in cm), and  $P_{max}$  – maximum load from the curve (in kN).

The values of  $f(x)$  are tabulated in the standard and can be selected using the following criterion:

$$x = \frac{A}{W} \quad (24)$$

where A – total crack length (in cm) as recorded Table 18 and Table 19.

Alternatively,  $f(x)$  was determined using the following equation:

$$f(x) = 6x^{0.5} \frac{[1.99 - x(1-x)(2.15 - 3.93x + 2.7x^2)]}{(1 + 2x)(1 - x)^{1.5}} \quad (25)$$

After calculating  $K_Q$  for each specimen, its validity was checked using the size criteria listed below:

$$2.5 \left( \frac{K_Q}{\sigma_y} \right)^2 < B, A, W - A \quad (26)$$

where  $\sigma_y$  – is the yield stress acquired from a uniaxial tensile test for the maximum load (See Section 5.3.2).

If all of the criteria are satisfied, then  $K_Q = K_{Ic}$ . Otherwise, the test result is not valid. The calculated values of fracture toughness can be seen in Table 21. The average fracture toughness of RTE samples is 47% higher than T742 specimens,  $0.74 \text{ MPa} \cdot \text{m}^{0.5}$  vs  $0.46 \text{ MPa} \cdot \text{m}^{0.5}$ . The corresponding standard deviations are 0.11 and 0.06.

Sample #	$P_{max}$ kN	$B$ m	$A$ m	$W - A$ m	$2.5 \left( \frac{K_Q}{\sigma_y} \right)^2$ -	Validity -	$K_{Ic}$ $MPa * m^{0.5}$
RTE 1	0.0312	0.0039	0.0038	0.0044	0.0012	Valid	0.85
RTE 2	0.0257	0.0039	0.0040	0.0040	0.0010	Valid	0.78
RTE 3	0.0258	0.0039	0.0037	0.0045	0.0008	Valid	0.68
RTE 4	0.0343	0.0039	0.0041	0.0051	0.0011	Valid	0.84
RTE 5	0.0194	0.0040	0.0038	0.0040	0.0005	Valid	0.55
T742 1	0.0209	0.0040	0.0041	0.0045	0.0002	Valid	0.55
T742 2	0.0153	0.0040	0.0037	0.0044	0.0001	Valid	0.40
T742 3	0.0148	0.0040	0.0041	0.0043	0.0001	Valid	0.41
T742 4	0.0137	0.0040	0.0040	0.0041	0.0001	Valid	0.41
T742 5	0.0145	0.0040	0.0045	0.0037	0.0002	Valid	0.51

Table 21. Fracture toughness of RTE and T742 and parameters used for test validity

SENB data analysis for RTE 3

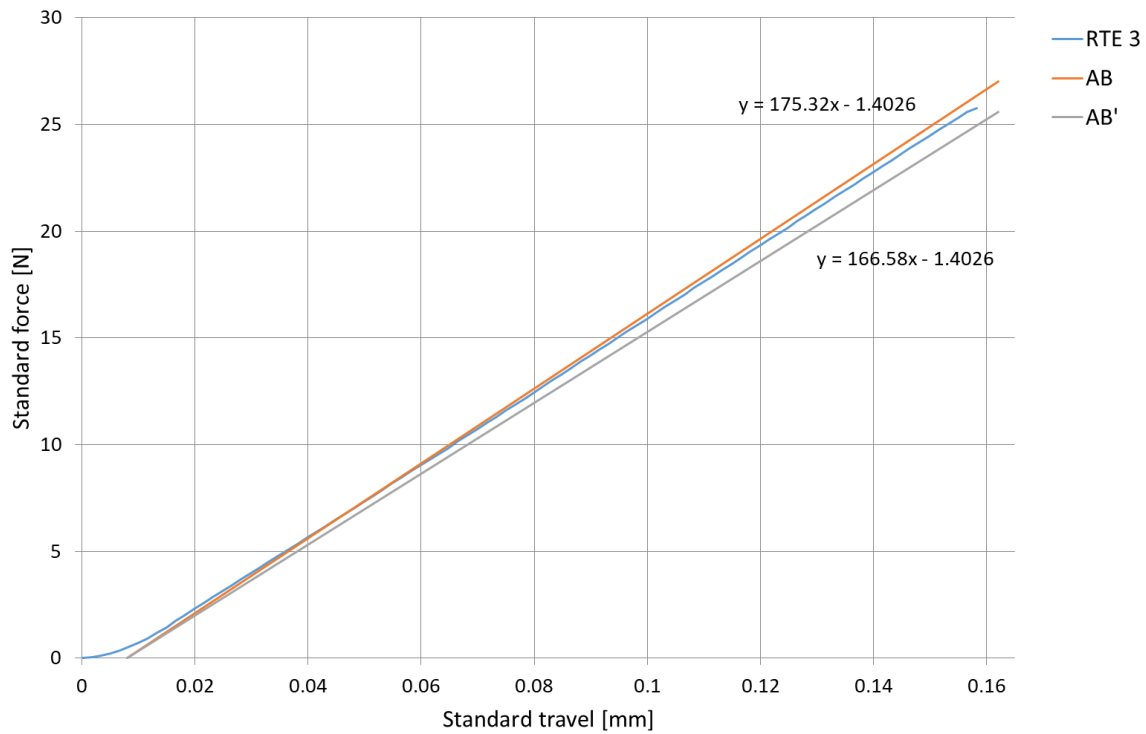


Figure 49. Load-deflection curve with AB and AB' lines for RTE 3

## 6. Composite Manufacturing & Testing

To obtain a better understanding of the properties of RTE-DDS resin in a composite system, it was decided to manufacture carbon fibre-reinforced polymer (CFRP) specimens to perform further experiments. The tests were chosen based on the composite properties that to a large extent depend on the parameters of the matrix material.

As mentioned in the literature review, such composite properties include:

- Compressive strength;
- Inter-laminar shear strength (ILSS);
- In-plane shear strength (IPSS).

### 6.1. Specimen Design & Manufacturing

#### 6.1.1. Wet Lay-Up & Autoclave Curing

Initially, several manufacturing processes were considered for the production of the test panel, including hot pressing and vacuum bagging in an oven. However, it was ultimately decided to proceed with a more sophisticated production process – autoclave curing. Autoclaves are commonly employed in the aerospace industry to manufacture high-performance composite laminates. Given the high viscosity and consequently poor wetting properties of the resin at lower temperatures, it is necessary to perform curing at elevated temperature conditions. This could be achieved in an oven, however, another important consideration at the planning stage was the uniform resin distribution throughout the layers of the laminate. It was believed that curing at elevated temperatures with the application of a vacuum would be insufficient to distribute the resin homogeneously over the surface of the panel. Consequently, this could lead to such defects as voids and dry spots. On the other hand, curing at elevated temperature and pressure in an autoclave helps to spread the resin uniformly and minimise the void content as the excess resin leaves the laminate carrying away entrapped air, volatiles and bubbles (Mallick, 2017c).

Before autoclaving took place, several considerations had been made. First of all, given the defined properties that had to be quantified, the most appropriate testing methods were selected using the ASTM standards. As such, the compressive properties were to be defined using the ASTM D6641 standard, the inter-laminar bonding was to be characterised using the ASTM D2344, while the in-plane shear properties were to be found according to the ASTM D3518 standard. The overall composite panel dimensions were defined based on the dimensional requirements given in each standard. It was decided to cut all test specimens from one panel with an area of 400mm by 300mm. This eliminated the possibility of quality variations if multiple individual manufacturing cycles had been used.

A bi-axial non-crimp carbon fibre fabric was chosen as a reinforcement material (Faserverbundwerkstoffe GmbH, 2024). A minimum panel thickness of 2mm was aimed for as required by the ASTM D2344 standard for ILSS testing. Given the approximate dry fabric

thickness of 0.25mm and accounting for compaction during the autoclaving process, a total of 12 fabric layers was used (i.e., 24 plies given the bi-axial fabric). The sufficient laminate thickness was later confirmed by manufacturing a smaller test panel.

The amount of resin needed per panel was estimated based on the panel dimensions, number of bi-axial layers, area density of the fabric (given by the manufacturer) and fibre weight fraction. Since the most common fibre volume fraction in high-performance composites is between 50% and 65%, it was decided to use a 50% fibre weight fraction per layer for initial calculations. On top of that, to account for the resin leakage from the panel during manufacturing, safety factors of 3 and 2 were applied to the amount of resin used in the first and second layers of the laminate, respectively. Ultimately, for a 400x300mm panel, approximately 370g of resin was used. The RTE monomer and DDS hardener were combined at the stoichiometric ratio, mixed and de-gassed using a Speedmixer, and stored in a refrigerator until lay-up.

The vacuum bagging process started with the preparation of the metal plate (mould). A steel plate of 5mm thickness was chosen to enable sufficient heat transfer to the bottom layers of the laminate and to prevent bending due to the pressure cycle inside the autoclave. The metal plate was cleaned and covered with Marbcote 227 release agent, after which the layers of release film, peel ply and breather fabric were applied as illustrated in Figure 50 and a corresponding schematic in Figure 51.



Figure 50. Prepared mould

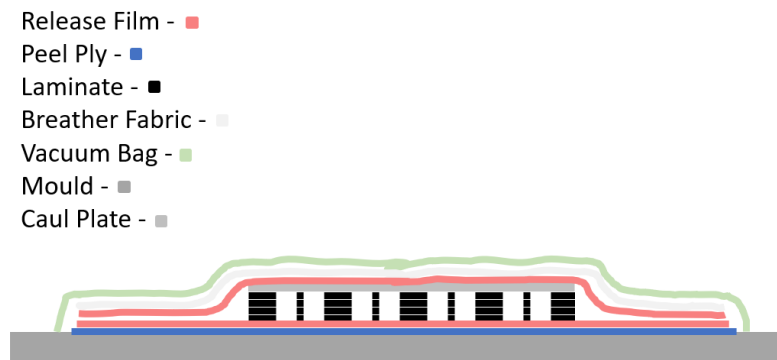


Figure 51. Schematic of a mould layup

Following the mould preparation, the resin was pre-heated and split into separate cups (one per layer). Each cup contained the amount of resin calculated for that specific layer. The resin was applied on each fabric layer using a brush and assisted with a heat gun to improve wettability. Following the manufacturing of a smaller test panel, it was found that the thickness of the laminate was not uniform. Thus, it was decided to use a Caul plate which improves part surface finish and enables uniform pressure distribution in the autoclave (Davé & Loos, 2000b). A vacuum bag was then placed over the entire assembly and connected to the mould via tacky tape. After checking the vacuum, the assembly was placed in an autoclave for curing. The curing cycle was designed according to the conclusions summarised in Section 5.1.5 and is shown in Figure 52.

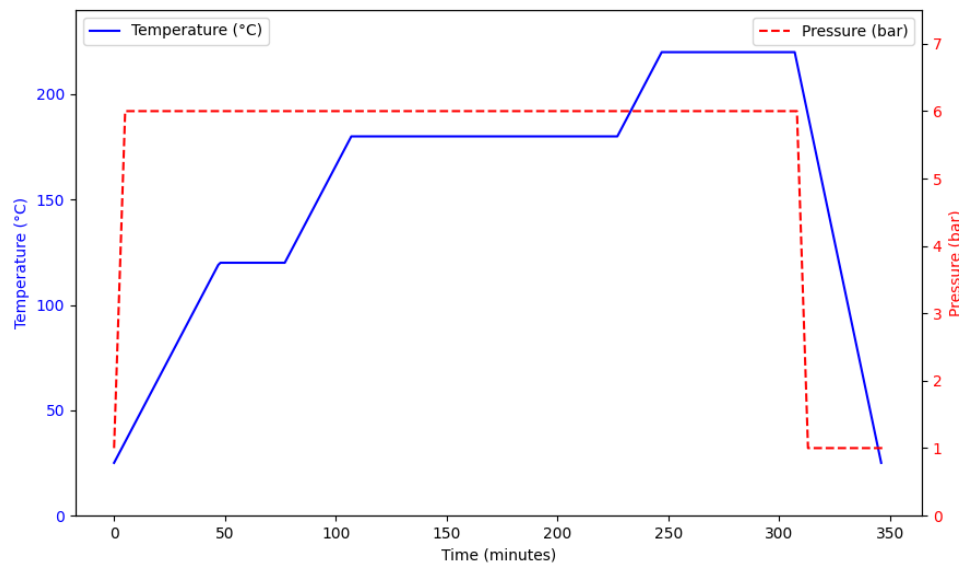


Figure 52. Autoclave curing cycle diagram

Once the curing cycle had been completed, the panel was taken out of the autoclave (See Figure 53) and demoulded (See Figure 54). Afterwards, it was necessary to cut the panel into test specimens and to perform quality control to ensure low void content had been achieved.



Figure 53. Vacuum bag after curing

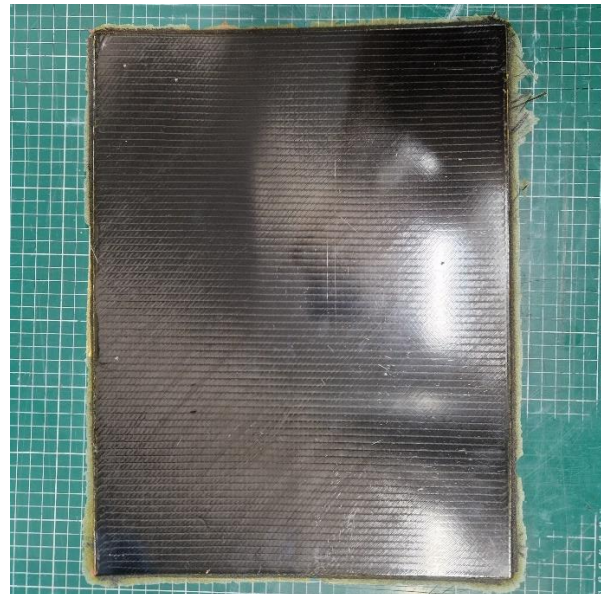


Figure 54. De-moulded composite panel

### 6.1.2. Quality Control

The quality control of the composite panel was performed in accordance with the ASTM D3171 standard which allows for the determination of constituent contents and voids in a composite piece (ASTM, 2022c). It is vital to get accurate data on the void content in the panel since it can significantly influence the outcome of future mechanical tests. Generally, higher porosity leads to increased scatter in mechanical properties, reduced fatigue resistance and greater susceptibility to environmental conditions.

The standard offers two test methods to determine the constituent contents. Test Method I (Procedure G) describes a burn-off testing method where the matrix is physically removed from the reinforcement via ignition. The fibres remain unaffected, which is a valid assumption for carbon fibres which have a significantly higher decomposition temperature than epoxy matrix. By knowing the sample masses before and after combustion, as well as the densities of fibres and the matrix, one can calculate the volume contents of each phase, including voids. Test Method II is a simpler but less accurate alternative which can only be applied when the areal density of the fabric is known. It calculates the matrix and reinforcement contents based on the measured laminate thickness. It can also determine the thickness of a cured ply but not the void content.

In total, five specimens (See Figure 55) were tested with a minimum mass of 1g, as recommended by the standard. First, the samples were tested using Test Method II due to its non-destructive nature. The thickness of each sample was determined at 10 different locations and the average value was taken for further calculations. The data obtained from each sample and the statistical summary are presented in Table 22. The samples were cut from different parts of the panel. As can be seen from the data table, there exists a noticeable variation in sample thickness ( $3.57 \pm 0.35$ mm) depending on location. In turn, this leads to varying fibre volume fractions throughout the panel. From the measurements, this variation is estimated at  $38.13 \pm 3.78\%$ . This is attributed to the fact that, at the manufacturing stage, the resin was applied unevenly on the surface of each layer. Generally, more resin was applied in the centre. The application of heat and pressure cycle in the autoclave combined with the use of a Caul plate allowed to spread of the resin more uniformly over the ply surfaces. However, it was insufficient to achieve a fully uniform thickness.

Sample #	Sample Thickness (mm)	Fibre Weight Content (%)	Fibre Volume Content (%)	Matrix Weight Content (%)	Matrix Volume Content (%)	Ply thickness (mm)
Sample 1	3.542	46.35	38.07	53.65	59.98	0.30
Sample 2	3.218	48.97	41.90	51.03	59.43	0.27
Sample 3	3.722	44.07	36.23	55.93	62.59	0.31
Sample 4	3.822	43.58	35.28	56.42	62.18	0.32
Sample 5	3.925	42.78	34.35	57.22	62.55	0.33

Table 22. Quality control data from Test Method II

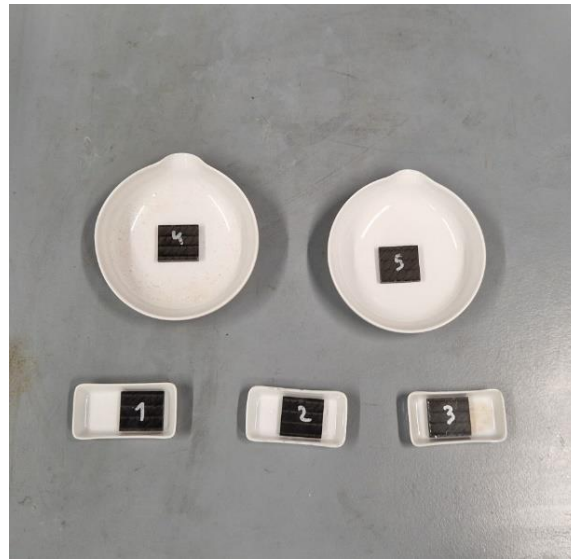


Figure 55. Quality control samples

Sample #	Fibre Weight Content (%)	Fibre Volume Content (%)	Matrix Weight Content (%)	Matrix Volume Content (%)	Void Volume Content (%)
Sample 1	41.96	34.46	58.04	64.88	0.65
Sample 2	54.12	46.30	45.88	53.43	0.27
Sample 3	43.27	35.57	56.73	63.48	0.95
Sample 4	35.76	28.95	64.24	70.79	0.25
Sample 5	34.21	27.47	65.79	71.92	0.61

Table 23. Quality control data from Test Method I

As can be seen from the data, the average fibre volume fractions from methods I and II are 35% and 37%, respectively. This is close to the values commonly used in composites designed for aerospace applications (i.e., around 40% fibre volume content). On top of that, it can be concluded that the laminate quality is sufficiently good for performing mechanical tests due to the low void volume content of around 0.55% which is significantly lower than the recommended maximums in most composite applications.

## 6.2. ILSS Testing

The Inter-Laminar Shear Strength was determined by following the ASTM D2344 test method (ASTM, 2022b). It specifies the procedure for finding the short-beam strength of a PMC. A short-beam test specimen is loaded in a 3-point bending configuration, as illustrated in Figure 56. The standard recommends a specimen thickness between 2mm and 6mm at the support span-to-thickness ratio of 4. Each test specimen rested on cylindrical supports 3mm in diameter and was loaded with a loading nose of 6mm in diameter. The tests were performed at a testing speed of 1mm/min. The specimens were cut from the panel with a 0°/90° ply orientation.

It should be noted that the standard recommends the following specimen dimensions: length = 6\*thickness, width = 2\*thickness. Initially, it was attempted to test samples with the aforementioned dimensional criteria. However, after performing more than 15 tests, it was not possible to achieve the desired failure mode. The samples experienced either diagonal shear failure or a failure mode with inelastic deformation, as presented in Figure 57. This failure mode was deemed inadequate for determining the inter-laminar shear strength because no clear mid-plane inter-laminar shear was observed. Therefore, the use of equation 27 would yield inaccurate results.

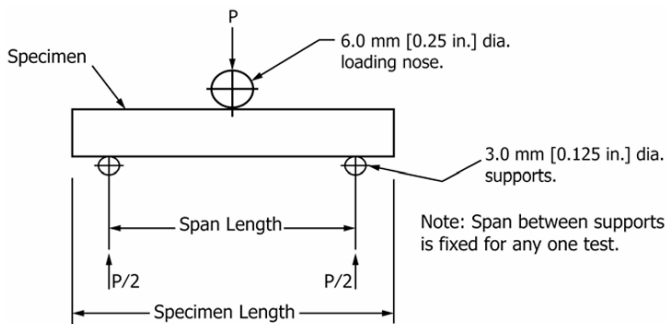


Figure 56. Short beam test configuration

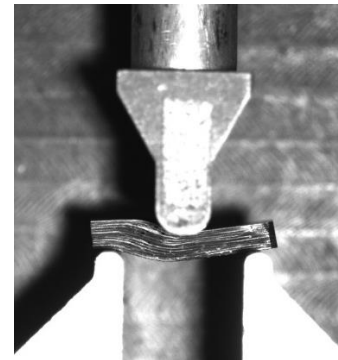


Figure 57. Invalid failure mode example

To avoid diagonal shear and inelastic failure, it was decided to increase the length of the specimens from around 21mm to 35mm. An increase in length and, consequently, the support span allowed to achieve the valid failure mode (See Figure 58) (Reed et al., 2014).

Finally, the short beam strength was calculated with the following equation:

$$F^{sbs} = 0.75 \frac{P_m}{Wt} \quad (27)$$

where  $F^{sbs}$  is equivalent to inter-laminar shear strength in MPa,  $P_m$  is the maximum force achieved during the test in N,  $W$  is the specimen width in mm, and  $t$  is the specimen thickness in mm.

The dimensions of the tested specimens alongside the computed ILSS values are presented in Table 24. Figure 59 demonstrates the load-displacement curve for the 5 tests. The average ILSS value turned out to be 30.6 MPa with a standard deviation of 1.5.

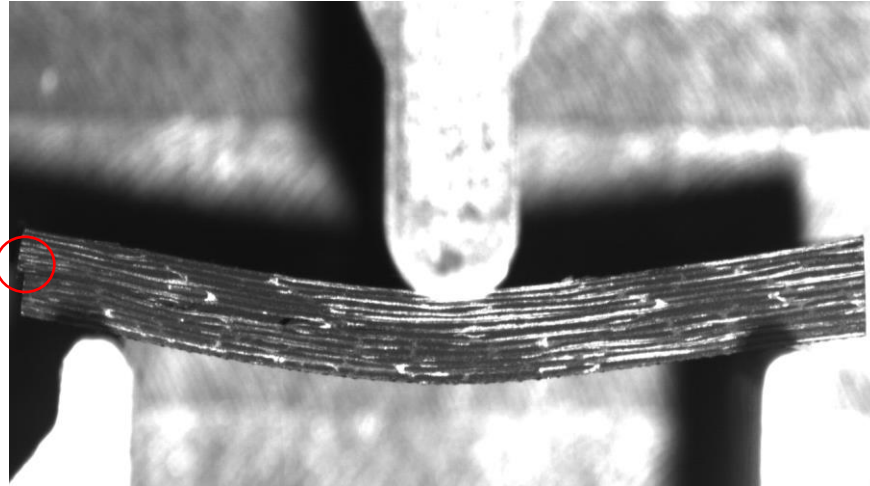


Figure 58. Mid-plane inter-laminar shear failure

Sample #	$L$ mm	$W$ mm	$t$ mm	$P_m$ N	$F^{sbs}$ MPa
Sample 1	35.34	6.08	3.77	911.86	29.8
Sample 2	35.02	7.22	3.26	993.13	31.6
Sample 3	34.96	7.34	3.74	1113.88	30.4
Sample 4	34.86	7.7	3.56	1034.85	28.3
Sample 5	35.23	7.15	3.37	1051.21	32.7

Table 24. ILSS specimen data and test results

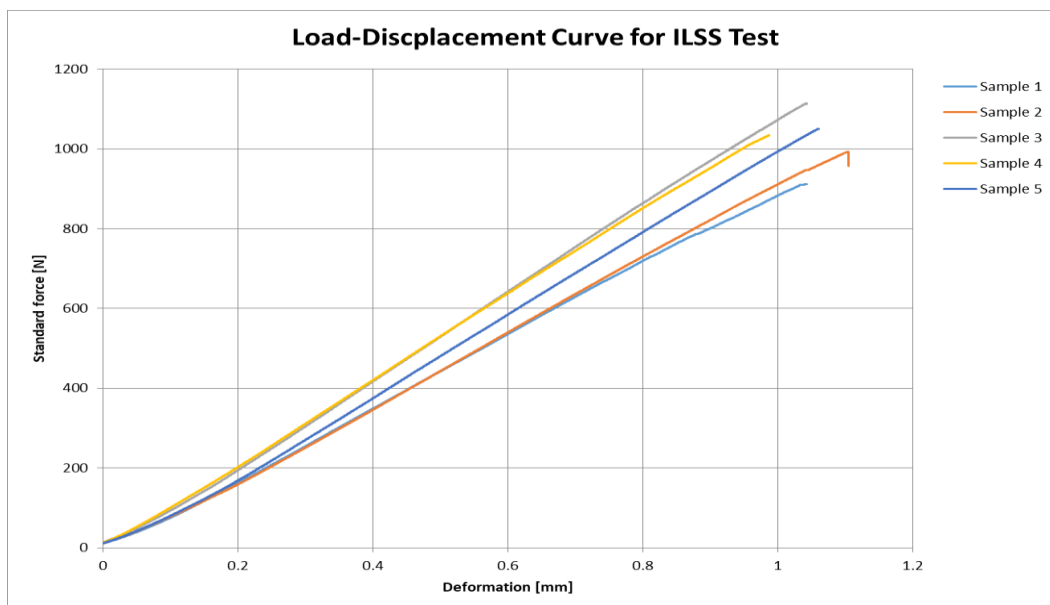


Figure 59. ILSS load-displacement curve

### 6.3. IPSS Testing

The IPSS tests were performed in accordance with the ASTM D3518 standard for the in-plane shear response of PMC composites (ASTM, 2018). The method proposes a uniaxial tension test of a composite laminate consisting of  $\pm 45^\circ$  plies (See Figure 60).

The following test sample dimensions were followed, as recommended by the standard: length – 250mm, width – 25mm. No thickness requirements were presented in the standard. However, the actual thickness of the test specimens was fixed by the composite panel. The gauge section thickness of test specimens was around  $3.38 \pm 0.33$ mm. At the same, the length of the gauge section was selected to be 50mm. The tests were performed using the Zwick Roell Universal Testing Machine. The strain data was acquired using an extensometer. The testing setup with the sample inserted in the clamps is given in Figure 61.

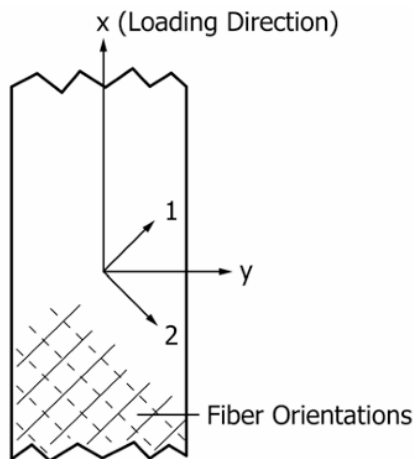


Figure 60. IPSS specimen orientation



Figure 61. IPSS test setup

The maximum shear stress developed in the laminate before failure was calculated using the following equation:

$$\tau_{12}^m = \frac{P_m}{2Wt} \quad (28)$$

where  $\tau_{12}^m$  is the maximum in-plane shear stress,  $P_m$  is the maximum force achieved during the test,  $W$  is the gauge section width, and  $t$  is the gauge section thickness.

The same equation was used to calculate the shear stress at each data point. Consequently, the chord shear modulus was determined with the following formula:

$$G^{chord} = \frac{\Delta\tau_{12}}{\Delta\gamma_{12}} \quad (29)$$

where  $G^{chord}$  is the chord shear modulus of elasticity,  $\Delta\tau_{12}$  is the difference in shear stress between two points  $\tau_1$  and  $\tau_2$ , and  $\Delta\gamma_{12}$  is the difference in shear strain between two points  $\gamma_1$  and  $\gamma_2$ .

The chord modulus was calculated using a data range of  $4000 \mu\epsilon$  and a starting point of  $1500\mu\epsilon$ . In total, 5 samples were tested. The sample dimensions, crucial test data, and computed parameters can be found in Table 25. Furthermore, Figure 62 presents the plot of shear stress vs strain for all of the specimens. The average in-plane shear strength was calculated to be 70.4 MPa with a standard deviation of 0.87. Furthermore, the in-plane shear modulus averaged at 4.45 GPa with a standard deviation of 0.66.

Sample #	$W$ mm	$t$ mm	$P_m$ N	$\tau_{12}^m$ MPa	$\gamma_1$ $\mu\epsilon$	$\gamma_2$ $\mu\epsilon$	$\tau_1$ MPa	$\tau_2$ MPa	$G^{chord}$ GPa
Sample 1	25.04	3.38	11982.3	70.8	1500	5500	9.50	24.05	3.64
Sample 2	25.19	3.7	12973.6	69.6	1500	5500	8.98	25.22	4.06
Sample 3	25.04	3.58	12621.9	70.4	1500	5500	13.20	30.44	4.31
Sample 4	24.31	3.05	10279.8	69.3	1500	5500	11.67	33.98	5.58
Sample 5	24.76	3.38	12008.6	71.7	1500	5500	10.51	29.23	4.68

Table 25. IPSS specimen data and test results

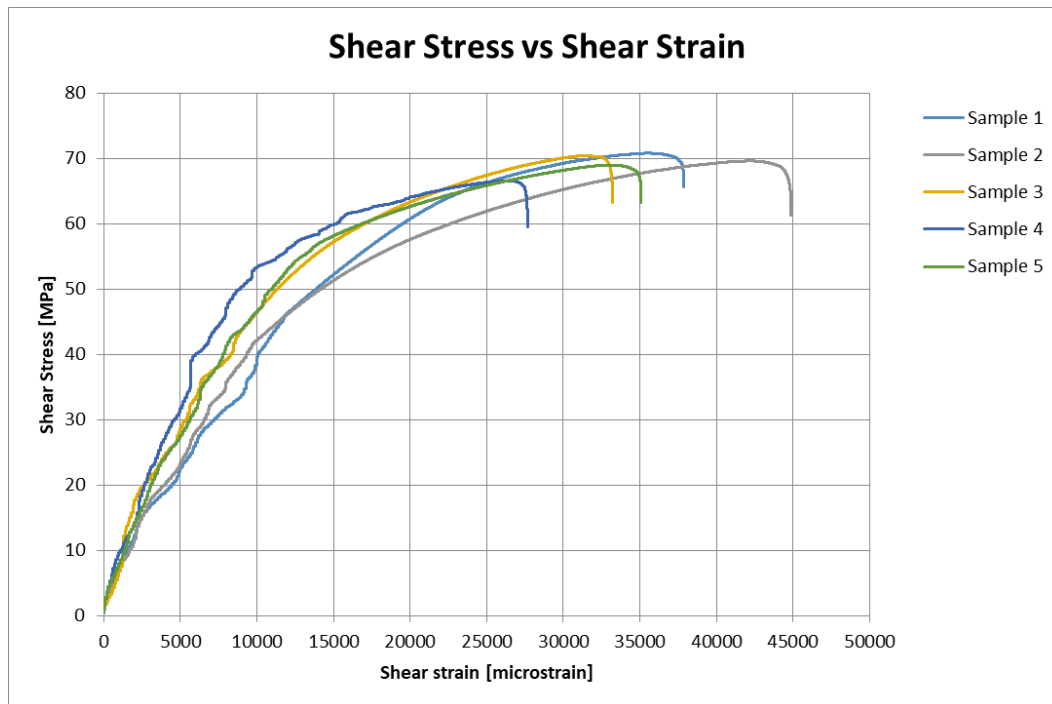


Figure 62. IPSS test stress-strain curve

## 6.4. CLC Testing

To evaluate the compressive strength and stiffness of resveratrol-based PMC, it was decided to perform a Combined Loading Compression (CLC) test. ASTM D6641 test standard for compressive properties of PMCs was used as a reference to complete the tests (ASTM, 2016). According to the standard, 5 test specimens with a 0°/90° ply orientation were prepared having a length of 140mm, width of 13mm and thickness of around 2.7±0.03mm. KFG-5-120-C1-23 uni-axial strain gauges from Kyowa were bonded to the surface of each specimen as shown in Figure 63. The gauge length of 13mm was selected to provide enough space for strain gauge installation. After placing a specimen in the CLC fixture, the strain gauge was connected to the data acquisition equipment (See Figure 64). The loading of the samples was conducted at 1.3 mm/min speed. The test outcome was considered valid if the failure had occurred in the gauge section of the specimen. Crushing of a specimen inside the grips invalidated the test results.

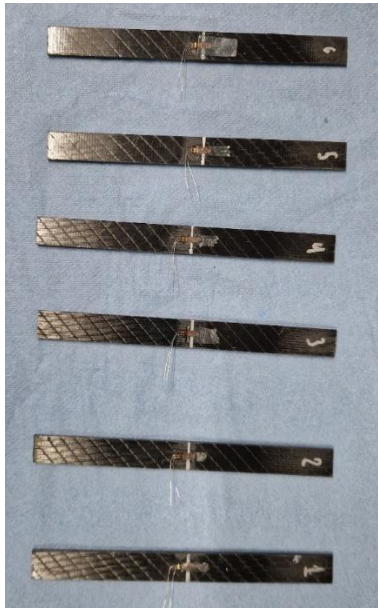


Figure 63. Prepared specimens for CLC testing

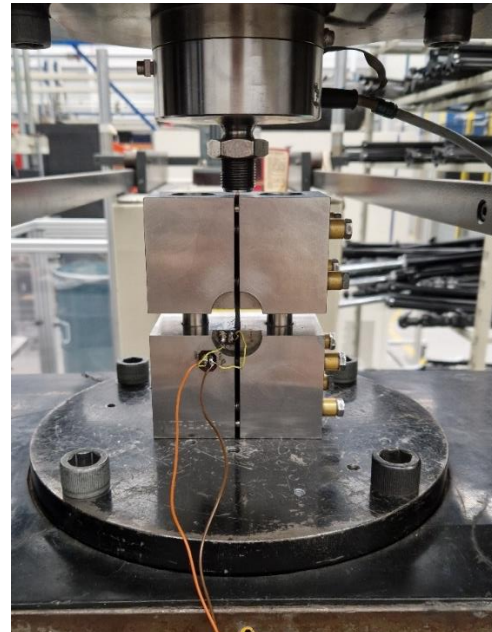


Figure 64. CLC test setup

After collecting all the data and validating the test outcomes, the compressive strength of the laminate was calculated using the following equation:

$$F^{cu} = \frac{P_f}{Wt} \quad (30)$$

Where  $F^{cu}$  is the compressive strength in MPa,  $P_f$  is the maximum load at failure in N,  $W$  is the width of the gauge section,  $t$  is the thickness of the gauge section.

Furthermore, a chord modulus was calculated over a range of axial strain of around 1800 microstrain, as per the standard. The compressive modulus was computed in the following way:

$$E_c = \frac{P_2 - P_1}{(\varepsilon_2 - \varepsilon_1)Wt} \quad (31)$$

where  $E_c$  is the compressive modulus in MPa,  $P_2$  and  $P_1$  are loads at  $\varepsilon_2$  and  $\varepsilon_1$ , respectively, while  $\varepsilon_2$  and  $\varepsilon_1$  are selected strain values near the upper and lower ends of the strain range.

Relevant sample properties and computed parameters are given in Table 26, while Figure 65 presents the force-displacement curves. Ultimately, the average compressive strength of the resveratrol-based CFRP composite was 438.6 MPa with a standard deviation of 20.6. Furthermore, the compressive modulus was estimated at 58.7 GPa having a standard deviation of 2.9.

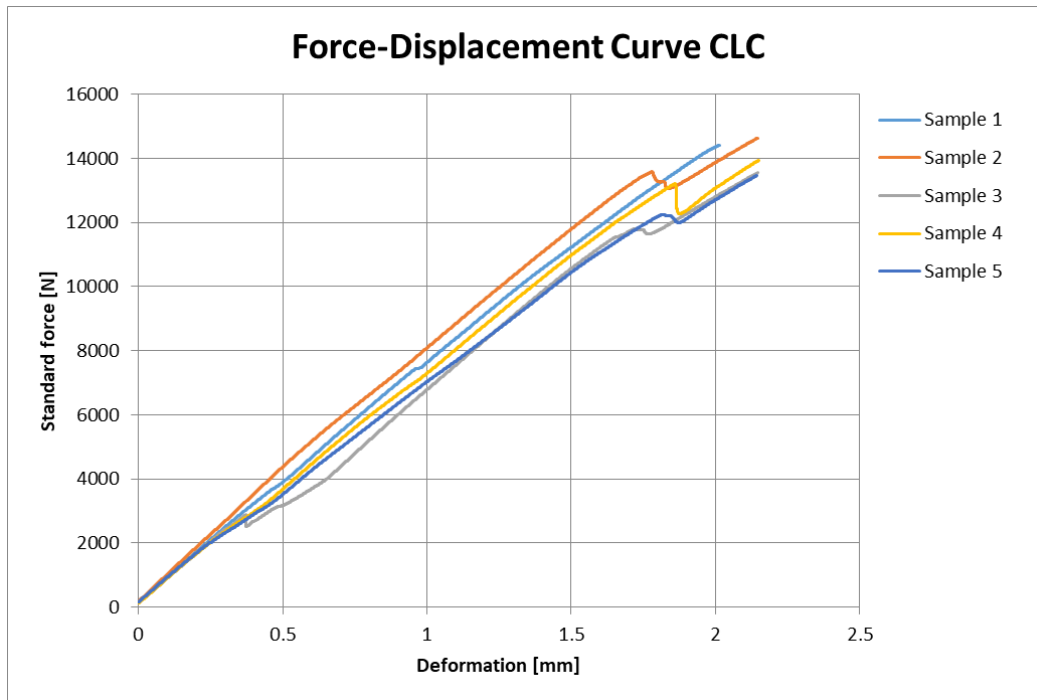


Figure 65. Compression test load-displacement curves

Sample #	$W$ mm	$t$ mm	$P_f$ N	$F^{cu}$ MPa	$\varepsilon_1$ $\mu\varepsilon$	$\varepsilon_2$ $\mu\varepsilon$	$P_1$ N	$P_2$ N	$E_c$ GPa
Sample 1	13.13	2.66	14.40	412.9	-26.03	-1504.74	153.87	3305.58	61.03
Sample 2	12.97	2.68	16.13	464.2	-24.62	-1502.43	170.82	3056.86	56.18
Sample 3	13.13	2.71	16.32	458.5	-27.60	-1502.10	144.27	3210.57	58.44
Sample 4	13.16	2.68	14.75	418.3	-24.59	-1508.53	125.32	2997.96	54.89
Sample 5	13.16	2.69	15.54	439.1	-29.33	-1507.10	159.79	3453.33	62.96

Table 26. CLC specimen data and test results

## 7. Outcomes

### 7.1. Resin Thermal & Physical Properties

Table 27 presents the summary of the main thermal properties of RTE-DDS and T742-DDS resin that were successfully investigated and compared in this study. When applicable, the acquired data is compared with the properties of other bio-based and commercial resins obtained from the literature.

	RTE-DDS	T742-DDS
Curing Cycle	C for 0.5h + 180°C for 2h + 220°C for 1h	120°C for 0.5h + 180°C for 2h + 220°C for 1h
Activation Energy	61.2 kJ/mol	66.6 kJ/mol
$T_{g\infty}$	>300°C	>300°C
Degradation Temperature		
5% mass loss	364.56°C	376.10°C
30% mass loss	403.59°C	399.48°C
Char yield @900°C	44.49%	33.30%
Storage Modulus		
@ RT	2427.8 MPa	2216.6 MPa
@ 300°C	1229.5 MPa	1091.8 MPa
Viscosity		
@ 40°C	2653 Pa*s	5441 Pa*s
@ 100°C	0.45 Pa*s	0.68 Pa*s

Table 27. Resin thermal characterisation summary

The final curing cycle of RTE-DDS resin was selected based on the data acquired from multiple DSC measurements. A cycle including a main curing step of two hours at 180°C and one hour at 220°C was chosen to achieve a reasonable degree of curing in an acceptable timeframe. In addition, a dwelling step at 120°C for 30 minutes was introduced based on the practical considerations of resin and composite sample manufacturing.

One of the reasons for the 120°C dwell step is the high viscosity of the RTE-DDS resin. While being more than two times lower than the viscosity of T742-DDS, it is significantly higher than the other commercial epoxy resins. When compared to some of the commercial resins systems that

are used in industry for wet-layup, resin transfer moulding or infusion, such as Araldite® LY 1556 / Aradur® 3405 ( $\eta$  @25°C = 1.7 Pas ), Araldite® LY 1556 / Hardener XB 3461 ( $\eta$  @25°C = 1.9 Ps) and Araldite® LY 3297 / Aradur® 3298 ( $\eta$  @25°C = 0.35 Pas) the viscosity of RTE-DDS becomes comparable only at temperatures above 80°C (Huntsman Corporation, 2010b). This complicates the processing and limits the available manufacturing options for the resin. To be able to effectively mix and degas RTE-DDS resin, it, therefore, needs to be heated up to higher temperatures. For the use in RTM where the viscosities are below 1 Pas (Liu et al., 2011), the resin needs to be heated up to over 100°C which significantly increases the energy consumption of the process as well as the equipment wear. At the same time, vacuum infusion at ambient conditions is practically impossible and is only feasible in an oven, necessitating more expensive temperature-resistant consumables. This, in turn, negates the advantages of vacuum infusion as a small-scale low-cost composite manufacturing method. Finally, the use in wet-layup is possible with preliminary heating of the resin. However, a high-temperature and pressure production method is still needed to spread the resin uniformly across the part and ensure proper fibre wetting. This can be accomplished by the use of an autoclave.

Using the data from DSC measurements and Kissinger's model, the activation energy of RTE-DDS was calculated to be 61.2 kJ/mol, 8.5% lower than for T742-DDS, indicating that a lower energy input is needed to initiate the curing reaction. The activation energy of resveratrol-based resin is also lower than that of BADGE resin (63.42 kJ/mol), resulting in a 3.6% difference. According to another study, the higher reactivity of RTE when compared to BADGE can be attributed to the more flexible molecular chain of the former. On top of that, the presence of one additional epoxy group and the conjugated stilbene structure in the RTE molecule may also lead to higher reactivity.

As a result of the high crosslinking density and, consequently, the high glass transition temperature of RTE-DDS resin, it was not possible to establish the  $T_{g\infty}$  using DSC. This was attributed to the fact that the glass transition signature of the resin was masked by the decomposition signature starting at around 300°C. Furthermore, although the use of mDSC allowed the separating of the glass transition and decomposition signals, no clear  $T_g$  the transition was recorded before 350°C. Further investigation with DMA indicated that the resin experienced vitrification during initial curing and de-vitrified during the DMA run. Signs of residual curing were observed at around 260°C - 280°C with no significant drop in storage modulus. A  $T_g$  transition occurred at around 340°C and can be taken as the  $T_{g\infty}$  of the resin. However, it does not correspond to the  $T_g$  after the defined curing cycle. As can be seen from Figure 66, RTE-DDS possesses the highest  $T_g$  among comparable RTE-based systems and significantly outperforms commercial aerospace-grade epoxies (HexFlow, 2024; TEIJIN, 2024; Westlake, 2024a, 2024b).

Using TGA analysis, the degradation of RTE-DDS resin was investigated. A mass loss of 5% was recorded at 364.56°C, marginally earlier than for T742-DDS. Despite the earlier onset of decomposition, RTE-DDS keeps more mass by the time the temperature reaches 900°C. The char yields of RTE and T742 are 44.39% and 33.30%, respectively. The formation of a char layer on the surface of the polymers is assumed to act as an insulative barrier for the combustion zone. As a result, the heat feedback is reduced, thus, preventing the formation of volatile matter (Lu et al.,

2022). The high char yield of resveratrol-based resin can serve as an indication of low flammability. In another study, TG-IR analysis showed that RTE-TAR resin loses only a small fraction of its backbone. Most of the degradation occurring is attributed to the breaking of ether bonds and detachment of oxygen atoms (Liu et al., 2023b). Furthermore, RTE-DDS possesses higher thermal resistance than other bio-based resins. Another study reported a 5% mass loss for VDE-DDS (vanillin-based) at 273°C (Kaushik, 2024), while a PHTE-DDS resin (algae-based) had a similar mass loss at 340°C (Gupta, 2024).

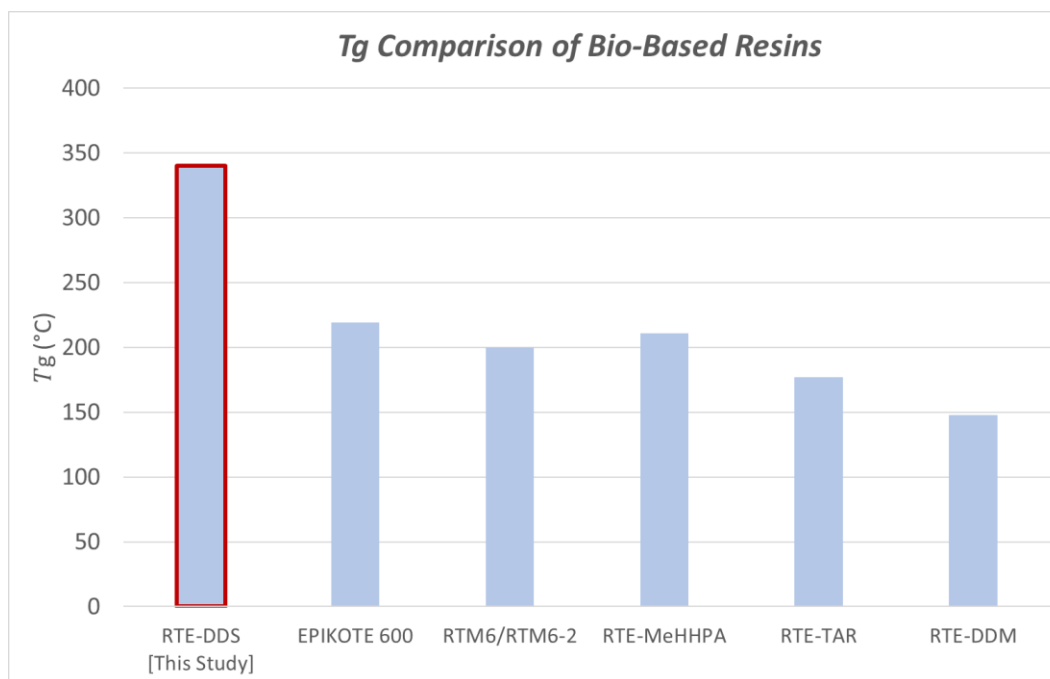


Figure 66. T<sub>g</sub> values of several resveratrol-based and commercial epoxy resins (HexFlow, 2024; Shang et al., 2018b; Tian et al., 2020; Westlake, 2024a)

Another indication of the excellent thermomechanical performance of RTE-DDS was acquired from the DMA measurements. RTE-DDS was found to have a 12% higher storage modulus at 300°C than T472-DDS. The thermal stability of RTE-DDS is superior to that of other bio-based resins. For example, a significant drop in storage modulus was observed at around 160°C for VDE-DDS (Kaushik, 2024) and at 260°C for PHTE-DDS (Gupta, 2024).

	RTE-DDS	T742-DDS
Bio-based Content	74.19%	24.81%
Density	1307.6 $\frac{kg}{m^3}$	1288.9 $\frac{kg}{m^3}$
Water Contact Angle	75.51°	71.25°
Water Absorption	1.39%	0.97%
Gel Content	99.96%	99.95%

Table 28. Resin physical characterisation summary

Table 28 presents the summary of the physical properties of RTE-DDS and T742-DDS. Since the main purpose of using resveratrol-based resin is to improve sustainability when compared to commercial resins, the bio-based content can be regarded as one of the most crucial properties in this investigation. Comparing the bio-based contents of RTE-DDS and T742-DDS (74.19% vs 24.81%), it can be concluded that the former has a less detrimental effect on the environment.

Moreover, RTE-DDS resin also possesses a water contact angle closer to 90° than T742-DDS (75.51° vs 71.25°), which indicates a more hydrophobic nature. On top of that, the water contact angle of RTE-DDS is also higher than other comparable bio-based resins, such as VDE-DDS (71°) and PHTE-DDS (69°) (Gupta, 2024; Kaushik, 2024). Furthermore, as previously stated, bio-based resins tend to absorb higher amounts of water. While it is true when comparing the water absorption of RTE-based resin (1.39%) and Tactix (0.97%), the water intake of resveratrol is comparable to PHTE-DDS (1.3%) and significantly lower than VDE (5.49%) (Gupta, 2024; Kaushik, 2024). It should also be noted that the moisture uptake of some commercial aerospace-grade epoxies, such as RTM6/RTM6-2, is in the range of 2% – 3% (HexFlow, 2024).

Finally, it was found that RTE resin has a similar but slightly higher density than T742 resin, which is expected due to their similar chemical structure. However, the difference between average densities is only marginal, 1.4%. On the other hand, RTE-DDS has a lower density than BADGE-DDS,  $1308 \frac{kg}{m^3}$  vs  $1333 \frac{kg}{m^3}$  (Gupta, 2024). Other bio-based resins may offer better specific properties due to lower densities:  $1217 \frac{kg}{m^3}$  for PHTE-DDS and  $1296 \frac{kg}{m^3}$  for VDE-DDS (Gupta, 2024; Kaushik, 2024). Generally, a higher density of bio-based resin is undesirable when taking into account aerospace applications where weight savings are essential for emission and cost reductions.

## 7.2. Resin Mechanical Properties

As part of the current study, several mechanical tests were performed on the RTE-DDS and T742-DDS resins, including tensile, flexural and fracture toughness testing. The gathered data was used to derive the mechanical properties of both resins and compare them, as can be seen from the Table 29.

	RTE-DDS	T742-DDS
Tensile Strength	43.97±3.12 MPa	63.36±10.02 MPa
Tensile Modulus	2.31±0.13 GPa	2.57±0.08 GPa
Flexural Strength	106.10±10.7 MPa	116.18±9.91 MPa
Flexural Modulus	2.96±0.12 GPa	3.35±0.08 GPa
Fracture Toughness	0.74±0.11 MPa * m <sup>0.5</sup>	0.46±0.06 MPa * m <sup>0.5</sup>

Table 29. Resin mechanical characterisation summary

As can be seen from the data, RTE resin exhibits 36% lower tensile strength, 43.97 MPa vs 63.36 MPa. Similarly, T742 has a higher tensile modulus and strain at break than the RTE counterpart, 2.57 MPa and 3.1%, respectively. This constitutes an 11% and 28% difference for each respective parameter. Similarly, T742-DDS has higher flexural strength by a marginal 1.7% and flexural modulus by 12.4%.

Furthermore, the mechanical properties of RTE-DDS and T742-DDS are put in comparison against other bio-based and commercial petroleum-based resins. Specifically, two commercial resin systems were chosen for comparison, *Araldite LY 1556 - Aradur 34055* and *Araldite LY 1568 - Aradur 3492* produced by Huntsman Corporation. The former is commonly used for manufacturing structural composites via wet lay-up and resin transfer moulding, while the latter is a low-viscosity system that can be used in wet lay-up, as well as filament winding and infusion.

Figure 67 shows that based on the gathered data, RTE-DDS possesses the lowest tensile strength out of the compared resins. The flexural strength was comparable to the other resins but was still lower than other bio-based and commercial analogues (See Figure 68). Despite lower strength, RTE-DDS resin does have a higher tensile modulus than PHTE-DDS and VDE-DDS. However, other bio-based resins possess a higher flexural modulus. Lastly, RTE-DDS resin has higher stiffness than BADGE-DDS (Gupta, 2024; Kaushik, 2024).

Initially, the low performance of RTE-DDS resin was deemed unexpected since it was assumed that the resin obtained a high cross-linking density, which is attributed to the higher reactivity of the RTE monomer when compared to other resins (higher functionality). Thus, as a result of higher functionality of the resin and a high  $T_g$  value, it was assumed that RTE would possess higher mechanical properties, particularly strength (Gradin et al., 1989).

However, while the mechanical properties of the cured epoxy depend on the cross-link density, other parameters of the cross-linked structure play a role. These parameters may include the permanent dipoles, aromatic to aliphatic atom ratio and the free volume of the polymer (Dyer et al., 2024). Moreover, the aforementioned parameters are not independent of each other and are also influenced by the cross-link density.

For example, according to McKenna (1989), it is considered that an increase in cross-link density leads to a decrease in the free volume of the polymer due to the exchange of van der Waals' bonds for shorter covalent bonds. Then, taking into account the considerations of McKenna and Gradin et al., higher cross-link density would lead to lower free volume and higher strength. Furthermore, a study by C. Li & Strachan (2016) concludes that, for the same cross-link density, a reduction of free volume leads to higher stiffness and strength.

At the same time, the effect of aromaticity on free volume is not conclusive since a higher ratio of aromatic to aliphatic atoms can both increase and decrease the free volume through different mechanisms (Dyer et al., 2024). Having said that, a higher ratio may lead to lower strength and higher stiffness of the resin.

Thus, the low flexural and tensile strength of RTE-DDS could be explained by the higher free volume of the resin. This becomes a plausible explanation after analysing the free volume data

generated by Dyer et al. (2024). According to the study, RTE-DDS has a larger free volume than both PHTE-DDS and VDE-DDS. Furthermore, RTE-DDS has a higher ratio of aromatic to aliphatic atoms than the other bio-based resins. This can explain the higher tensile modulus of RTE-based resin without contradicting the lower strength. However, the flexural modulus distribution of the resins is different from the tensile modulus. Here, PHTE- and VDE-based resins have higher values (Gupta, 2024; Kaushik, 2024).

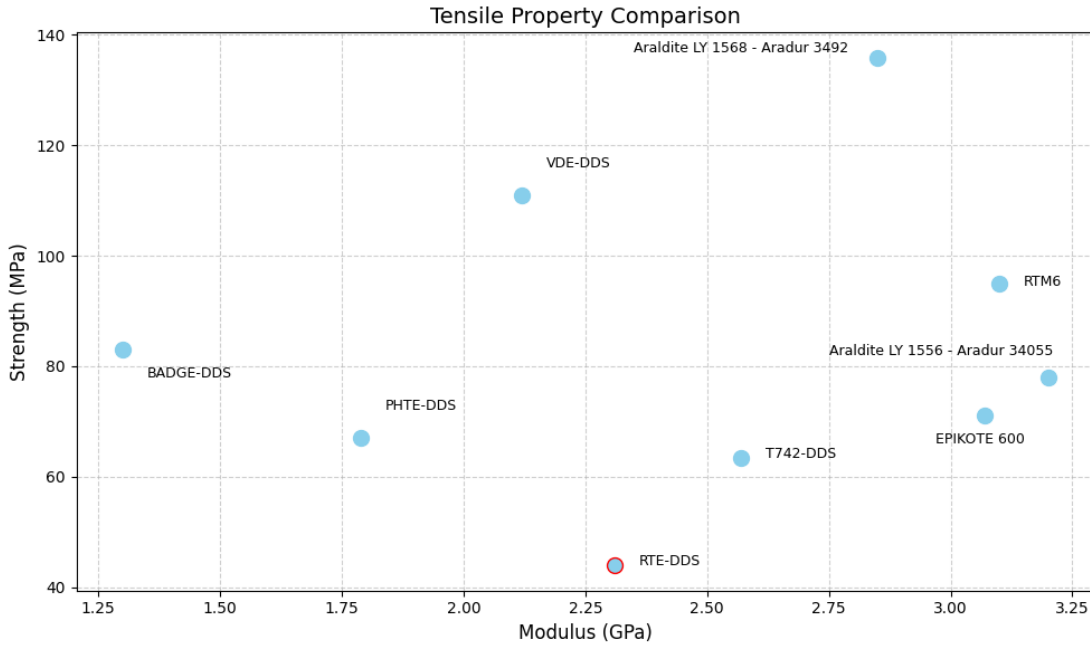


Figure 67. Tensile and flexural strengths of various epoxy resins (Gupta, 2024; Huntsman, 2010, 2012; Kaushik, 2024)

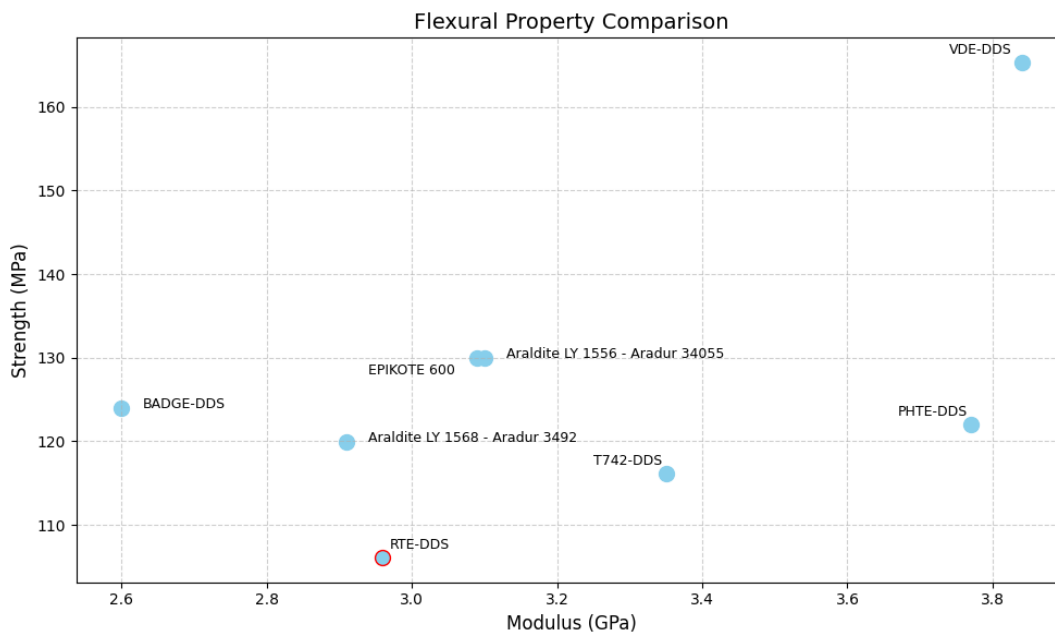


Figure 68. Tensile and flexural moduli of various epoxy resins(Gupta, 2024; Huntsman, 2010, 2012; Kaushik, 2024)

Additionally, Figure 69 shows the comparison of fracture toughness values among several bio-based and commercial epoxy resins with respect to their  $T_g$ . Here, RTE-DDS has better performance than both T742-DDS and BADGE-DDS resins. While the fracture toughness of RTE-DDS is similar to Araldite LY 1568 - Aradur 3492 and Araldite LY 1556 - Aradur 34055, its thermal performance is significantly better. Moreover, the fracture toughness of RTE-DDS is lower than that of VDE-DDS and higher than that of PHTE-DDS (Gupta, 2024; Kaushik, 2024). Finally, RTE-DDS has better fracture toughness and thermal stability than some common aerospace-grade epoxies (RTM6 and EPIKOTE 600).

Referring these results to the previous discussion on free volume, a higher free volume in a material provides additional space for molecular movement, allowing the network to adjust slightly under stress and redistribute the load more evenly. However, in terms of fracture toughness, free volume can create localised stress concentrations at the pores, acting as weak points where cracks might initiate. Consequently, an increase in free volume is generally associated with a decrease in fracture toughness due to these stress-inducing effects (Dyer et al., 2024). Thus, a higher free volume of RTE-DDS resin may lead to lower fracture toughness than VDE-DDS. Similarly, since both BADGE-DDS and T742-DDS have higher free volume, they are also more prone to crack propagation.

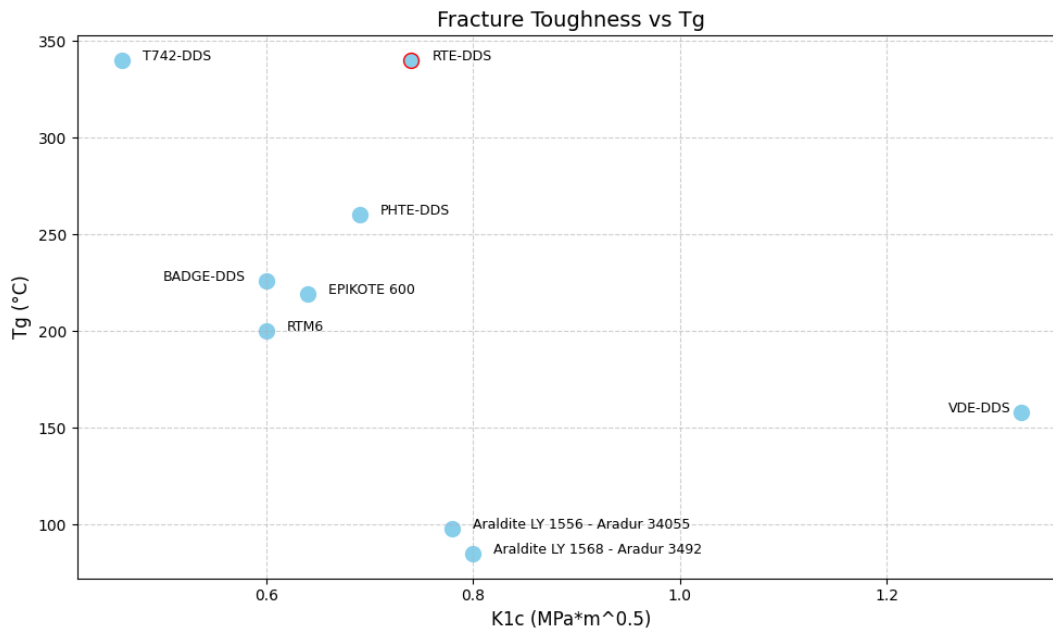


Figure 69. Fracture toughness values of various epoxy resins (Gupta, 2024; HexFlow, 2024; Kaushik, 2024; Westlake, 2024a)

In summary, a composite matrix material must have a combination of good stiffness and fracture toughness. Although RTE-DDS has lower tensile and flexural strengths than some alternatives, the combination of acceptable properties with excellent thermal stability is the quality that makes it uniquely suited for high-performance applications. Furthermore, the tensile and flexural strengths of the matrix are not as important as those of fibres, since it is the purpose of the reinforcement phase to carry the main load. In contrast, the influence of the matrix becomes more significant

when considering crack propagation during impact with foreign objects, for instance. Generally, to achieve good fracture toughness in combination with impact resistance, a resin must have sufficiently high stiffness but also be able to accommodate some deformation before failure. However, if the stiffness is too high, then the matrix may be too brittle and rapid crack propagation can be expected. In turn, this may lead to damage to the fibres and potentially catastrophic failure.

### 7.3. Composite Mechanical Properties

Table 30 contains the mechanical properties of the composite panel with RTE-DDS matrix. In total, three types of tests were performed: combined loading compression, inter-laminar shear and in-plane shear. Due to time constraints, no tests were performed with the T742-DDS as a matrix material. However, a comparison with other matrix materials is provided below.

	<b>RTE-DDS Matrix</b>
Inter-Laminar Shear Strength	30.6±1.50 MPa
In-Plane Shear Strength	70.4±0.87 MPa
Shear Modulus	4.45±0.66 GPa
Compressive Strength	438.6±20.60 MPa
Compressive Modulus	58.7±2.90 GPa

Table 30. Composite mechanical characterisation summary

As can be seen from Figure 70, the overall performance of the RTE-DDS matrix is lower than for other bio-based matrices. As such, ILSS of VDE-DDS and PHTE-DDS are respectively 62% and 68% higher than that of RTE-based resin. However, the RTE-DDS matrix composite possesses a slightly higher value of ILSS when compared to BADGE-DDS. In terms of in-plane shear and compressive strengths, the discrepancy in performance is lower but the RTE-DDS matrix still performs the worst, nevertheless.

Lastly, Figure 71 shows the shear and compressive moduli of RTE-, VDE- and BADGE-based composites. As previously, the RTE-DDS matrix has a lower performance than the other matrix materials.

To conclude, it becomes obvious from the gathered mechanical performance data that the RTE-DDS matrix offers lower shear and compressive properties than the typical petroleum-based and alternative bio-based resin formulations. However, it should be reiterated that one of the main advantages of RTE monomer is its thermal stability and unmatched mechanical performance at higher temperatures, as was demonstrated with the DMA measurements. As will be discussed in Section 8, a comparison of mechanical performance at higher temperatures is desirable to properly evaluate the potential of RTE-DDS as a matrix material for structural composites.

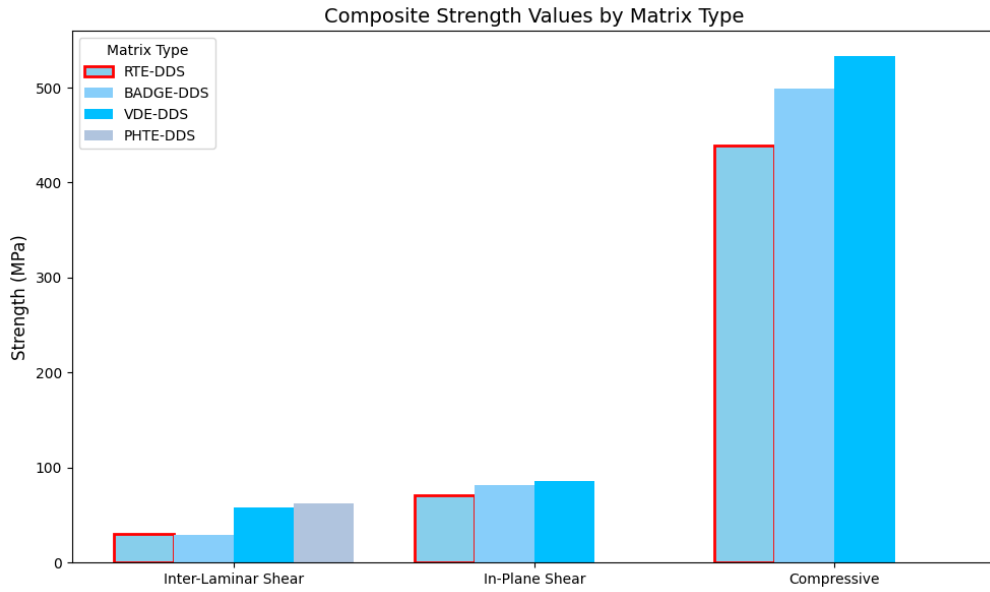


Figure 70. ILSS, IPSS and compressive strength values for different matrices

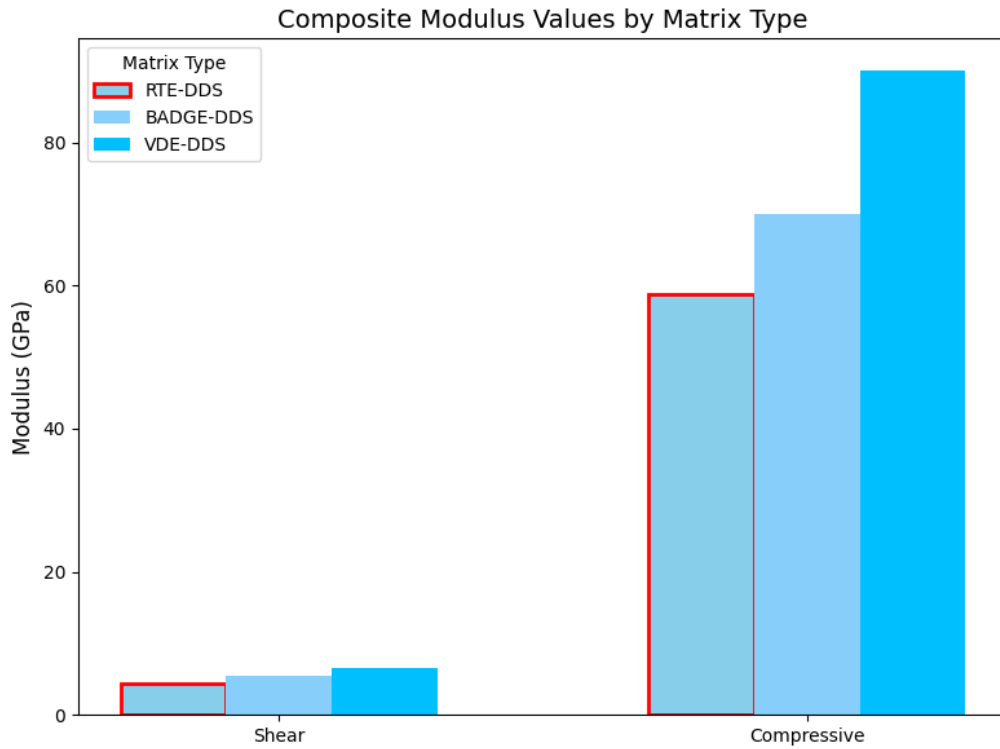


Figure 71. Shear and Compressive moduli for different matrices

## 7.4. Final Conclusions

Over the previous decades, the aviation industry has firmly established itself at the forefront of efficient technology. Initially, the drive to develop more efficient aircraft technology was governed purely by economic reasoning. However, with a projected yearly increase in demand of 4.3% over the next decades and a growing socio-political pressure to mitigate the growth of CO<sub>2</sub> emissions, the key members of the aviation sector, including airlines and aircraft manufacturers have pledged to achieve net-zero carbon emissions by 2050. As defined by the International Air Transport Association, the achievement of Fly Net Zero Commitment aims largely depends on the implementation of more efficient aircraft structural design. One of the key action points of IATA's plan revolves around the use of composite materials to improve aircraft sustainability.

The application of composite materials in aircraft design has seen increased growth in the past decade with some aircraft achieving over 50% composite structure by weight. Polymer Matrix Composites (PMCs) consisting of carbon fibre reinforcement and epoxy matrix have become the most common composite type used in aircraft structures due to their high mechanical performance, low weight and flexible processing. However, while the use of lighter and stronger materials greatly improves the efficiency of the aircraft, it is also crucial to consider the environmental impacts of the materials themselves. Specifically, the production of epoxy resin, which is present in about 90% of PMCs used in the aerospace industry, raises significant concerns related to environmental pollution. Currently, most common epoxy monomers are synthesised from petroleum-based starting materials, such as Bisphenol A and Tris(4-hydroxyphenyl)methane. Furthermore, exposure to Bisphenol A has been linked to detrimental health effects, such as fertility issues and cancer.

As a result, there has been increased interest in the potential use of bio-based epoxies as a sustainable substitute for petro-sourced polymers. However, while the existing bio-based epoxy resins may resolve some of the aforementioned issues of conventional epoxy resins, the majority of them are rendered unsuitable for aerospace composite applications due to their low thermo-mechanical performance and susceptibility to environmental conditions. To address these issues, this study investigated the potential of bio-sourced resveratrol epoxy resin as a sustainable matrix material for polymer matrix composites in aerospace applications. The research addressed key objectives: assessing the thermal, physical, and mechanical properties of resveratrol-based epoxy resins, comparing them to conventional petroleum-based counterparts, and evaluating their applicability in high-performance composite manufacturing.

The outcomes demonstrated that resveratrol epoxy resin offers significant advantages over traditional BPA-based epoxy systems. First of all, its bio-sourced nature has the potential to reduce the environmental burden of epoxy resin by mitigating the dependence on fossil fuel extraction. Furthermore, resveratrol presents a much safer alternative to the currently-used epoxy monomers, minimising the health and safety risks to people and wildlife. Most importantly, its aromatic structure imparted good thermal stability and mechanical properties, evidenced by high glass transition temperature, competitive stiffness and fracture toughness. Moreover, resveratrol-based epoxy resin demonstrated a more hydrophobic nature when compared to other bio-sourced resins,

thusby circumventing one of the main challenges of bio-materials in aerospace applications. From a manufacturing perspective, resveratrol-based composites showed compatibility with existing production processes, such as wet lay-up and autoclave curing. The resin's processability and curing behaviour were investigated through rheological studies and differential scanning calorimetry.

Some challenges arose during the investigation. Firstly, the high cross-link density of the resin complicated the accurate measurement of the glass transition temperature with the available methods. Although the ultimate glass transition temperature could be estimated with DMA, some indications of residual curing were observed in the resin prior to that, indicating possible vitrification of the original cured system. Furthermore, the high viscosity of the resin posed a serious challenge during wet lay-up, complicating the homogeneous application of the resin and leading to non-uniform composite panel thickness. Finally, composite testing indicated lower mechanical properties than other bio-based resins, which can be partially attributed to manufacturing-related issues and the chemical nature of the resveratrol structure.

In conclusion, this study underscores the feasibility of using resveratrol epoxy resin as a viable alternative to petroleum-based epoxies while still offering excellent thermal and mechanical performance. By addressing the dual imperatives of performance and eco-efficiency, resveratrol epoxy holds the potential to greatly improve the sustainability of aircraft design bringing the aviation sector one step closer to net-zero operations. Nevertheless, some challenges and benefits of resveratrol epoxy remain to be studied.

## 8. Recommendations for Future Work

As concluded in the previous chapter, RTE holds great potential as an alternative to existing petroleum-based epoxy monomers in high-performance composite manufacturing. While the current study has successfully revealed and characterised some thermomechanical properties of RTE, it has also uncovered some challenges and points of interest that require further research, such as:

1. **High viscosity of RTE resin system:** As was discovered in this study, RTE monomer is characterised by a high viscosity at room temperature. As a result, high temperatures of around 100°C were required to achieve convenient processing. Even then, the manufacturing of composite laminates using wet lay-up was complicated leading to an imperfect final product with thickness variation throughout the composite panel. To improve the processing of the resin, the incorporation of reactive diluents should be considered and the influence on mechanical and thermal properties investigated.
2. **Further Cure Kinetics Characterisation of RTE resin system:** As was discussed earlier, it was problematic to define the  $T_g$  of the RTE-DDS system. While the  $T_{g\infty}$  was successfully defined, further investigation of the  $T_g$  progression with cure is required for successful industrial applications which can be attempted by applying the DiBenedetto equation. The creation of a Time-Temperature-Transformation (TTT) diagram is also crucial for optimisation of the curing cycle. Finally, the presence of vitrification was established in the study which needs to be further investigated.
3. **Flame resistance of RTE resin system:** The current study has revealed the great thermomechanical performance of RTE monomers in epoxies. High  $T_g$  coupled with excellent temperature resistance indicate the potential of RTE-DDS epoxy as a flame-retardant material. Further investigations can include the UL 94 flammability test and LOI (Limiting Oxygen Index) Test to determine minimum oxygen concentration for sustained combustion.
4. **Life Cycle Assessment (LCA) of RTE resin system:** While extensive analyses of mechanical and thermal properties have been conducted, particularly with claims that RTE is bio-based, it is crucial to carefully evaluate the true impact of green materials. LCA studies provide a reliable framework for assessing the overall changes or impacts associated with a process or material, helping to prevent greenwashing based solely on the material's bio-based nature. In some cases, bio-based materials may require more intensive processing, potentially resulting in a net negative environmental effect.
5. **High cost and food security:** Lastly, two of the challenges of bio-based epoxies are presented in Section 3.5.2 are still significant concerns for the use of RTE on an industrial scale. With the current price of the monomer at around 600 euros per 100g, it is crucial to investigate possible paths for cost reduction. On top of that, while the resveratrol used in this study had been obtained from Japanese knotweed (an invasive species), the bio-sourced resveratrol may come from agricultural products used for food production, such as grapes. Thus, it is important to model the influence of resveratrol production on food security in vulnerable areas.

## References

1. AGC Chemicals. (2024). *EPINITY™ Bio-based Epichlorohydrin*. <https://agcce.com/products/epinity-bio-based-epichlorohydrin/>
2. Alleman, G. (2018). *The effects of different cure cycles on the mechanical performance of thick-walled composites*.
3. Amarasekara, A. S., Garcia-Obergon, R., & Thompson, A. K. (2019). Vanillin-based polymers: IV. Hydrovanilloin epoxy resins. *Journal of Applied Polymer Science*, 136(4). <https://doi.org/10.1002/app.47000>
4. Anton Paar. (2017). *Basics of rheology*. <https://wiki.anton-paar.com/nl-en/basics-of-rheology/>
5. Apostolidis, D., Dyer, W. E., Dransfeld, C. A., & Kumru, B. (2024). An algae-derived partially renewable epoxy resin formulation for glass fibre-reinforced sustainable polymer composites. *RSC Applied Polymers*, 2(2), 149–154. <https://doi.org/10.1039/d3lp00174a>
6. ASTM. (2010). *ASTM D790 Test Methods for Flexural Properties of Unreinforced and Reinforced Plastics and Electrical Insulating Materials*. ASTM International. <https://doi.org/10.1520/D0790-10>
7. ASTM. (2014). *ASTM D638 Test Method for Tensile Properties of Plastics*. ASTM International. <https://doi.org/10.1520/D0638-14>
8. ASTM. (2016). *ASTM D6641 Test Method for Compressive Properties of Polymer Matrix Composite Materials Using a Combined Loading Compression (CLC) Test Fixture*. ASTM International. [https://doi.org/10.1520/D6641\\_D6641M-16E02](https://doi.org/10.1520/D6641_D6641M-16E02)
9. ASTM. (2018). *ASTM D3518 Test Method for In-Plane Shear Response of Polymer Matrix Composite Materials by Tensile Test of a 45 Laminate*. ASTM International. [https://doi.org/10.1520/D3518\\_D3518M-18](https://doi.org/10.1520/D3518_D3518M-18)
10. ASTM. (2019). *ASTM D5045 Standard Test Methods for Plane-Strain Fracture Toughness and Strain Energy Release Rate of Plastic Materials*. [www.astm.org](http://www.astm.org)
11. ASTM. (2020). *ASTMD792 Test Methods for Density and Specific Gravity (Relative Density) of Plastics by Displacement*. ASTM International. <https://doi.org/10.1520/D0792-20>
12. ASTM. (2021). *ASTM D3418 Test Method for Transition Temperatures and Enthalpies of Fusion and Crystallization of Polymers by Differential Scanning Calorimetry*. ASTM International. <https://doi.org/10.1520/D3418-21>
13. ASTM. (2022a). *ASTM D570 Test Method for Water Absorption of Plastics*. ASTM International. <https://doi.org/10.1520/D0570-22>
14. ASTM. (2022b). *ASTM D2344 Test Method for Short-Beam Strength of Polymer Matrix Composite Materials and Their Laminates*. ASTM International. [https://doi.org/10.1520/D2344\\_D2344M-22](https://doi.org/10.1520/D2344_D2344M-22)
15. ASTM. (2022c). *ASTM D3171 Test Methods for Constituent Content of Composite Materials*. ASTM International. <https://doi.org/10.1520/D3171-22>
16. ASTM. (2022d). *Test Method for Short-Beam Strength of Polymer Matrix Composite Materials and Their Laminates*. ASTM International. [https://doi.org/10.1520/D2344\\_D2344M-22](https://doi.org/10.1520/D2344_D2344M-22)
17. ASTM. (2024). *D2765 Standard Test Methods for Determination of Gel Content and Swell Ratio of Crosslinked Ethylene Plastics*. <https://www.astm.org/d2765-16.html>

18. Auvergne, R., Caillol, S., David, G., Boutevin, B., & Pascault, J. P. (2014). Biobased thermosetting epoxy: Present and future. In *Chemical Reviews* (Vol. 114, Issue 2, pp. 1082–1115). <https://doi.org/10.1021/cr3001274>
19. Bu, M., Zhang, X., Zhou, T., & Lei, C. (2022). Fully bio-based epoxy resins derived from magnolol and varying furan amines: Cure kinetics, superior mechanical and thermal properties. *European Polymer Journal*, 180. <https://doi.org/10.1016/j.eurpolymj.2022.111595>
20. Callister, William D., J., & Rethwisch, D. G. (2018a). Materials Science and Engineering: An Introduction. *Materials Science and Engineering: An Introduction*, 754. <https://www.wiley.com/en-us/Materials+Science+and+Engineering%3A+An+Introduction%2C+10th+Edition-p-9781119405498>
21. Callister, William D., J., & Rethwisch, D. G. (2018b). Materials Science and Engineering: An Introduction. *Materials Science and Engineering: An Introduction*, 754. <https://www.wiley.com/en-us/Materials+Science+and+Engineering%3A+An+Introduction%2C+10th+Edition-p-9781119405498>
22. CAMEO Chemicals. (2010). 4,4'-DIAMINODIPHENYLMETHANE. <https://cameochemicals.noaa.gov/chemical/3080>
23. Capretti, M., Giammaria, V., Santulli, C., Boria, S., & Del Bianco, G. (2023). Use of Bio-Epoxyes and Their Effect on the Performance of Polymer Composites: A Critical Review. In *Polymers* (Vol. 15, Issue 24). Multidisciplinary Digital Publishing Institute (MDPI). <https://doi.org/10.3390/polym15244733>
24. CCUK. (2022). *Is Carbon Fibre a Sustainable Material for Strengthening Buildings and Structures?* <https://www.fibrwrap-ccuk.com/carbon-fibre-strengthening/is-carbon-fibre-a-sustainable-material-for-strengthening-buildings-and-structures/>
25. CDC. (2024). Acrylonitrile. <https://archive.cdc.gov/#/details?url=https://www.cdc.gov/niosh/topics/acrylonitrile/default.html>
26. Chandekar, H., Chaudhari, V., & Waigaonkar, S. (2020). A review of jute fiber reinforced polymer composites. *Materials Today: Proceedings*, 26, 2079–2082. <https://doi.org/10.1016/j.matpr.2020.02.449>
27. Chou, T.-W. (1992). *Microstructural Design of Fiber Composites*. <https://doi.org/10.1017/CBO9780511600272>
28. Davé, R. S. ., & Loos, A. C. . (2000a). *Processing of composites*. Hanser Publishers ; Hanser/Gardner Publications.
29. Davé, R. S. ., & Loos, A. C. . (2000b). *Processing of composites*. Hanser Publishers ; Hanser/Gardner Publications.
30. Dvorakova, M., & Landa, P. (2017). Anti-inflammatory activity of natural stilbenoids: A review. *Pharmacological Research*, 124, 126–145. <https://doi.org/10.1016/J.PHRS.2017.08.002>
31. Dyer, Schut, H., Dransfeld, C. A., & Kumru, B. (2024). *Bio-Based Epoxyes: Mechanical Properties And Free Volume Perspectives* (Vol. 1).

32. Dyer, W. E., & Kumru, B. (2023). Polymers as Aerospace Structural Components: How to Reach Sustainability? In *Macromolecular Chemistry and Physics* (Vol. 224, Issue 24). John Wiley and Sons Inc. <https://doi.org/10.1002/macp.202300186>
33. EAG Laboratories. (2020). *DSC Analysis of Polymers*. <https://www.eag.com/app-note/characterization-of-polymers-using-differential-scanning-calorimetry-dsc/>
34. ECHA. (2023). *Substance Information - 4,4'-methylenedianiline*. <https://echa.europa.eu/substance-information/-/substanceinfo/100.002.705>
35. ECHA. (2024). *4,4'-isopropylidenediphenol*. <https://echa.europa.eu/brief-profile/-/briefprofile/100.001.133>
36. EEA. (2023a). *Human exposure to Bisphenol A in Europe*. <https://www.eea.europa.eu/publications/peoples-exposure-to-bisphenol-a/>
37. EEA. (2023b). *Human exposure to Bisphenol A in Europe*. <https://www.eea.europa.eu/publications/peoples-exposure-to-bisphenol-a/>
38. EFSA. (2023). *Bisphenol A*. <https://www.efsa.europa.eu/en/topics/topic/bisphenol>
39. Faserverbundwerkstoffe GmbH. (2024). *Carbon non-crimp fabric 200 g/m<sup>2</sup> (biaxial) 125 cm*. <https://www.r-g.de/en/art/CT-200125-BA>
40. Fink, J. K. (2013). Epoxy Resins. In *Reactive Polymers Fundamentals and Applications* (pp. 95–153). Elsevier. <https://doi.org/10.1016/B978-1-4557-3149-7.00003-6>
41. Foreman, J., Sauerbrunn, S. R., & Marcozzi, C. L. (2010). *Exploring the Sensitivity of Thermal Analysis Techniques to the Glass Transition Thermal Analysis & Rheology*.
42. Garrison, M. D., Savolainen, M. A., Chafin, A. P., Baca, J. E., Bons, A. M., & Harvey, B. G. (2020). Synthesis and Characterization of High-Performance, Bio-Based Epoxy-Amine Networks Derived from Resveratrol. *ACS Sustainable Chemistry and Engineering*, 8(37), 14137–14149. <https://doi.org/10.1021/acssuschemeng.0c04816>
43. Gradin, P., Howgate, P. G., Seldén, R., & Brown, R. A. (1989). Dynamic-mechanical Properties. *Comprehensive Polymer Science and Supplements*, 533–569. <https://doi.org/10.1016/B978-0-08-096701-1.00053-7>
44. Gupta, P. (2024). *Naturally Sourced Epoxies for High-Performance Composite Applications A feasibility study of renewable algae-derived epoxy resin system*. <http://repository.tudelft.nl/>
45. Halls, C., & Yu, O. (2008). Potential for metabolic engineering of resveratrol biosynthesis. *Trends in Biotechnology*, 26(2), 77–81. <https://doi.org/10.1016/J.TIBTECH.2007.11.002>
46. Hamerton, I., & Mooring, L. (2012). *The use of thermosets in aerospace applications*.
47. Hardis, R., Jessop, J. L. P., Peters, F. E., & Kessler, M. R. (2013). Cure kinetics characterization and monitoring of an epoxy resin using DSC, Raman spectroscopy, and DEA. *Composites Part A: Applied Science and Manufacturing*, 49, 100–108. <https://doi.org/10.1016/j.compositesa.2013.01.021>
48. Hasan, K. M. F., Hasan, K. N. Al, Ahmed, T., György, S. T., Pervez, M. N., Bejó, L., Sándor, B., & Alpár, T. (2023). Sustainable bamboo fiber reinforced polymeric composites for structural applications: A mini review of recent advances and future prospects. *Case Studies in Chemical and Environmental Engineering*, 8. <https://doi.org/10.1016/j.cscee.2023.100362>
49. HexFlow. (2024). *RTM6/RTM6-2 Epoxy Datasheet*.

50. Hitachi. (2022). *Principle of Differential Scanning Calorimetry (DSC)*. <https://www.hitachi-hightech.com/global/en/knowledge/analytical-systems/thermal-analysis/basics/dsc.html>
51. Hu, Y., Tong, S., Sha, Y., Yu, J., Hu, L., Huang, Q., Jia, P., & Zhou, Y. (2023). Cardanol-based epoxy vitrimer/carbon fiber composites with integrated mechanical, self-healing, reprocessible, and welding properties and degradability. *Chemical Engineering Journal*, 471. <https://doi.org/10.1016/j.cej.2023.144633>
52. Huang, X., Liu, H., Shang, S., Cai, Z., Song, J., & Song, Z. (2016). Synthesis and characterization of castor oil-based polymeric surfactants. *Frontiers of Agricultural Science and Engineering*, 3(1), 46–54. <https://doi.org/10.15302/J-FASE-2016083>
53. Hughes, J., & Than Tun, S. (2019). *Epoxy resin composition, prepreg, and fiber reinforced composite material*.
54. Huntsman. (2010). *Advanced Materials Araldite® LY 1568 Aradur® 3489 / Aradur® 3492 STRUCTURAL COMPOSITES*.
55. Huntsman. (2012). *Advanced Materials Araldite® LY 1556 / Aradur® 34055 WARM CURING EPOXY SYSTEM Araldite® LY 1556 epoxy resin Aradur® 34055 amine hardener*.
56. Huntsman Corporation. (2010a). *ARADUR HT 976-2 CS Safety Datasheet*.
57. Huntsman Corporation. (2010b). *Composite Resin Systems Selector Guide*. [www.huntsman.com/advanced\\_materials](http://www.huntsman.com/advanced_materials)
58. Huntsman Corporation. (2012). *Tactix® 742 Epoxy resin*. <https://adhesives.specialchem.com/product/p-huntsman-tactix-742>
59. IATA. (2021a). *Aircraft Technology - Net Zero Roadmap*. [www.aviationbenefits.org](http://www.aviationbenefits.org)
60. IATA. (2021b). *Executive Summary Net Zero Roadmaps*.
61. IATA. (2021c). *Fly Net Zero*. <https://www.iata.org/en/programs/sustainability/flynetzero/>
62. IATA. (2021d). *Net Zero Roadmaps*. <https://www.iata.org/en/programs/sustainability/roadmaps/>
63. ICAO. (2024). *Future of Aviation*. <https://www.icao.int/Meetings/FutureOfAviation/Pages/default.aspx>
64. IEA. (2022). *Tracking Aviation*. <https://www.iea.org/energy-system/transport/aviation>
65. Jaillet, F., Darroman, E., Ratsimihety, A., Auvergne, R., Boutevin, B., & Caillol, S. (2014). New biobased epoxy materials from cardanol. *European Journal of Lipid Science and Technology*, 116(1), 63–73. <https://doi.org/10.1002/ejlt.201300193>
66. Javdanitehran, M., Berg, D. C., Duemichen, E., & Ziegmann, G. (2016). An iterative approach for isothermal curing kinetics modelling of an epoxy resin system. *Thermochimica Acta*, 623, 72–79. <https://doi.org/10.1016/J.TCA.2015.11.014>
67. Jeandet, P., Clément, C., & Courot, E. (2014). Resveratrol production at large scale using plant cell suspensions. *Engineering in Life Sciences*, 14(6), 622–632. <https://doi.org/10.1002/ELSC.201400022>
68. Kadam, A., Pawar, M., Yemul, O., Thamke, V., & Kodam, K. (2015). Biodegradable biobased epoxy resin from karanja oil. *Polymer*, 72, 82–92. <https://doi.org/10.1016/j.polymer.2015.07.002>
69. Kaltenecker-Uray, A., Rieß, G., Lucyshyn, T., Holzer, C., & Kern, W. (2019). Physical foaming and crosslinking of polyethylene with modified talcum. *Polymers*, 11(9). <https://doi.org/10.3390/polym11091472>

70. Kaushik, B. (2024). *Investigation of Vanillin-Derived Bio-Based Epoxy as a High-Performance Composite Matrix Material*. <http://repository.tudelft.nl/>.
71. Khusiafan, F. J. (2018). Use of KEVLAR® 49 in Aircraft Components. *Engineering Management Research*, 7(2), 14. <https://doi.org/10.5539/emr.v7n2p14>
72. Kissinger, H. E. (1957). Reaction Kinetics in Differential Thermal Analysis. *Analytical Chemistry*, 29(11), 1702–1706. [https://doi.org/10.1021/AC60131A045/ASSET/AC60131A045.FP.PNG\\_V03](https://doi.org/10.1021/AC60131A045/ASSET/AC60131A045.FP.PNG_V03)
73. Kumar, S., Krishnan, S., Mohanty, S., & Nayak, S. K. (2018). Synthesis and characterization of petroleum and biobased epoxy resins: a review. In *Polymer International* (Vol. 67, Issue 7, pp. 815–839). John Wiley and Sons Ltd. <https://doi.org/10.1002/pi.5575>
74. Kusuma, H. S., Permatasari, D., Umar, W. K., & Sharma, S. K. (2023). Sugarcane bagasse as an environmentally friendly composite material to face the sustainable development era. In *Biomass Conversion and Biorefinery*. Springer Science and Business Media Deutschland GmbH. <https://doi.org/10.1007/s13399-023-03764-2>
75. Li, C., & Strachan, A. (2016). Free volume evolution in the process of epoxy curing and its effect on mechanical properties. *Polymer*, 97, 456–464. <https://doi.org/10.1016/J.POLYMER.2016.05.059>
76. Li, T., Liu, X., Jiang, Y., Ma, S., & Zhu, J. (2016). Bio-based shape memory epoxy resin synthesized from rosin acid. *Iranian Polymer Journal (English Edition)*, 25(11), 957–965. <https://doi.org/10.1007/s13726-016-0482-0>
77. LibreTexts. (2024). *Bisphenol A*. [https://chem.libretexts.org/Ancillary\\_Materials/Exemplars\\_and\\_Case\\_Studies/Exemplars/Environmental\\_and\\_Green\\_chemistry/Bisphenol\\_A](https://chem.libretexts.org/Ancillary_Materials/Exemplars_and_Case_Studies/Exemplars/Environmental_and_Green_chemistry/Bisphenol_A)
78. Liu, J., Agag, T., & Ishida, H. (2011). Main-chain type benzoxazine oligomers: A new concept for easy processable high performance polybenzoxazines. In *Handbook of Benzoxazine Resins* (pp. 355–362). Elsevier. <https://doi.org/10.1016/B978-0-444-53790-4.00063-1>
79. Liu, J., Liu, X., Cui, X., Qin, J., Wu, M., Fu, L., Shi, M., Wang, D., & Liang, L. (2023a). Investigation on the properties and structures of resveratrol-derived epoxy thermosets cured with an active ester. *Polymer Chemistry*, 14(14), 1665–1679. <https://doi.org/10.1039/d2py01579j>
80. Liu, J., Liu, X., Cui, X., Qin, J., Wu, M., Fu, L., Shi, M., Wang, D., & Liang, L. (2023b). Investigation on the properties and structures of resveratrol-derived epoxy thermosets cured with an active ester. *Polymer Chemistry*, 14(14), 1665–1679. <https://doi.org/10.1039/d2py01579j>
81. Liu, J., Zhang, L., Shun, W., Dai, J., Peng, Y., & Liu, X. (2021). Recent development on bio-based thermosetting resins. In *Journal of Polymer Science* (Vol. 59, Issue 14, pp. 1474–1490). John Wiley and Sons Inc. <https://doi.org/10.1002/pol.20210328>
82. Lu, C., Bian, S., Hu, K., Li, C., Zheng, K., & Sun, Q. (2022). Biomass-based epoxy resin derived from resveratrol with high temperature resistance and intrinsic flame retardant properties. *Industrial Crops and Products*, 187. <https://doi.org/10.1016/j.indcrop.2022.115500>

83. Ma, C., & Li, J. (2019). Synthesis of an organophosphorus flame retardant derived from daidzein and its application in epoxy resin. *Composites Part B: Engineering*, 178. <https://doi.org/10.1016/j.compositesb.2019.107471>
84. Maiti, S., Islam, M. R., Uddin, M. A., Afroj, S., Eichhorn, S. J., & Karim, N. (2022). Sustainable Fiber-Reinforced Composites: A Review. In *Advanced Sustainable Systems* (Vol. 6, Issue 11). John Wiley and Sons Inc. <https://doi.org/10.1002/adsu.202200258>
85. Mallick, P. K. (2017a). *Processing of Polymer Matrix Composites*. <http://taylorandfrancis.com>
86. Mallick, P. K. (2017b). *Processing of Polymer Matrix Composites*. <http://taylorandfrancis.com>
87. Mallick, P. K. (2017c). *Processing of Polymer Matrix Composites*. <http://taylorandfrancis.com>
88. Matikas, T. E. (2007). ANALYSIS OF LOAD TRANSFER BEHAVIOUR AND DETERMINATION OF INTERFACIAL SHEAR STRENGTH IN SINGLE-FIBRE-REINFORCED TITANIUM ALLOYS. In *Advanced Composites Letters* (Vol. 16, Issue 5).
89. McKenna, G. B. (1989). Glass Formation and Glassy Behavior. *Comprehensive Polymer Science and Supplements*, 311–362. <https://doi.org/10.1016/B978-0-08-096701-1.00047-1>
90. More, A. P. (2022). Flax fiber–based polymer composites: a review. In *Advanced Composites and Hybrid Materials* (Vol. 5, Issue 1). Springer Science and Business Media B.V. <https://doi.org/10.1007/s42114-021-00246-9>
91. Muthu, S. S. (2020). Ways of measuring the environmental impact of textile processing: an overview. In *Assessing the Environmental Impact of Textiles and the Clothing Supply Chain* (pp. 33–56). Elsevier. <https://doi.org/10.1016/b978-0-12-819783-7.00002-8>
92. Nabipour, H., Niu, H., Wang, X., Batool, S., & Hu, Y. (2021). Fully bio-based epoxy resin derived from vanillin with flame retardancy and degradability. *Reactive and Functional Polymers*, 168. <https://doi.org/10.1016/j.reactfunctpolym.2021.105034>
93. Nepomuceno, N. C., Fook, M. V. L., Ries, A., Mija, A., & Wellen, R. M. R. (2023). Bio-Based Epoxy Resins of Epoxidized Soybean oil Cured with Salicylic acid Loaded with Chitosan: Evaluation of Physical–Chemical Properties. *Journal of Polymers and the Environment*, 31(6), 2566–2575. <https://doi.org/10.1007/s10924-022-02585-0>
94. NHV Corporation. (2023). *Gel Fraction: an indicator of the Degree of Crosslinking* | [https://www.nhv.jp/blog\\_en/post980/](https://www.nhv.jp/blog_en/post980/)
95. NIH. (1994). *Propylene - Some Industrial Chemicals*. <https://www.ncbi.nlm.nih.gov/books/NBK507483/>
96. PerkinElmer. (2022). *Thermogravimetric Analysis (TGA) TGA 8000 TGA 4000 STA 6000 / STA 8000 The Thermogravimetric Instrument Family*.
97. Qi, Y., Weng, Z., Kou, Y., Song, L., Li, J., Wang, J., Zhang, S., Liu, C., & Jian, X. (2021). Synthesize and introduce bio-based aromatic s-triazine in epoxy resin: Enabling extremely high thermal stability, mechanical properties, and flame retardancy to achieve high-performance sustainable polymers. *Chemical Engineering Journal*, 406. <https://doi.org/10.1016/j.cej.2020.126881>

98. Reed, R. P., Madhukar, M., Thaicharoenporn, B., & Martovetsky, N. N. (2014). Low-temperature mechanical properties of glass/epoxy laminates. *AIP Conference Proceedings*, 1574 60, 109–116. <https://doi.org/10.1063/1.4860612>
99. Reinhart, T. J. (1998a). *Handbook of composites*. Chapman & Hall.
100. Reinhart, T. J. (1998b). *Handbook of composites*. Chapman & Hall.
101. Rochester, J. R. (2013). Bisphenol A and human health: A review of the literature. *Reproductive Toxicology*, 42, 132–155. <https://doi.org/10.1016/J.REPROTOX.2013.08.008>
102. Samper, M. D., Petrucci, R., Sánchez-Nacher, L., Balart, R., & Kenny, J. M. (2015). New environmentally friendly composite laminates with epoxidized linseed oil (ELO) and slate fiber fabrics. *Composites Part B: Engineering*, 71, 203–209. <https://doi.org/10.1016/j.compositesb.2014.11.034>
103. Santiago, D., Guzmán, D., Ramis, X., Ferrando, F., & Serra, À. (2020). New epoxy thermosets derived from clove oil prepared by epoxy-amine curing. *Polymers*, 12(1). <https://doi.org/10.3390/polym12010044>
104. Sato, M., Maulik, N., & Das, D. K. (2002). Cardioprotection with alcohol: Role of both alcohol and polyphenolic antioxidants. *Annals of the New York Academy of Sciences*, 957, 122–135. <https://doi.org/10.1111/j.1749-6632.2002.tb02911.x>
105. Scheelhaase, J., Müller, L., Ennen, D., & Grimme, W. (2022). Economic and Environmental Aspects of Aircraft Recycling. *Transportation Research Procedia*, 65(C), 3–12. <https://doi.org/10.1016/j.trpro.2022.11.002>
106. Schutyser, W., Renders, T., Van Den Bosch, S., Koelewijn, S. F., Beckham, G. T., & Sels, B. F. (2018). Chemicals from lignin: an interplay of lignocellulose fractionation, depolymerisation, and upgrading. *Chemical Society Reviews*, 47(3), 852–908. <https://doi.org/10.1039/C7CS00566K>
107. Shang, L., Zhang, X., Zhang, M., Jin, L., Liu, L., Xiao, L., Li, M., & Ao, Y. (2018a). A highly active bio-based epoxy resin with multi-functional group: synthesis, characterization, curing and properties. *Journal of Materials Science*, 53(7), 5402–5417. <https://doi.org/10.1007/s10853-017-1797-8>
108. Shang, L., Zhang, X., Zhang, M., Jin, L., Liu, L., Xiao, L., Li, M., & Ao, Y. (2018b). A highly active bio-based epoxy resin with multi-functional group: synthesis, characterization, curing and properties. *Journal of Materials Science*, 53(7), 5402–5417. <https://doi.org/10.1007/s10853-017-1797-8>
109. Singh, M. K., & Singh, A. (2022). Dynamic mechanical analysis. In *Characterization of Polymers and Fibres* (pp. 241–271). Elsevier. <https://doi.org/10.1016/B978-0-12-823986-5.00005-1>
110. Soto, M., & Koschek, K. (2018). Diastereoisomeric diversity dictates reactivity of epoxy groups in limonene dioxide polymerization. *Express Polymer Letters*, 12(6), 583–589. <https://doi.org/10.3144/expresspolymlett.2018.48>
111. Statista. (2020). *Aviation industry - Aircraft Fleet Age*. <https://www.statista.com/statistics/751440/aviation-industry-aircraft-fleet-age-by-region/>
112. Sukanto, H., Raharjo, W. W., Ariawan, D., Triyono, J., & Kaavesina, M. (2021). Epoxy resins thermosetting for mechanical engineering. *Open Engineering*, 11(1), 797–814. <https://doi.org/10.1515/eng-2021-0078>

113. TA Instruments. (2012). *Gelation Kinetics from Rheological Experiments*. [www.tainstruments.com/](http://www.tainstruments.com/)
114. TA Instruments. (2015). *Measurement of Glass Transition Temperatures by Dynamic Mechanical Analysis and Rheology*.
115. TA Instruments. (2020a). *Overview of Glass Transition Analysis by Differential Scanning Calorimetry*.
116. TA Instruments. (2020b). *Thermogravimetric Analysis (TGA) - Theory and Applications*.
117. TA Instruments. (2023). *What is Differential Scanning Calorimetry?* <https://www.tainstruments.com/what-is-differential-scanning-calorimetry/>
118. Tam, D. K. Y., Ruan, S., Gao, P., & Yu, T. (2012). High-performance ballistic protection using polymer nanocomposites. *Advances in Military Textiles and Personal Equipment*, 213–237. <https://doi.org/10.1533/9780857095572.2.213>
119. Tcharkhtchi, A., Nony, F., Khelladi, S., Fitoussi, J., & Farzaneh, S. (2015). Epoxy/amine reactive systems for composites materials and their thermomechanical properties. In *Advances in Composites Manufacturing and Process Design* (pp. 269–296). Elsevier Inc. <https://doi.org/10.1016/B978-1-78242-307-2.00013-0>
120. TEIJIN. (2024). *TR001X Data Processing Guidelines*.
121. Tencom Ltd. (2024). *The History of Fiberglass*. <https://www.tencom.com/blog/the-history-of-fiberglass>
122. Thapa, S. B., Pandey, R. P., Il Park, Y., & Sohng, J. K. (2019). Biotechnological Advances in Resveratrol Production and its Chemical Diversity. *Molecules*, 24(14), 2571. <https://doi.org/10.3390/MOLECULES24142571>
123. Tian, Y., Ke, M., Wang, X., Wu, G., Zhang, J., & Cheng, J. (2021). A resveratrol-based epoxy resin with ultrahigh Tg and good processability. *European Polymer Journal*, 147. <https://doi.org/10.1016/j.eurpolymj.2021.110282>
124. Tian, Y., Wang, Q., Shen, L., Cui, Z., Kou, L., Cheng, J., & Zhang, J. (2020). A renewable resveratrol-based epoxy resin with high Tg, excellent mechanical properties and low flammability. *Chemical Engineering Journal*, 383. <https://doi.org/10.1016/j.cej.2019.123124>
125. TinyEco. (2024). *Guide To Material Sustainability*. <https://tinyeco.com/material-sustainability-guide>
126. Tziamtzi, C. K., & Chrissafis, K. (2021). Optimization of a commercial epoxy curing cycle via DSC data kinetics modelling and TTT plot construction. *Polymer*, 230. <https://doi.org/10.1016/j.polymer.2021.124091>
127. Vogel, S. A. (2009). The Politics of Plastics: The Making and Unmaking of Bisphenol A “Safety”. *American Journal of Public Health*, 99(Suppl 3), S559. <https://doi.org/10.2105/AJPH.2008.159228>
128. Wahab, A., Gao, K., Jia, C., Zhang, F., Tian, G., Murtaza, G., & Chen, J. (2017). Significance of Resveratrol in Clinical Management of Chronic Diseases. *Molecules (Basel, Switzerland)*, 22(8). <https://doi.org/10.3390/MOLECULES22081329>
129. Wellen, R. M. R., & Canedo, E. L. (2014). On the Kissinger equation and the estimate of activation energies for non-isothermal cold crystallization of PET. *Polymer Testing*, 40, 33–38. <https://doi.org/10.1016/J.POLYMERTESTING.2014.08.008>

130. Wen, H., Zhang, X., Xia, R., Yang, Z., & Wu, Y. (2018). Thermal Decomposition Properties of Epoxy Resin in SF6/N2 Mixture. *Materials*, 12(1), 75. <https://doi.org/10.3390/MA12010075>
131. Westlake. (2024a). *TDS-EN EPIKOTE (TM) System 600 Epoxy Datasheet*.
132. Westlake. (2024b). *TDS-EN EPIKOTE (TM) System 600-2K Datasheet*.
133. Wikipedia. (2024a). *4,4'-methylenedianiline*. <https://www.wikidata.org/wiki/Q229848>
134. Wikipedia. (2024b). *4,4'-Oxydianiline*. <https://en.wikipedia.org/wiki/4,4%27-Oxydianiline>
135. Wikipedia. (2024c). *Dapsone*. <https://en.wikipedia.org/wiki/Dapsone>
136. Wikipedia. (2024d). *Epoxy*. <https://en.wikipedia.org/wiki/Epoxy>
137. Wikipedia. (2024e). *Thermosetting polymer* - *Wikipedia*. [https://en.wikipedia.org/wiki/Thermosetting\\_polymer](https://en.wikipedia.org/wiki/Thermosetting_polymer)
138. *Wikipedia*. (2024f). <https://www.wikipedia.org/>
139. Withers, P. J. (2000). Elastic and Thermoelastic Properties of Brittle Matrix Composites. *Comprehensive Composite Materials*, 25–45. <https://doi.org/10.1016/B0-08-042993-9/00087-5>
140. Yan, F., Sun, X., & Xu, C. (2018). Protective effects of resveratrol improve cardiovascular function in rats with diabetes. *Experimental and Therapeutic Medicine*, 15(2), 1728–1734. <https://doi.org/10.3892/ETM.2017.5537>
141. Yu, Q., Peng, X., Wang, Y., Geng, H., Xu, A., Zhang, X., Xu, W., & Ye, D. (2019). Vanillin-based degradable epoxy vitrimers: Reprocessability and mechanical properties study. *European Polymer Journal*, 117, 55–63. <https://doi.org/10.1016/j.eurpolymj.2019.04.053>
142. Zhang, J., Lin, G., Vaidya, U., & Wang, H. (2023). Past, present and future prospective of global carbon fibre composite developments and applications. *Composites Part B: Engineering*, 250. <https://doi.org/10.1016/j.compositesb.2022.110463>
143. Zwingelstein, M., Draye, M., Besombes, J. L., Piot, C., & Chatel, G. (2019). Trans-Resveratrol and trans- $\epsilon$ -Viniferin in Grape Canes and Stocks Originating from Savoie Mont Blanc Vineyard Region: Pre-extraction Parameters for Improved Recovery. *ACS Sustainable Chemistry and Engineering*, 7(9), 8310–8316. [https://doi.org/10.1021/ACSSUSCHEMENG.8B06723/SUPPL\\_FILE/SC8B06723\\_SI\\_001.PDF](https://doi.org/10.1021/ACSSUSCHEMENG.8B06723/SUPPL_FILE/SC8B06723_SI_001.PDF)

## Appendix A

### A.1. Stoichiometry Ratio Determination

#### Theory and Practice

In order to generate an epoxy network with a high degree of crosslinking, it is necessary to create an optimally proportioned mixture of monomer and hardener materials. This ensures that all of the epoxy monomer molecules react with all of the curing agent molecules. As per Section 3.5.3, RTE is a tri-functional epoxy monomer due to the 3 epoxy groups present in its molecule. According to Section 3.2.2, the functionality of an amine is defined by the number of hydrogen atoms connected to nitrogen. DDS is a di-amine and each amine contains 2 active hydrogens. Therefore, the functionality of DDS is 4.

$$\text{Stoichiometric Ratio} = \frac{EEW}{AHEW} = \frac{M_{epoxy} * N_{hardener}}{N_{epoxy} * M_{hardener}}$$

Where EEW – epoxy equivalent weight ( $\frac{g}{eq}$ ); AHEW – amine hydrogen equivalent weight ( $\frac{g}{eq}$ );  $M_{epoxy}$  – molecular weight of epoxy resin monomer ( $\frac{g}{mol}$ );  $M_{hardener}$  – molecular weight of amine hardener ( $\frac{g}{mol}$ );  $N_{epoxy}$  – number of epoxy groups per molecule ( $\frac{eq}{mol}$ );  $N_{hardener}$  – number of active hydrogens in amine hardener ( $\frac{eq}{mol}$ ).

Thus, the theoretical stoichiometric molar ratio of both RTE:DDS and T742:DDS is calculated to be 1.33:1.

However, the theoretically calculated stoichiometric ratio of the epoxy resin formulation does not always represent the actual optimal proportion of the reactants. This is attributed to the fact that the synthesis of the epoxy monomers results in oligomeric products. This implies that some of the monomers form into oligomers containing only a few repeating units. Oligomerisation reduces the overall functionality of the monomer, which needs to be accounted for during resin preparation. This ensures proper cross-linking and, subsequently, good properties of the resin.

#### Ratio Estimation Procedure

It was decided to select the stoichiometric ratio of the RTE-DDS blend according to the results of the Dynamical Mechanical Analysis (DMA) analysis which are presented below. DMA enables tracking the change of storage modulus with respect to temperature. The significance of this characterisation method is described in more detail in Section 5.1.3.

As can be seen from the graphs, the mechanical behaviour is similar for various stoichiometries across a large temperature range. However, around 350°C the storage modulus starts to drop as the resin enters the glass transition temperature region. It can be observed that the molar ratio of 1.5:1 leads to a delayed drop in modulus when compared to other stoichiometries, corresponding to a higher  $T_g$ . As a result, it was decided to use this value as the molar ratio for resin preparation.

Furthermore, when converted to mass ratio, it became 2.39:1. This mass ratio was used for sample preparation in all of the following sections.

Similar process was used for other resin formulations, including T742-DDS (molar ratio: 1.45:1, weight ratio: 2.69:1) and BADGE-DDS (molar ratio: 2.06, weight ratio: 2.82:1).

